TESIS PUCP

# Structural, luminescence and Judd-Ofelt analysis to study the influence of post-annealing treatment on the AlN:Tb thin films prepared by radio frequency magnetron sputtering

Thesis submitted for the degree of

Master of Materials Science and Engineering

AUTOR

**Karem Tucto Salinas**

THESIS SUPERVISOR

**Dr. Roland Weingärtner**

JURY MEMBERS

**Dr. Thomas Kups**

**Dr. Rolf Grieseler**

**Ilmenau-Germany / Lima-Perú**

**February 2016**

Tesis publicada con autorización del autor
No olvide citar esta tesis

TESIS PUCP

PONTIFICIA UNIVERSIDAD CATÓLICA DEL PERÚ

# Preface

This thesis was performed in the framework of a double degree program with the Technische Universität Ilmenau (TUIlm) and the Pontificia Universidad Católica del Perú (PUCP). The research for this thesis has been carried out in the Laboratory at ZMN TUIlm, in cooperation with the Laboratory of Material Science at the Department of Physics, PUCP.

I would like to take this opportunity to express my sincere gratitude and recognition towards all the people who supported me during this Master Thesis year. First of all, my recognition goes out to my supervisors: Dr. Thomas Kups, for his suggestions, encouragements and guidance in approaching the different challenges during the thesis, and Dr. Roland Weingärtner, who gave me the opportunity to conduct my study in his research group. My deepest gratitude also goes to Dr. Rolf Grieseler, from whom I received a lot of help and encouragement. Thank you, Rolf, for the support and patient guidance from the start until the end of this year. And I would like to thank MSc. Andrés Guerra, your availability and your quick and productive responses to my questions were profoundly appreciated.

I am also thankful to all the people who assisted me in the lab and helped creating a pleasant work environment Dr. rer. nat. Jörg Pezoldt, Dr.-Ing. Thomas Stauden, Elvira Remdt and Diana Roβberg. Special thanks to the FONDECYT studentship for financing according to the contract between PUCP-FONDECYT, without it, this thesis would have not been possible

Finally I would like to thank my family, all this work was made for you and me.



Tesis publicada con autorización del autor
No olvide citar esta tesis

TESIS PUCP

PONTIFICIA UNIVERSIDAD CATÓLICA DEL PERÚ

# Contents

**Preface** ........ i

**Contents** ........ ii

**Abstract** ........ iv

**Resumen** ........ v

**1 Introduction** ........ 1

**2 Theoretical background** ........ 3

2.1 Crystal field splitting of the energy levels ........ 5

2.2 The Judd-Ofelt theory of 4f-4f transitions ........ 7

2.2.1 Judd-Ofelt parameters calculation from absorption spectrum ........ 10

2.2.2 Judd-Ofelt parameters calculation from emission spectrum ........ 13

2.3 Cathodoluminescence activation ........ 18

2.3.1 Electron beam interactions ........ 18

2.3.2 Direct and indirect excitation of RE ions by incident electrons ........ 19

2.4 Properties of the investigated material systems from the perspective of the application in luminescent devices ........ 21

2.4.1 Aluminum nitride ........ 22

2.4.2 Terbium doped aluminum nitride ........ 23

2.5 Concentration quenching and thermal activation of RE ions doped materials ........ 25

**3 Experimental details** ........ 27

3.1 Film deposition and annealing ........ 27

3.2 Film structure, composition and light emission characterization ........ 28

**4 Results and Discussion** ........ 32

4.1 Judd-Ofelt parameters calculation from emission spectrum ........ 32

4.2 Luminescence analysis ........ 36

4.2.1 Emission spectra of AlN:Tb thin films ........ 36

4.2.2 Radiative lifetime of AlN:Tb thin films ........ 39



Tesis publicada con autorización del autor
No olvide citar esta tesis

TESIS PUCP

4.3 Structural analysis ... 48

4.3.1 X-ray diffraction ... 49

4.3.2 RHEED surface analysis ... 53

4.3.3 EDX composition ratio ... 55

4.3.4 SEM micrographs ... 57

**5 Conclusion ... 60**

**References ... 64**

Tesis publicada con autorización del autor
No olvide citar esta tesis

TESIS PUCP

PONTIFICIA UNIVERSIDAD CATÓLICA DEL PERÚ

# Abstract

This thesis investigates the effects of the annealing treatments on the spontaneous emission, radiative lifetime, composition and structure of terbium doped aluminum nitride films deposited on silicon substrates by radio frequency magnetron sputtering. The purpose of this thesis is to determine the Judd-Ofelt intensity parameters from the emission spectrum, in order to calculate the radiative lifetime, branching ratios and spontaneous emission probability. The optimal annealing temperature for the emission of terbium doped aluminum nitride is investigated. The annealing treatment was performed in the temperature range starting from 500 up to 1000°C. Two annealing techniques were investigated: rapid thermal processing and a rather slower quartz tube furnace. Furthermore, two heating approaches were applied: direct heating at 500, 750, 900 and 1000 °C, and multistep heating of 500-750°C, 750-900°C and 900-1000°C. The film was then characterized to determine which conditions resulted in the highest emission of Tb. The film characterization includes the use of X-ray diffraction to study the film's crystal orientation, Energy dispersive X-ray spectroscopy to determine the film composition, Scanning electron microscopy and Reflection high-energy electron diffraction to resolve the surface morphology and structure of the film respectively. The luminescent intensity and the radiative lifetime were analyzed using cathodoluminescence measurement and Judd-Ofelt analysis. This work shows that the activation of the Tb ions to enhance the emitted cathodoluminescence intensity depends on the structure of the film and the oxygen concentration. The best annealing temperature to produce the highest emitted light intensity in this set of experiments were the single-step heating at 750°C using rapid thermal processing.

**Key words**: luminescence, radiative lifetime, Judd-Ofelt analysis, Aluminum nitride, X-ray diffraction, scanning electron microscopy, energy dispersive X-ray spectroscopy.



Tesis publicada con autorización del autor
No olvide citar esta tesis

TESIS PUCP
PONTIFICIA UNIVERSIDAD CATÓLICA DEL PERÚ

# Resumen

En la presente tesis se investiga la influencia del tratamiento térmico en la probabilidad de emisión espontánea, el tiempo de vida radiativa, la composición y la estructura de películas delgadas de nitruro de aluminio dopadas con terbio depositadas sobre substratos de silicio por la técnica de pulverización catódica de radiofrecuencia.

La tesis tiene por objetivo aplicar el análisis de Judd-Ofelt usando el espectro de emisión. Se propone un método que utiliza la intensidad de las bandas de transición del espectro de emisión y las ecuaciones de Judd-Ofelt para calcular las propiedades espectrales: tiempo de vida radiativa, tasa de los canales de transición y probabilidad de emisión espontánea. Usando el software Wolfram Mathematica 9.0 se implementa un programa con el método propuesto.

Las películas se trataron térmicamente a 500, 750, 900 y 1000 °C. Se investigaron dos técnicas del tratamiento térmico: Tratamiento térmico rápido y Horno tubular de vidrio de cuarzo. Con el tratamiento térmico rápido se usaron dos tipos de calentamiento: calentamiento directo a la temperatura de tratamiento térmico, y calentamiento sucesivo de la película desde la menor hasta la mayor temperatura.

El análisis estructural de las películas fue realizada con difracción de rayos X. A nivel de superficie se caracterizó la estructura y la morfología con las técnicas de difracción de electrones reflejados de alta energía y microscopía electrónica de barrido. La luminiscencia fue medida con la técnica de catodoluminiscencia. Las propiedades espectrales fueron calculadas usando el método propuesto.

La intensidad de luz emitida se incrementó y luego decayó con la temperatura de tratamiento. La relación entre la intensidad de emisión, la estructura, composición y los parámetros de Judd-Ofelt son mostrados mediante gráficas y tablas. Los resultados obtenidos muestran una mayor activación de los iones de terbio en las películas calentadas directamente a 750°C usando el tratamiento térmico rápido.

**Palabras Clave:** Luminiscencia, tiempo de vida radiativa, análisis de Judd-Ofelt, nitruro de aluminio, difracción de rayos X, microscopía electrónica de barrido, espectrometría por dispersión de energía de rayos X.



Tesis publicada con autorización del autor
No olvide citar esta tesis

TESIS PUCP

ET LUX IN TENEBRIS LUCET MCMXVII PONTIFICIA UNIVERSIDAD CATÓLICA DEL PERÚ

# 1 Introduction

Rare earth (RE) doped wide band gap semiconductors are of great importance for optoelectronics and photonics applications. The RE elements exhibit a unique electronic structure which differs from other transition metal elements by an unfilled $4f^n$ electron shell. Embedded in a matrix, RE's are usually found in the trivalent state with the $4f^n$ electrons shielded from the chemical influence of the host material by the filled $5s^2$ and $5p^6$ shells [1]. When these materials are excited by various means (e.g. light, electrical field, etc.), well-defined emission peaks of fixed wavelengths are observed due to the $4f^n$ intra-shell transitions in the RE ion core [2]. The emission color of RE ions are host independent. This special feature of the RE ions found potential applications in several electroluminescent devices: flat panel displays, light emission diodes (LEDs) and laser diodes are some examples [3], [4]. Since the RE emission is host independent, they are an alternative to the common band-to-band transition emission; where the gap of the host determine the color of the device. The use of group III-nitrides semiconductors such as AlN, GaN and InN as a host, are attributed to their energy band gap range of 1.9 to 6.2 eV. Which make them suitable transparent materials for light generation with colors ranging from red to ultraviolet wavelengths [5]–[7].

Among other techniques to produce semiconductor thin films doped with RE ions (e.g. chemical vapor deposition, molecular beam epitaxy), an advantageous way is by magnetron sputtering deposition, due to its high-throughput production and high quality films [8]–[10]. The radiofrequency (RF) magnetron sputtering is a method most often used for thin film deposition in industry and research [11]. Crystalline and amorphous materials can be obtained by this method depending on the sputtering conditions. Post-deposition annealing treatments can be applied to the produced films to subsequently improve the structures causing crystallization and grain coarsening [12], [13]. The annealing treatment introduces modifications in the matrix structure which affects the mechanism of activation of the RE ion [14]. Such influence can be conveniently controlled for the achievement of more optically efficient materials.

The fabrication of luminescent based devices requires the knowledge of the spectral properties of the material for an accurate control of the performance characteristics. Important radiative parameters are the emission transition rates, the branching ratios and the radiative lifetime [15]–[18]. They are useful parameters to estimate the quantum yield and



Tesis publicada con autorización del autor
No olvide citar esta tesis

TESIS PUCP

PONTIFICIA UNIVERSIDAD CATÓLICA DEL PERÚ

emission cross section of a doped material to evaluate its suitability for solid-state lighting [19]. The Judd-Ofelt (JO) theory [20]–[22] provides the mathematical formalism and the physical picture behind the 4f transitions of rare earths for the determination of the radiative parameters.

In this thesis a systematical study of the luminescence and structural properties of terbium doped aluminum nitride (AlN:Tb) thin films grown by RF magnetron sputtering and submitted to annealing treatments will be presented. AlN thin films semiconductors are materials used in microelectronic processing due to its excellent combination of electrical, thermal and optical properties [23], [24]. Its large optical band gap ($E_g$ = 6.2 eV) allows transparency to emission in the ultraviolet (UV) and visible (VIS) range of light, making this material a viable host for luminescent rare earth ions. When doped with terbium, the semiconductor exhibits a characteristic trivalent Tb emission spectra with a dominating green emission at 542nm [25].

Recent efforts have been focused on studying the mechanism affecting the luminescence intensity of crystalline and amorphous Tb doped AlN thin films [26]–[29]. All these works investigate the effect of annealing treatments to improve the emission intensity of the films. However, no attention has been paid to the application of the JO theory for determining the radiative transition rates, radiative lifetime and branching ratio parameters. The JO analysis affronts limitations here. First, there is the absence of adequate absorption spectra of thin films to observe the specific absorption bands of the transition manifolds; and second, the calculation of the Judd–Ofelt intensity parameters becomes much harder using only the emission spectrum.

The development of a method to determine the JO intensity parameters using the emission spectra is one important goal of this thesis. The second aim is to investigate the effect of annealing temperature on the cathodoluminescence spectra of AlN:Tb thin films by using the developed method to calculate the radiative parameters such as the spontaneous emission probabilities, branching ratios and radiative lifetime. Furthermore, structural and compositional characterization will be carried out to see the influence of annealing temperature on phase formation, composition and surface morphology of the AlN:Tb samples. The evolution of the calculated radiative parameters along with the changes on microstructure and composition at increasing annealing temperature will be discussed in this work.



Tesis publicada con autorización del autor
No olvide citar esta tesis

TESIS PUCP
PONTIFICIA UNIVERSIDAD CATÓLICA DEL PERÚ

# 2 Theoretical background

The luminescence spectra of rare earth ions has attracted interest in science and technology for its special characteristics such as sharp spectral lines, wavelength independent peaks and high color purity (see Figure 2.1). This luminescence is generated by the intra f-shell transition of electrons from an excited energy level to a lower energy level. It can occur in two ways: the excess of energy is radiated away in the form of a luminescence photon (radiative transition) with a radiative decay rate $k$ or it is transmitted in the form of vibrations to the crystal lattice (non-radiative transition) with a non-radiative decay rate $\Gamma$ [30]. The quantum yield for light emission is given by:

$$\eta = \frac{k}{\Gamma + k} = \frac{\tau_{exp}}{\tau_r} \tag{2.1}$$

Here $\tau_r = 1/k$ is the radiative lifetime and $\tau_{exp} = 1/(\Gamma + k)$ is the experimental lifetime. The quantum yield is an important parameter related to the power efficiency of a solid state luminescent device. It measures the fraction of input excitation energy that can be converted into light emission [31]. The calculation of the quantum yield requires the knowledge of the experimental luminescence lifetime $\tau_{exp}$ and the radiative lifetime $\tau_r$.

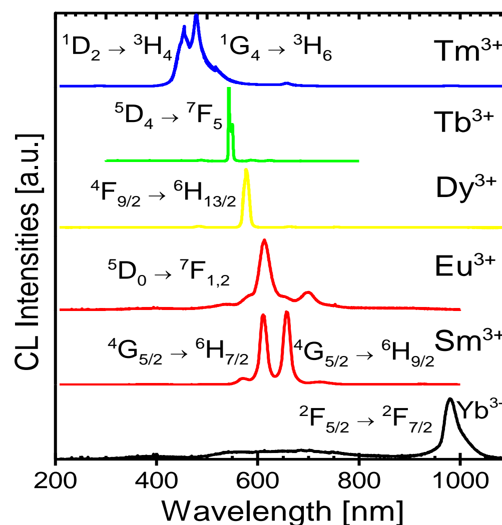


***Figure 2.1*** *Cathodoluminescence spectra of different RE$^{3+}$ ions. Image from* [32].



Tesis publicada con autorización del autor
No olvide citar esta tesis

Thus, for designing efficient luminescent devices the radiative lifetime is an important parameter as it influences the quantum efficiency. By definition, the radiative lifetime is the time it takes to the electrons in an excited state to decay by emitting a photon. The experimental measure of the radiative lifetime is possible for low RE ion dopant concentration and large energy gaps between the excited energy level and the next lowest lying level [33]. With these conditions the non-radiative transition rate is negligible and the experimental lifetime coincide with the radiative lifetime [34]. However, the latter is very often difficult to measure because it is necessary to populate the excited state just enough for detection, with a pulse width much smaller than any relaxation time constant [35]. Another possible approach to determine the radiative lifetime consists of applying the Judd-Ofelt theory [36] on luminescence spectra.

There are three main emission mechanisms: the intraconfigurational $4f \rightarrow 4f$ transitions, the broader $4f \rightarrow 5d$ transitions and charge transfer transitions (metal-to-ligand, MLCT or ligand-to-metal, LMCT). Among them, the intraconfigurational $4f \rightarrow 4f$ transition is responsible for the attractive line-like emission and wavelength independent peaks characteristics. Although the $4f \rightarrow 4f$ transitions are known to be strictly forbidden by the Laporte selection rule, this no longer applies when the RE ion interacts with a noncentrosymmetric field (see section 2.1). The $4f \rightarrow 4f$ radiative transition consists mainly of a magnetic dipole (MD) and induced electric dipole (ED) transitions. The JO theory describes $4f \rightarrow 4f$ transitions and has been very successful in reproducing the spectral intensities of these transitions for RE ions in solids [37].

This chapter outlines the energy levels responsible for the 4f – 4f transitions of rare earth ions in solids. The equations derived by the JO theory are presented with a description of the method applied to obtain the JO parameters from the absorption spectra. A detailed explanation of the proposed method is here introduced for the calculation of the JO parameters using only the emission spectra. The expansion of the JO theory using the emission spectra is necessary here since the absorption band transitions are not seen due to the highly sub-bandgap absorption in the amorphous AlN, $Si_3N_4$, SiC:H thin film host materials. The radiative transition rates, branching ratios and radiative lifetime quantities are then calculated. Furthermore, emission properties of aluminum nitride and terbium are also presented in this chapter.



Tesis publicada con autorización del autor
No olvide citar esta tesis

TESIS PUCP

PONTIFICIA UNIVERSIDAD CATÓLICA DEL PERÚ

## 2.1 Crystal field splitting of the energy levels

As defined by IUPAC, rare earth metals are the set of seventeen chemical elements in the periodic table: scandium, yttrium, and the 15 lanthanides from lanthanum through lutetium. The electronic configuration of the RE ions are characterized by a xenon core, an unfilled 4f shell, and the larger radial expansion of the $5s^2 5p^6$ shells from the Xe core. This makes the 4f orbitals "inner orbitals" shielded from outside perturbing influences.

In order to depict the energy levels seen in the spectral transitions of a RE ion, the quantum mechanical description of the electronic states in an atom is applied to the case of an ion embedded in a chemical environment and submitted to the effect of the crystal field. The Hamiltonian operator used in the quantum mechanical calculations of the energy levels diagram of a RE ion (see Figure 2.2) is given by:

$$\mathcal{H} = \sum_{i=1}^{n}\left(-\frac{Ze^2}{4\pi\varepsilon_0 r_i} - \frac{\hbar^2}{2m_e}\nabla_i^2\right) + \sum_{i\neq j}^{n}\frac{Ze^2}{4\pi\varepsilon_0 r_{ij}} + \lambda\cdot\vec{L}\cdot\vec{S} + V_{CF} \tag{2.2}$$

The first terms in the Hamiltonian operator $\mathcal{H}$ are the kinetic and potential energies in the system. The sum of $Ze^2/r_{ij}$ counts for the Coulombic interactions (where $r_{ij}$ is the distances between the electrons) responsible for the division of the electronic configuration into spectroscopic terms written as $^{2S+1}L$ . The spin – orbit coupling $\left(\lambda\cdot\vec{L}\cdot\vec{S}\right)$, with $\lambda$ a positive spin orbit coupling constant, splits the spectroscopic terms into a number of states represented by the full term symbol $^{2S+1}L_J$. Finally the crystal field represented by the potential $V_{CF}$ describes the electrostatic environment felt by the $i^{th}$ electron at $\vec{r_i}$ position generated by a point charge $Z$ at $\overrightarrow{R_L}$.

$$V_{CF} = \sum_{L}\frac{(Ze^2)_L}{4\pi\varepsilon_0\left|\overrightarrow{R_L} - \vec{r_i}\right|} \tag{2.3}$$

The crystal field is responsible for the splitting of the $^{2S+1}L_J$ spectroscopic levels into several other levels of only few hundreds of $cm^{-1}$ called Stark levels [37]. When embedded into a solid, the spherical symmetry of the electronic structure in the free ion is lost, and the remaining $(2J + 1)$ degeneracy of the spectroscopic levels is removed [37] .



Tesis publicada con autorización del autor
No olvide citar esta tesis

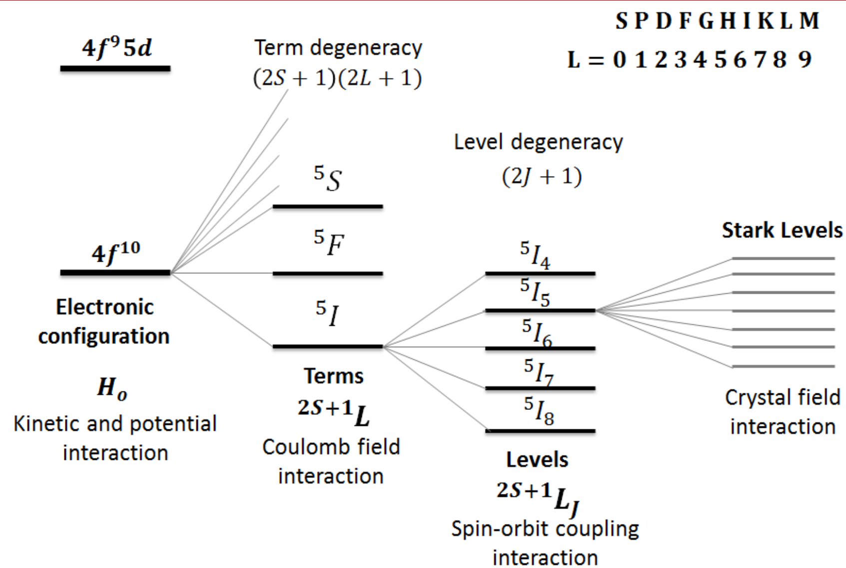


***Figure 2.2*** *Diagram representing the interactions that leads to the splitting of the electronic energy levels for a lanthanide ion in a crystal field. Image modified from* [1].

Due to the screening effect on the 4f electrons, the influence of the crystal field over the 4f RE electrons is small in comparison to spin-orbit coupling, whereas in transition metals occurs the inverse situation [38]. However, this little influence of the host material plays an important role in determining the intensity pattern spectra of the optically active lanthanide ion: the $4f \rightarrow 4f$ transitions forbidden by Laporte selection rule no longer applies when the RE ion interacts with a noncentrosymmetric field that splits the orbitals into hyperfine structures.

The theory dealing with the split of the energy levels is known as ligand field theory in general and crystal field theory (CF) in the case of a periodic lattice [1]. In the CF point of view the ligands are treated as negative point charges surrounding the metal ion which feels a repulsive effect. The bonds character is thought to be purely ionic. However, a covalent character was found to dominate the observed lanthanide crystal field parameters [39]. Though the CF model fails to give a correct description of the problem, its simple electrostatic model has been retained as a framework to deal with complex calculations [40]. The ligand field theory is a modified form of the CF theory that takes into account the covalent nature and overlap of the metal-atom orbitals.



Tesis publicada con autorización del autor
No olvide citar esta tesis

## 2.2 The Judd-Ofelt theory of 4f-4f transitions

In this section the calculation of the spontaneous emission probability, branching ratio and radiative lifetime in RE ions using the JO theory will be outlined. For a detailed explanation of the spectral intensities of $4f \rightarrow 4f$ the reader is referred to the review by M.P. Helen *et al.* [41] as well as Görrler-Walrand and Binnemans [42].

In emission spectra, the electrons from an excited state $|4f^n SLJ\rangle$ can decay to various lower-energy final states $|4f^n S'L'J'\rangle$. The radiative lifetime is defined as the reciprocal of the sum of the total spontaneous radiative decay rate for a transition, and is given by:

$$\tau_r = \frac{1}{\sum_{S'L'J'}(A_{SLJ \rightarrow S'L'J'})} \quad (2.4)$$

Here $A_{SLJ \rightarrow S'L'J'}$ is the total spontaneous emission probability. The spontaneous emission is the process involving the electron transition from a higher to a lower energy state emitting a photon. It takes into account the induced ED transition and the MD transition which are generated by the interaction of the RE ion with the electric and magnetic field component of light, through an electric dipole and a magnetic dipole respectively. The total spontaneous emission probability for a transition is given by:

$$A_{SLJ \rightarrow S'L'J'} = A^{ED}_{SLJ \rightarrow S'L'J'} + A^{MD}_{SLJ \rightarrow S'L'J'} \quad (2.5)$$

***Electric dipole contribution***

The spontaneous emission probability $A^{ED}_{SLJ \rightarrow S'L'J'}$ for an ED transition $|4f^n SLJ\rangle \rightarrow |4f^n S'L'J'\rangle$ is related to the oscillator strength $f^{ED}$ of the ED induced emission intensity.

$$A^{ED}_{SLJ \rightarrow S'L'J'} = \frac{2\pi e^2}{m_e \varepsilon_0 \bar{\lambda}^2 c} f^{emi}_{ED} \quad (2.6)$$

The physical constants are the speed of light ($c$), the electron charge ($e$), the electron mass ($m_e$), the mean transition wavelength ($\bar{\lambda}$). The mean wavelength is defined by the integral of



Tesis publicada con autorización del autor
No olvide citar esta tesis

the wavelenght multiplied by the intensity for a transition $J \rightarrow J'$ divided by the area below the intensity of the same transition.

$$\bar{\lambda}_{J\rightarrow J'} = \int_{J\rightarrow J'} \lambda I(\lambda)d\lambda \Big/ \int_{J\rightarrow J'} I(\lambda)d\lambda \tag{2.7}$$

The induced ED oscillator strength given by Eq.(2.8) is obtained by the JO theory. It is obtained solving the electric dipole matrix elements $\langle\psi|\,\vec{P}\,|\psi'\rangle$. Where $\vec{P}$ is the ED operator linked to the electric field component of light promoting a transition between the $4f$ initial $\langle\psi|$ and final $|\psi'\rangle$ states. The JO theory succeed in finding an easy to handle expression for the induced ED absorption intensity, by proposing four assumptions [1]:

i. All the sublevels of a $4f^{n-1}5d$ state are degenerate in $J$.
ii. The $4f \rightarrow 4f$ energy separation and the $4f \rightarrow 4f^{n-1}5d$ energy separation are the same.
iii. All Stark sublevels within the ground state are equally populated.
iv. The host material is optically isotropic.

Although these assumptions are seem to be quite drastic and modetately fullfilled for most of the RE ions [41], they are helpful in order to simplify the calculations. The mathematical steps to obtain the oscillator strength equation is beyond the scope of this section, for further details see Walsh [1], Judd [20] and Ofelt [22].

$$f_{ED}^{abs} = \frac{8\pi^2 m_e c}{3h\bar{\lambda}} \frac{1}{(2J+1)} \frac{\chi_{ED}^{abs}}{n} \sum_{j=2,4,6} \Omega_{(j)} \left|\langle 4f^n SLJ || U^{(j)} || 4f^n S'L'J' \rangle\right|^2 \tag{2.8}$$

Where, $h$ is the Planck constant. The oscillator strength expression for absorption is typically used in the determination of the JO parameters $\Omega_{(j)}$ where $j = 2,4,6$ arise from the parametrization of the crystal field to consider the induced ED transitions [42]. Several authors consider the JO parameter $\Omega_2$ is related to the covalency of the chemical bond between the RE ions and the ligand ions. It is said $\Omega_2$ is more sensitive to the local symmetry of the environment, while the structural information carried by $\Omega_4$ and $\Omega_6$ is considered less accurate and insensitive to the local environment [15], [43], [44]. Sometimes $\Omega_4$ and $\Omega_6$ are related to the viscosity and the rigidity of the medium [15].



Tesis publicada con autorización del autor
No olvide citar esta tesis

The tensorial form $U^{(j)}$ arises in the calculation of ED transition intensities. The dimensionless doubly-reduced matrix elements $\langle\,||U^{(j)}||\,\rangle$ of the tensor operator $U^{(j)}$ are values already tabulated in Kaminskii [45] for a given $RE^{3+}$ ion. The literature review considers these values fixed and usable for an analysis of any insulating crystal, since they are insensitive to the surroundings and vary only slightly from host to host [37], [45].

The factor $\chi_{ED}^{abs} = [(n^2+2)/3]^2$ in equation (2.8) is the local-field correction for the induced ED absorption in the virtual cavity model. This local-field correction takes into account that the local electric field at the site of the ion undergoing an optical transition is quite different from the macroscopic field in the medium [41]. The dimensionless refractive index $(n)$ can be modelled using a dispersion equation (e.g. Sellmeier or Cauchy's equation).

Finally, for the $f_{ED}^{emi}$electric dipole induced emission oscillator strength the local-field correction has to be multiplied by $n^2$ [41], thus $\chi_{ED}^{emi} = n^2\chi_{ED}^{abs}$.

$$f_{ED}^{emi} = \frac{8\pi^2 m_e c}{3h\bar{\lambda}} \frac{1}{(2J+1)} \frac{\chi_{ED}^{emi}}{n} \sum_{j=2,4,6} \Omega_{(j)} \left|\langle 4f^n SLJ \middle|\middle| U^{(j)} \middle|\middle| 4f^n S'L'J' \rangle\right|^2 \tag{2.9}$$

The spontaneous emission probability for an ED transition $|4f^n SLJ\rangle \rightarrow |4f^n S'L'J'\rangle$ is given by:

$$A_{SLJ\rightarrow S'L'J'}^{ED} = \frac{16\pi^3 e^2}{3\varepsilon_0 h\bar{\lambda}^3} \frac{1}{(2J+1)} \chi_{ED}^{emi} \sum_{j=2,4,6} \Omega_{(j)} \left|\langle 4f^n SLJ \middle|\middle| U^{(j)} \middle|\middle| 4f^n S'L'J' \rangle\right|^2 \tag{2.10}$$

***Magnetic dipole contribution***

For the magnetic dipole transition in absorption (or emission), the oscillator strength only depends on one reduced matrix element $\langle 4f^n SLJ||L+gS||4f^n S'L'J'\rangle$:

$$f_{MD}^{abs} = \frac{h}{6m_e c\bar{\lambda}} \frac{n}{(2J+1)} |\langle 4f^n SLJ||L+gS||4f^n S'L'J'\rangle|^2 \tag{2.11}$$



Tesis publicada con autorización del autor
No olvide citar esta tesis

TESIS PUCP

PONTIFICIA UNIVERSIDAD CATÓLICA DEL PERÚ

Where the tensor $L + gS$ is the magnetic dipole operator and $g = 2.002319304362$ is the electron factor [41].

The spontaneous emission probability for an MD transition $|4f^nSLJ\rangle \rightarrow |4f^nS'L'J'\rangle$ is given by:

$$A^{MD}_{SLJ\rightarrow S'L'J'} = \frac{\pi he^2}{3\varepsilon_0 m_e c^2 \bar{\lambda}^3}\frac{1}{(2J+1)}n^3|\langle 4f^nSLJ||L + gS||4f^nS'L'J'\rangle|^2 \quad (2.12)$$

***Branching ratio***

Another important parameter characterizing the luminiscence properties of a material is the branching ratio of a transition $\beta_{SLJ\rightarrow S'L'J'}$. The branching ratio shows the relative contribution of a transition $|4f^nSLJ\rangle \rightarrow |4f^nS'L'J'\rangle$ to the total spontaneous emission probability:

$$\beta_{SLJ\rightarrow S'L'J'} = \frac{A^{ED}_{SLJ\rightarrow S'L'J'} + A^{MD}_{SLJ\rightarrow S'L'J'}}{\sum_{S'L'J'}\left(A_{SLJ\rightarrow S'L'J'}\right)} \quad (2.13)$$

This means the branching ratio gives the amount of spontaneous radiation for a given channel of transition among the other transition channels (or branches). The branching ratio becomes a significant parameter for a luminescent device designer [46]. Thus, the branching ratio value of a transition can indicate if the material is adequate to obtain good luminiscence characteristics or not for laser applications, depending on how high is the value obtained. Usually it must show the highest values for a good laser transition [47]. For example, a transition with $\beta > 0.5$ is a potential candidate for laser action [41].

### 2.2.1 Judd-Ofelt parameters calculation from absorption spectrum

The calculation of the radiative lifetime, the manifold to manifold spontaneous emission probability and branching ratio depends on Eq. (2.4), Eq. (2.10) and Eq. (2.13) and they are



Tesis publicada con autorización del autor
No olvide citar esta tesis

functions of the three JO parameters $\Omega_2, \Omega_4, \Omega_6$. In order to determine the JO parameters the traditional JO analysis relies on absorption measurements, specifically the integrated absorption coefficient $\alpha(\lambda)$ over the wavelength range for a transition band. It forms part of the expresion for the experimental line strength of a transition given by [48]:

$$S_{SLJ \to S'L'J'}^{exp} = \frac{3ch(2J+1)n}{8\pi^3 \bar{\lambda} e^2 N_A \, \chi_{ED}^{abs}} \int \alpha(\lambda) d\,\lambda \tag{2.14}$$

With $N_A$ the Avocadro's number and $\bar{\lambda}$ the mean wavelength of the specific absorption band. The JO expression of the line strenght in Eq. (2.15) can then be compared to the experimental line strength as part of a procedure for fitting the $\Omega_2, \Omega_4, \Omega_6$ parameters.

$$S_{SLJ \to S'L'J'}^{ED} = e^2 \sum_{j=2,4,6} \Omega_{(j)} \left| \langle 4f^n SLJ \| U^{(j)} \| 4f^n S'L'J' \rangle \right|^2 \tag{2.15}$$

The standard least-squares method minimize the absolute differences between the experimental and the calculated values for the line strength. By using the absolute differences as system of $N$ equations for the $N$ transitions $J \to J'$ (abreviation of $SLJ \to S'L'J'$) the matrix representation given by Eq. (2.17) can be obtained to:

$$\begin{aligned} S_1^{exp} &= \Omega_2 \left| \langle U_1^{(2)} \rangle \right|^2 + \Omega_4 \left| \langle U_1^{(4)} \rangle \right|^2 + \Omega_6 \left| \langle U_1^{(6)} \rangle \right|^2 \\ S_2^{exp} &= \Omega_2 \left| \langle U_2^{(2)} \rangle \right|^2 + \Omega_4 \left| \langle U_2^{(2)} \rangle \right|^2 + \Omega_6 \left| \langle U_2^{(2)} \rangle \right|^2 \\ &\vdots \\ S_N^{exp} &= \Omega_2 \left| \langle U_N^{(2)} \rangle \right|^2 + \Omega_4 \left| \langle U_N^{(2)} \rangle \right|^2 + \Omega_6 \left| \langle U_N^{(2)} \rangle \right|^2 \end{aligned} \tag{2.16}$$

$$\begin{pmatrix} S_1^{exp} \\ \vdots \\ S_N^{exp} \end{pmatrix} = \begin{pmatrix} \left| \langle U_1^{(2)} \rangle \right|^2 & \left| \langle U_1^{(4)} \rangle \right|^2 & \left| \langle U_1^{(6)} \rangle \right|^2 \\ \vdots & \vdots & \vdots \\ \left| \langle U_N^{(2)} \rangle \right|^2 & \left| \langle U_N^{(4)} \rangle \right|^2 & \left| \langle U_N^{(6)} \rangle \right|^2 \end{pmatrix} \begin{pmatrix} \Omega_2 \\ \Omega_4 \\ \Omega_6 \end{pmatrix} \to \boldsymbol{Y} = \boldsymbol{X\Omega} \tag{2.17}$$

Due to the large number of calculations to be made, matrices are suitable for computer based calculations [1].The matrix least square estimation for the JO parameters is given by [42]:



Tesis publicada con autorización del autor
No olvide citar esta tesis

$$\widehat{\boldsymbol{\Omega}} = \left(\boldsymbol{X}^{\boldsymbol{T}}\boldsymbol{X}\right)^{-1}\boldsymbol{X}^{\boldsymbol{T}}\boldsymbol{Y} \tag{2.18}$$

Where $\boldsymbol{X}^{\boldsymbol{T}}$is the transpose of $\boldsymbol{X}$ and $\widehat{\boldsymbol{\Omega}}$ is the matrix solution with the set of the estimated JO parameters $(\widehat{\Omega}_2, \widehat{\Omega}_4, \widehat{\Omega}_6)$. Once the JO parameters are determined, they can be used to calculate the line strength expression in Eq. (2.15).

$$S_{J\to J'}^{cal} = e^2 \sum_{j=2,4,6} \widehat{\Omega}_{(j)} \left|\left\langle 4f^n SLJ \middle\| U^{(j)} \middle\| 4f^n S'L'J' \right\rangle\right|^2 \tag{2.19}$$

The calculated line strength $S_{J\to J'}^{cal}$ is compared directly with the experimental line strength $S_{J\to J'}^{exp}$ of transition $J \to J'$ to measure the quality of the fit by the root mean square deviation error RMS:

$$RMS = \left[\frac{\sum_{J'}\left(S_{J\to J'}^{exp} - S_{J\to J'}^{cal}\right)^2}{N-3}\right]^{1/2} \tag{2.20}$$

Where $N$ is the number of the transitions and three is the number of the parameters $(\widehat{\Omega}_2, \widehat{\Omega}_4, \widehat{\Omega}_6)$ used in the fitting procedure. The error on a parameter is given by the product of the square root of the respective diagonal matrix element of the matrix $\left(\boldsymbol{X}^{\boldsymbol{T}}\boldsymbol{X}\right)^{-1}$ and the RMS desviation [42].

If the transition has partial MD contribution, the line strength $S_{SLJ\to S'L'J'}^{MD}$ must be first calculated and the $\Omega_{(j)}$ parameters are obtained minimizing the absolute difference $S_{J\to J'}^{exp} - \left(S_{J\to J'}^{ED} + S_{J\to J'}^{MD}\right)$.

$$S_{J\to J'}^{MD} = \frac{e^2 h}{16\pi^2 m_e^2 c^2} |\langle 4f^n SLJ || L + gS || 4f^n S'L'J' \rangle|^2 \tag{2.21}$$

Once the JO parameters are found, the calculations of the radiative lifetime, the spontanoeus emission probability and the branching ratio are straightforward using Eq. (2.4), Eq. (2.10) and Eq. (2.13) respectively.



Tesis publicada con autorización del autor
No olvide citar esta tesis

PONTIFICIA UNIVERSIDAD CATÓLICA DEL PERÚ

### 2.2.2 Judd-Ofelt parameters calculation from emission spectrum

After presenting the JO-analysis from absorption spectrum, it is important to note that the calculations require an accurate absortion coefficient spectra with well resolved absorption bands. However, in this work the biggest problem of the AlN:Tb thin film materials is the lack of an absorption coefficient with clear absoprtion bands in the spectra (see Figure 2.3). It will be discussed now.

In the case of a polished bulk material the absorption coefficient can be easily determined from the measured transmission spectrum using the Lambert's law. Figure 2.3 shows that for a doped bulk material (e.g. $LiTbF_4$ [49]) the transition bands of RE ions in the absorption coefficient spectra are in the order of $10^1\ cm^{-1}$.

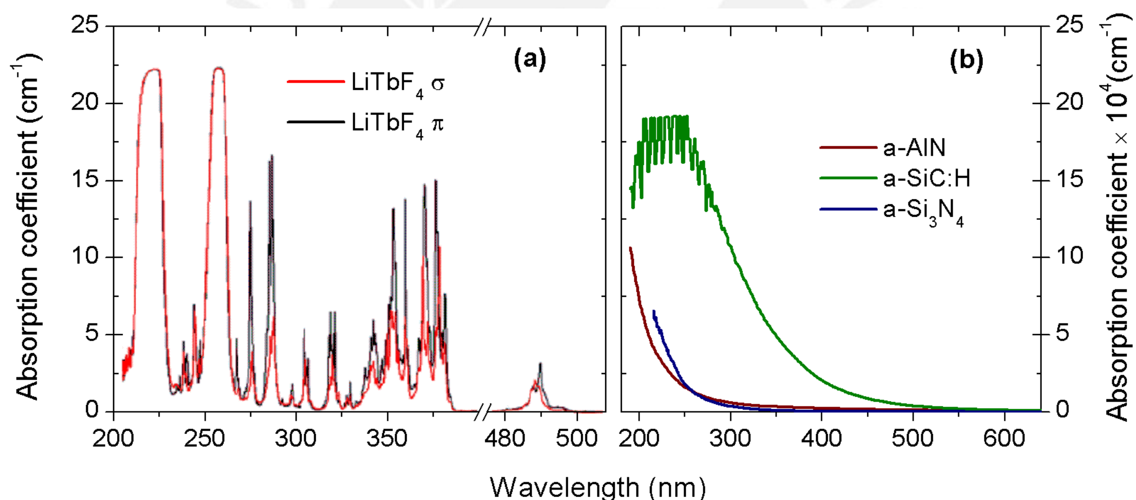


***Figure 2.3*** ***(a)*** *UV-VIS polarized absorption coefficient of* $LiTbF_4$*. Image modified from* [49]. ***(b)*** *Absorption coefficient of amorphous AlN,* $Si_3N_4$ *and SiC:H thin films deposited by radiofrequency magnetron sputtering at PUCP. Notice the different scales between the absorption coefficients of the RE doped bulk and the RE doped thin films.*

On the other hand, the thin film absorption coefficient can be calculated using the interference pattern present in the transmission spectrum [50]–[53]. This interference pattern comes from the thin thickness of the film (typically in the nanometer range) and the refractive behaviour of the light when it passes throught film and substrate. Figure 2.3 shows the absorption coefficient of amorphous thin film materials a-AlN, a- $Si_3N_4$ and a-SiC:H depending on the wavelength of the used light which are in the order of $10^4\ cm^{-1}$.



Tesis publicada con autorización del autor
No olvide citar esta tesis

PONTIFICIA UNIVERSIDAD CATÓLICA DEL PERÚ

Since the absorption of the host thin film material is $10^3$ times higher than the absorption bands due to the RE ion transitions, the small values of the absorption bands are not seen due to the highly absorbing a-AlN, a-$Si_3N_4$ and a-SiC:H host material. This is the main reason why in the case of a thin film material it is preferable to determine the JO parameters using the emission spectrum.

Now, this section continues the discussion with the outline of the expansion of the JO theory for emission spectra.

For a decay transition between two energy levels $|4f^nSLJ\rangle \rightarrow |4f^nS'L'J'\rangle$, the intensity of spontaneous light emission $I_{J\rightarrow J'}$ is proportional to the energy of the emitted photon $h\nu_{J\rightarrow J'}$, multiplied by the spontaneous transition probability $A_{J\rightarrow J'}$ [54]:

$$I(\nu_{J\rightarrow J'}) \propto h\nu_{J\rightarrow J'} A_{J\rightarrow J'} \tag{2.22}$$

But the transitions peaks in the measured emission spectra are not perfect lines; instead they present a sharp intensity peak form (see Figure 2.4). Thus, the total spontaneous emission probability of a transition can be estimated integrating the emission intensity divided by the energy of the emitted photon:

$$A_{J\rightarrow J'} \propto \int_{\nu_{min}}^{\nu_{max}} I_{mn}(\nu)(h\nu_{mn})^{-1}\mathrm{d}\nu \tag{2.23}$$

For simplicity the integral in Eq. (2.23) will be expressed as $\Gamma_{J\rightarrow J'}$. Then, the experimental branching ratios can be calculated from the ratio of the integrated intensity for each manifold transition to the sum of all the integrated intensity transitions, as follows:

$$\beta_{J\rightarrow J'}^{exp} = \frac{A_{J\rightarrow J'}}{\sum_{J'} A_{J\rightarrow J'}} \propto \frac{\Gamma_{J\rightarrow J'}}{\sum_{J'} \Gamma_{J\rightarrow J'}} \tag{2.24}$$

Combining Eq. (2.4) and Eq. (2.13) the experimental branching ratio is related to the radiative lifetime and the spontaneous emission probability as follows:

$$\beta_{J\rightarrow J'}^{exp} = A_{J\rightarrow J'}\tau_r \tag{2.25}$$



Tesis publicada con autorización del autor
No olvide citar esta tesis

Expanding the spontaneous emission probability in its ED and MD components, it is more obvious how the JO parameters are related to the experimental branching ratios by:

$$\beta^{exp}_{J\to J'}/\tau_r = A^{oe}_{J\to J'}\left(\sum_j \Omega_j \left|\langle U^{(j)}_{J\to J'}\rangle\right|^2\right) + A^{MD}_{J\to J'} \tag{2.26}$$

Where:

$$A^{ED}_{J\to J'} = A^{oe}_{J\to J'}\left(\sum_j \Omega_j \left|\langle U^{(j)}_{J\to J'}\rangle\right|^2\right) \tag{2.27}$$

$$A^{oe}_{J\to J'} = \frac{16\pi^3 e^2}{3\varepsilon_0 h(2J+1)\bar{\lambda}^3}\frac{n^2(n^2+2)^2}{9} \tag{2.28}$$

And $A^{MD}_{J\to J'}$ given by Eq. (2.12).

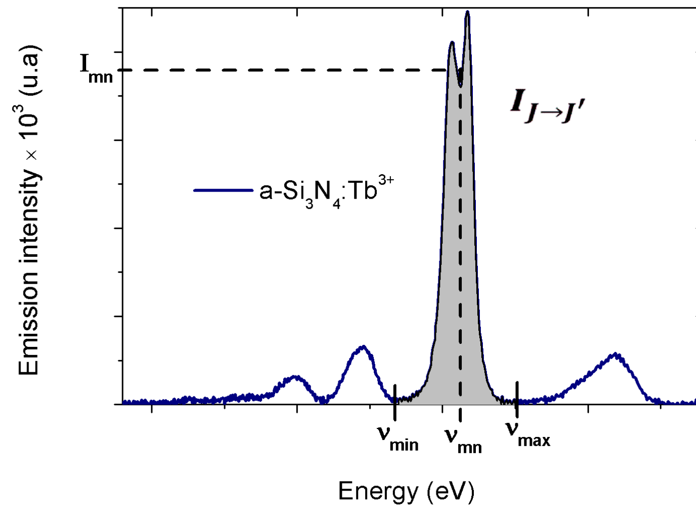


***Figure 2.4*** *Scheme of the integration* $\int \boldsymbol{I_{JJ'}(\nu)\nu^{-1}d\nu}$ *for each emission peak, which is proportional to the spontaneous emission probability of a* $\boldsymbol{J \to J'}$ *transition Image modified from* [55].

If the radiative lifetime is also expanded in terms of the JO parameters, Eq. (2.26) becomes rather cumbersome. In order to explain this situation consider Eq. (2.29) where the reciprocal of the radiative lifetime is expressed as $1/\tau_r = \xi^{(2)}\Omega_2 + \xi^{(4)}\Omega_4 + \xi^{(6)}\Omega_6 + \xi^{(MD)}$.

$$\sum_{j=2,4,6}\left(A^{oe}_{J\to J'}\left|\langle U^{(j)}_{J\to J'}\rangle\right|^2 - \xi^{(j)}\beta^{exp}_{J\to J'}\right)\Omega_j = \xi^{(MD)}\beta^{exp}_{J\to J'} - A^{MD}_{J\to J'} \tag{2.29}$$



Tesis publicada con autorización del autor
No olvide citar esta tesis

TESIS PUCP

PONTIFICIA UNIVERSIDAD CATÓLICA DEL PERÚ

Then, the system of equations for $N$ observed transitions $J \rightarrow J'$ can again be written in a matrix form like $\boldsymbol{M\Omega} = \boldsymbol{b}$ to find the JO parameters by a least square matrix operation. However, this approach fails to give positive JO parameters with physical meaning, as a consequence of possible negative values for the matrix elements:

$$M_{jJ'} = A^{oe}_{J\rightarrow J'} \left|\langle U^{(j)}_{J\rightarrow J'}\rangle\right|^2 - \xi^{(j)} \beta^{exp}_{J\rightarrow J'} \quad (2.30)$$

$$b_{J'} = \xi^{(MD)} \beta^{exp}_{J\rightarrow J'} - A^{MD}_{J\rightarrow J'} \quad (2.31)$$

In order to avoid meaningless negative values for the JO parameters, Eq. (2.26) can be rewritten in a matrix form given by Eq. (2.32); where the squared matrix elements $(|\langle 4f^n SLJ||L + gS||4f^n S'L'J'\rangle|^2)$ of the MD operator in $A^{MD}_{J\rightarrow J'}$ were replaced by the letters $k_{J\rightarrow J'}$ for each $J \rightarrow J'$ transition and the radiative lifetime was replaced by the letter $y$. These letters become minimizing parameters to find the JO parameters.

$$\sum_{j=2,4,6} \left( A^{oe}_{J\rightarrow J'} \left|\langle U^{(j)}_{J\rightarrow J'}\rangle\right|^2 \right) \Omega_j = \frac{\beta^{exp}_{J\rightarrow J'}}{y} - A^{MD}_{J\rightarrow J'}(k_{J\rightarrow J'}) \quad \rightarrow \quad \boldsymbol{M\widehat{\Omega}} = \boldsymbol{b} \quad (2.32)$$

$$\boldsymbol{M} = \begin{bmatrix} A^{oe}_1 \left|\langle U^{(2)}_1\rangle\right|^2 & A^{oe}_1 \left|\langle U^{(4)}_1\rangle\right|^2 & A^{oe}_1 \left|\langle U^{(6)}_1\rangle\right|^2 \\ A^{oe}_2 \left|\langle U^{(2)}_2\rangle\right|^2 & A^{oe}_2 \left|\langle U^{(4)}_2\rangle\right|^2 & A^{oe}_2 \left|\langle U^{(6)}_2\rangle\right|^2 \\ \vdots & \vdots & \vdots \\ A^{oe}_N \left|\langle U^{(2)}_N\rangle\right|^2 & A^{oe}_N \left|\langle U^{(4)}_N\rangle\right|^2 & A^{oe}_N \left|\langle U^{(6)}_N\rangle\right|^2 \end{bmatrix} \qquad J \rightarrow J' = 1,2,3 \ldots N \quad (2.33)$$

The matrix elements of $\boldsymbol{M}$ are undoubtedly positive values and depends on the doubly reduced matrix elements $\left|\langle U^{(j)}_{J\rightarrow J'}\rangle\right|^2$ whose values can be found in Kaminiskii [45].

$$\boldsymbol{b} = \begin{bmatrix} \beta^{exp}_1/y - A^{MD}_1(k_1) \\ \beta^{exp}_2/y - A^{MD}_2(k_2) \\ \vdots \\ \beta^{exp}_N/y - A^{MD}_N(k_N) \end{bmatrix} \qquad J \rightarrow J' = 1,2,3 \ldots N \quad (2.34)$$

The reason for considering the squared matrix elements $|\langle 4f^n SLJ||L + gS||4f^n S'L'J'\rangle|^2$ minimizing parameters $k_{J\rightarrow J'}$ is to avoid the problem of unknown suitable intermediate coupling wavefunctions for the matrix elements calculation. These wavefunctions depends on



Tesis publicada con autorización del autor
No olvide citar esta tesis

PONTIFICIA UNIVERSIDAD CATÓLICA DEL PERÚ

the specific RE and host material combination. They can be calculated on the basis of a weak-field crystal field model of the RE in a host, taking into account the influence of the surroundings on the spin-orbit coupling strength by applying a fit of the spin-orbit parameters to a set of experimental ${}^{2S+1}L_J$ multiplet energies [41]. However, the complex calculations are not necessary as long as the magnetic contribution can be estimated by minimizing Eq. (2.37).

The matrix $\widehat{\mathbf{\Omega}}$ is the matrix of the least-squares estimates JO parameters calculated in the same manner as Eq. (2.18). But now, the estimated JO parameters are function of the minimizing parameters $k_{1,2\ldots N}$ and $y$.

$$\widehat{\mathbf{\Omega}} = (\boldsymbol{M}^T\boldsymbol{M})^{-1}\boldsymbol{M}^T\boldsymbol{b} \quad \longrightarrow \quad \widehat{\mathbf{\Omega}} = \widehat{\mathbf{\Omega}}(y, k_1, k_2 \ldots k_N) \tag{2.35}$$

The radiative lifetime equation can now be expressed as a function of the JO parameters variables $k_{1,2\ldots N}$ and $y$. Even more, the same radiative lifetime is a minimizing parameter $y$.

$$\tau_r = \sum_{J'}^{N}\left(A^{oe}_{J\to J'}\sum_{j=2,4,6}\left(\widehat{\mathbf{\Omega}}_j(y, k_1, \ldots k_N)\left|\langle U^{(j)}_{J\to J'}\rangle\right|^2\right) + A^{MD}_{J\to J'}(k_{J\to J'})\right) = y \tag{2.36}$$

$$\chi^2 = \left(y - \frac{1}{A^{Total}(y, k_1, \ldots k_N)}\right)^2 \tag{2.37}$$

The problem is reduced to find the parameters $y, k_1, \ldots k_N$ that minimize the estimator $\chi^2$ defined by Eq. (2.37) as the difference between the unknown radiative lifetime parameter $y$ and its own analytical expression in function of the minimizing parameters $k_i$ and $y$ itself. Due to the complexity of the equation and the multiple solutions for the parameter values that not necessarily have physical meaning, it is necessary to give appropriate restrictions to perform the minimization. The most important condition is to require that the minimizing parameters $y, k_i$ take values that replaced in the JO parameter expression makes them positive values. Also the minimizing parameters themselves must be positive values since they represent the radiative lifetime and the squared matrix elements of the MD contribution for the $J \to J'$ transitions respectively.

The error on the Judd-Ofelt parameter is given by the product of the square root of the respective diagonal matrix element of the matrix $(\boldsymbol{M}^T\boldsymbol{M})^{-1}$ and the RMS deviation calculated as follows:



Tesis publicada con autorización del autor
No olvide citar esta tesis

$$RMS = \left[ \frac{\sum_{J'} \left( \beta_{J \to J'}^{exp} - \beta_{J \to J'}^{cal} \right)^2}{N - n} \right]^{1/2} \tag{2.38}$$

Where $N$ is the number of transitions and $n$ is the number of parameters used in the minimizing procedure.

The proposed method has been implemented in Mathematica 9.0 to perform the complex calculations and find the variables $y, k_1, k_2 \ldots k_N$ that minimize the value of the $\chi^2$ estimator. This method requires three input information: the experimental branching ratios calculated from the emission spectrum band transitions, the mean wavelength calculated for each transition peak and the refractive index of the host material. The material science group of the PUCP implemented a program to calculate the peak areas. In the present work, it has been further modified to obtain from the measured spectra (i) the integral of the emission intensity multiplied by the energy of the emitted photon and (ii) the mean transition wavelength.

## 2.3 Cathodoluminescence activation

This section addresses the generation of light from the optically active centers as the result of electron bombardment. This technique is known as cathodoluminescence (CL) and has become a widely used tool to characterize the optical properties of semiconductor materials [56], [57] and is used in this work to obtain emission spectra.

### 2.3.1 Electron beam interactions

The following is a brief description of the theory of cathodoluminescence which closely follows the explanations by Boggs and Krinsley [58] as well as Ozawa [59].

When an electron beam impinges on a material, a large part of the incident electrons penetrate into the material and the rest is ejected as back-scattered electrons. After elastic



Tesis publicada con autorización del autor
No olvide citar esta tesis

TESIS PUCP

PONTIFICIA UNIVERSIDAD CATÓLICA DEL PERÚ

and inelastic collisions, the energy of the penetrating electrons is converted into X-rays, auger electrons, secondary electrons, electron-hole pairs and phonons (see Figure 2.5(a)). The secondary electrons inside the crystal form the electron plasma (plasmon) which excites the lattice ions and produces electron-hole pairs during energy loss process along its trajectory inside the crystal.

Considering the band theory of solids (see reference [60] for details) in insulator and semiconductors when sufficient energy is applied (which is practically always the case for CL excitation), the electrons can be promoted from the valence band to the conduction band, leaving behind a “hole” (see Figure 2.5(b)). However, the electrons only remain a short time in the conduction band before undergoing de-excitation and return to the valence band. Since the solid is far from being a perfect crystal, discrete energy levels arises in the band gap due to lattice defects or impurity ions. These defects trap the electron as they move through the band gap to lower energy states in the valence band, with the consequent emission of photons.

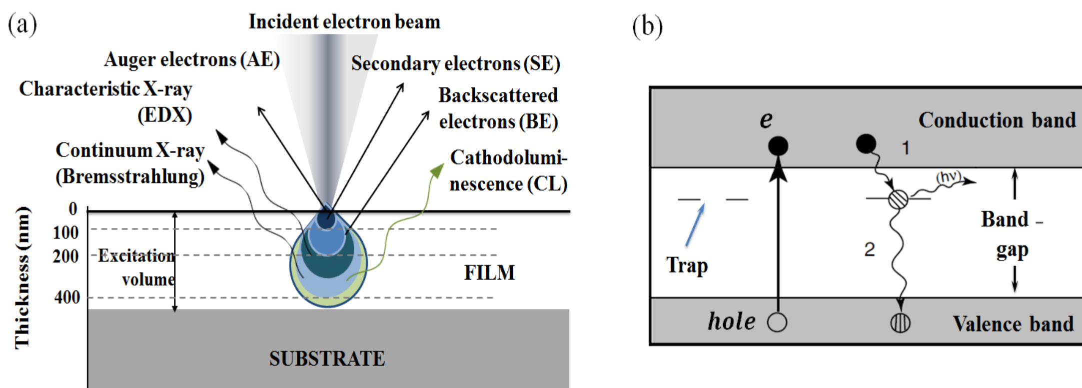


***Figure 2.5*** *(a) Interaction volume of an electron beam and the penetration depth. Image modified from* [61]. *(b) Schematic representation of the excitation process of RE ion centers. Image modified from* [58].

### 2.3.2 Direct and indirect excitation of RE ions by incident electrons

The excitation processes of RE ions can generally be divided into two categories, direct and indirect excitation processes. The direct excitation of a RE ion is a process of excitation of the $4f$ electrons by the incident electrons However, the cross section of the RE ion is too low that reduces the probability to occur direct excitation and does not explain the high light emission.



Tesis publicada con autorización del autor
No olvide citar esta tesis

PONTIFICIA UNIVERSIDAD CATÓLICA DEL PERÚ

The indirect excitation process occurs via transfer of energy to the $4f$ electrons system from the electron-hole (EH) pairs generated [62]. This EH pairs are produced when the electron energy of the incident beam into the solid promotes the carriers from the valence band to the conduction band. This mechanism of excitation is more probable to occur and will be explained now.

The process by which mobile EH pairs are lost is called recombination. Recombination centers are of two types: activator ions (e.g. RE ions) and lattice imperfections (e.g. vacancies, dislocations, etc.). The elimination of the EH pairs, release energy in a competitive process between radiative and non-radiative recombination. Non-radiative recombination releases energy by phonon emission or lattice vibration and occurs when the EH pair are trapped by impurities or crystal lattice defects. On the other hand, radiative recombination occurs when the produced EH pairs move through the host lattice until they get trapped by the activator (e.g. the RE ion). Thus, the CL intensity, is governed by the efficiency of the EH pair migration to find the RE ion, and the trapping of this EH pair by the RE ion [63]. The CL spectrum is characterized by intensity and emission wavelengths positions (color) which are determined by the nature of the RE ions and its host material. A good combination of RE ions and host matrix determines the bright features of the CL spectra. Some useful ways to enhance the intensity emission are discussed in section 2.5.

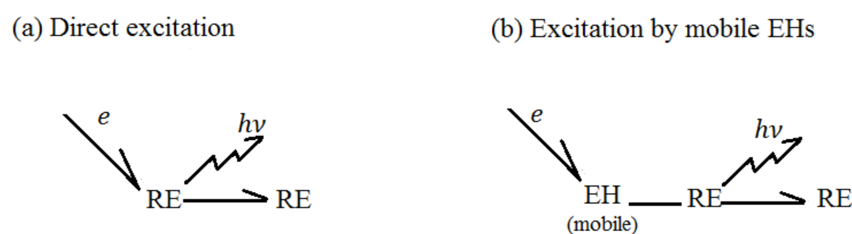


***Figure 2.6***. *Scheme for (a) directly and (b) indirectly luminescence arising from recombination of mobile electron-hole pairs (EHs). Image from* [59].



Tesis publicada con autorización del autor
No olvide citar esta tesis

TESIS PUCP

PONTIFICIA UNIVERSIDAD CATÓLICA DEL PERÚ

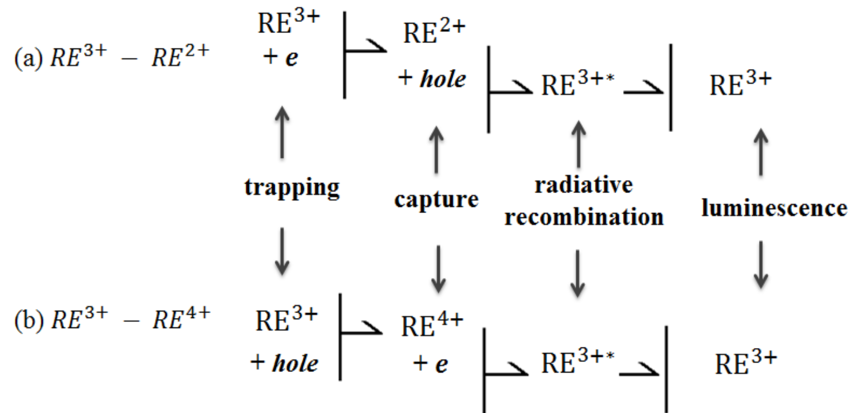


***Figure 2.7**. Proposed model for the recombination mechanism of electrons and holes (a) for ($RE^{3+}$) and ($RE^{2+}$) rare earth ions (b) for ($RE^{3+}$) and ($RE^{4+}$) rare earth ions. Image modified from* [59].

A model was proposed for the recombination mechanism of EH pairs at activator ions. As it is shown in Figure 2.7 the $RE^{3+}$ first trap an electron and becomes $RE^{2+}$ generating a negatively charged local field, which attracts a hole and captures it to become an excited state $RE^{3+*}$. Finally, after a holding time in the excited state, the $RE^{3+}$ emits a photon and returns to the ground state. If the hole is first trapped, the $RE^{3+}$ becomes $RE^{4+}$ producing a positively charged local field. An electron can be captured by the $RE^{4+}$ to form an excited $RE^{3+*}$ ion, which returns to the ground state after emitting a photon. Although, several attempts to explain the CL mechanism of luminescence centers have been proposed [64]–[66], investigations continues due to the complexity of the luminescence process which involves several steps between incidence and final emission of light.

## 2.4 Properties of the investigated material systems from the perspective of the application in luminescent devices

This section presents an overview of the properties and luminescent characteristics of the materials used in this work to produce the thin films: aluminum nitride semiconductor (host) and terbium ions (doped material).



Tesis publicada con autorización del autor
No olvide citar esta tesis

### 2.4.1 Aluminum nitride

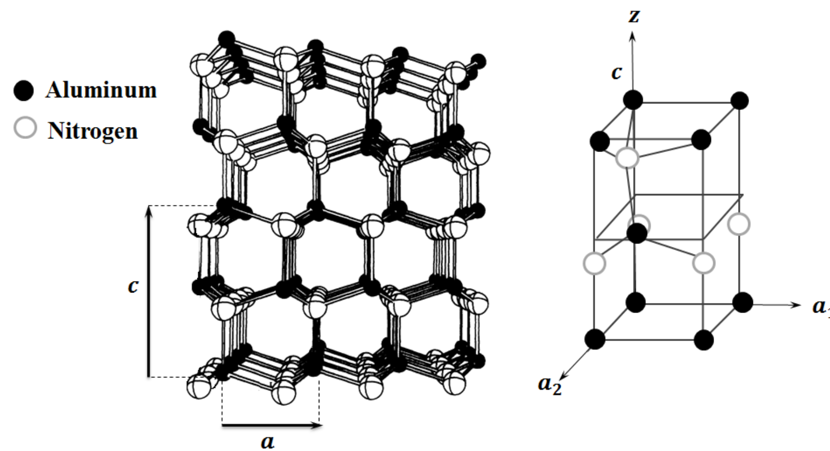


***Figure 2.8*** *The wurtzite structure has a hexagonal unit cell which consists of two interpenetrating hexagonal closed packed (hcp) lattices. Image left in* [$\mathbf{11\bar{2}0}$] *projection modified from* [68].

Aluminum nitride is one of the nitride semiconductors with optimal optical and electrical properties. The main characteristics of AlN properties are summarized in Table 2.1. A well know property unique for AlN is its direct wide band gap (~ 6.2 eV) suitable for study optical and luminescence properties of elements in the UV and visible wavelength. Because of these properties AlN is used as host for a variety of luminescent material [67], e.g. LEDs, laser diodes, etc.

One big drawback is the high reactivity of aluminum nitride with oxygen during its growth by deposition or by heating in the presence of oxygen. Shen *et al*. [69] pointed the problem of non-ultrahigh vacuum conditions out indicating that the oxygen comes from adsorbed gas molecules on the substrate and the inner wall of the vacuum chamber, gas leaks, and residual vacuum. It was found that the oxygen concentration increases in samples with low N:Al ratio, but decreases with high bias voltage applied to the substrates. Oxygen contamination declines the quality of AlN leading to deviations of the energy bandgap measured and the lattice constant from the theoretical values [70]. García-Méndez [71] found the effect of oxygen is band gap broadening, for AlN with oxygen gas introduced during deposition, calculated bang gap was of $E_g$= 7.95 eV, a value slightly higher than $E_g$= 6.6 eV for polycrystalline AlN deposited using an atmosphere of argon and nitrogen.



Tesis publicada con autorización del autor
No olvide citar esta tesis

The thermodynamically stable hexagonal wurtzite structure of aluminum nitride (see Figure 2.8) has a molar mass of $40.988\ g\ mol^{-1}$, the reported lattice parameters is about $3.110$ Å for the $a$ parameter and about $4.978$ Å for the $c$ parameter [70]. However, for the ideal wurtzite structure the expected ratio $c/a = 1.633$ suffers deviation from this value indicating the coordination of each atom is a distorted tetrahedron with three equal bonds forming aluminum nitrogen layers and a fourth slightly longer bond in the $c$ direction [68]. For AlN the ratio $c/a$ is$1.600$.

***Table 2.1*** *Basic parameters of polycrystalline wurtzitic AlN at 300K* [67], [72]

| | |
|---|---|
| Number of atoms per $cm^{-3}$ | $9.58 \times 10^{22}$ |
| Density $(gcm^{-3})$ | $3.23$ |
| Bandgap energy $(eV)$ direct | $6.2$ |
| Breakdown field $(Vcm^{-1})$ | $(1.2 - 1.8) \times 10^{6}$ |
| Dielectric constant static | $8.5 \pm 0.2$ |
| Dielectric constant, high frequency | $4.68$ |
| Mobility electrons $(cm^{2}V^{-1}s^{-1})$ | $300$ |
| Mobility holes $(cm^{2}V^{-1}s^{-1})$ | $14$ |
| Resistivity $(\Omega cm)$ | $10^{11} - 10^{13}$ |
| Index of refraction | $2.15\ \pm 0.5$ |
| Young's modulus $(GPa)$ | $265$ (longitudinal) $- 44.2$ (transversal) |
| Melting point $(K)$ | $3100$ |
| Thermal conductivity$(Wcm^{-1}K^{-1})$ | $2.60$ |
| Thermal expansion coefficient $(K^{-1})$ | $4.6 \times 10^{-6}$ |

The thermal conductivity of AlN ($320\ W/m \cdot K$) is higher than 6H-SiC ($270\ W/m \cdot K$), and close to that of copper ($398\ W/m \cdot K$) [73]. The electrical resistivity of AlN is $\rho = 10^{11} - 10^{13}\ \Omega\ cm$ and depends a lot on the impurity-doping content [70]. This combined high thermal conductivity and high electrical resistivity made AlN an appropriate material for thermal management in electronic devices.

### 2.4.2 Terbium doped aluminum nitride

Among the various RE ions, $Tb^{3+}$ has caused particular interest in the photonic field for the development of efficient green emitting materials [74]. In the trivalent terbium ion, the electronic configuration $[Xe]4f^{8}$ indicates the $6s$ electrons and the possible $5d$ electron have



Tesis publicada con autorización del autor
No olvide citar esta tesis

been lost [75]. The number of electrons in the $4f$ orbital can be distributed in various energy levels. Figure 2.9 shows the different energy levels that are of current interest for the trivalent Tb ion. The optical properties of $Tb^{3+}$ has been experimentally studied as an activator ion in several host materials (e.g. phosphors [76], [77], ceramics [78], [79], thin film nitride semiconductors [55], [80]–[83] and fluoroborate glasses [84], [85]). The emission spectrum of Tb doped amorphous AlN sample deposited by RF magnetron sputtering is presented in Figure 2.10. The green luminescence, attributed to the $4f^8 \rightarrow 4f^8$ transitions, consists of four bands corresponding to the manifold transitions from the $^5D_4$ multiplet to the different $^7F_J$ $(J = 0,1,2 \ldots 6)$ multiplets [86].

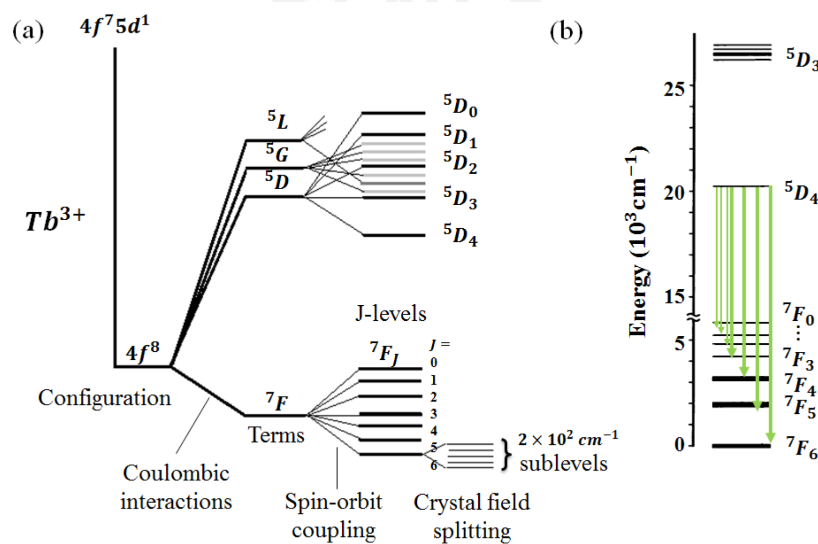


***Figure 2.9*** *(a) Diagram representing the interactions leading to the splitting of the electronic energy levels of $Tb^{3+}$ (b) Energy diagram for the green emission of $Tb^{3+}$. Image modified from* [87].

In Figure 2.10 the three transitions $^5D_4 \rightarrow {}^7F_{2,1,0}$ corresponding to 649, 671 and 680 nm respectively, are not seen in the CL spectra due to the weakness of these emission lines. The $^5D_4 \rightarrow {}^7F_{6,4,3}$ transitions are stronger suggesting moderate sensitivity to the host environment [88]. The transition $^5D_4 \rightarrow {}^7F_5$ at approximately 550 nm has been found to be the strongest. This occurs in nearly all host crystals, probably due to the induced electric dipole and magnetic dipole contribution involved in the $^5D_4 \rightarrow {}^7F_5$ transition [54]. Additional magnetic dipole contribution can be present also in the $^5D_4 \rightarrow {}^7F_3$ [88], [89] and $^5D_4 \rightarrow {}^7F_6$ [90], [91] transitions.



Tesis publicada con autorización del autor
No olvide citar esta tesis

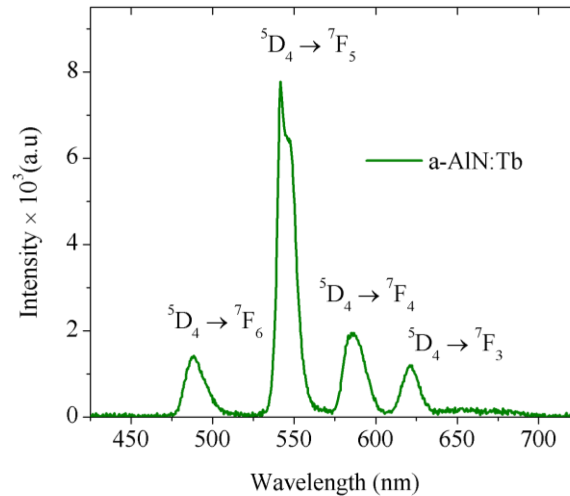


***Figure 2.10*** *CL emission spectra of a-AlN: Tb grown by radio frequency magnetron sputtering. The observed transitions correspond to the energy levels of the free Tb ion. Image modified from* [55].

## 2.5 Concentration quenching and thermal activation of RE ions doped materials

The emission intensity of RE luminescent materials depends on the annealing temperature and the doping concentration [55], [80]. Initially, as the RE ions dopant concentration in a given material increase, the emitted light intensity also increases due to higher number of emission centers. However, this behavior continues only until a critical concentration value is reached. Above this value the emission intensity starts to drop. This reduction in the emission intensity at high dopant concentration is called concentration quenching (see Figure 2.11 (a)). In such a situation the probability to reach a path of non-radiative decay is strongly enhanced [80].

The main mechanisms explaining this effect are the donor-killer energy migration and cross-relaxation. In the first mechanism, the high concentration of luminescence centers reduce the distance between them and also lays a path for the excitation energy to find a defect or impurity ion that acts like a killer and dissipates energy in a non-radiative way. The cross-relaxation mechanism accounts for the resonant energy transfer between to identical adjacent centers. The critical distance from the concentration quenching follows the equation [92]:



Tesis publicada con autorización del autor
No olvide citar esta tesis

$$R_c = 2\left(\frac{3V}{4\pi x_c N}\right)^{1/3} \tag{2.39}$$

Where $x_c$ is the critical concentration estimated where the emission intensity begin to decrease quickly, $N$ the number of RE ions in the host unit cell, and $V$ is the volume of the unit cell. Usually the critical distance is determined to be about few angstroms (e.g. 8.05 Å for Eu [92], 7.22 Å for Tb [93])

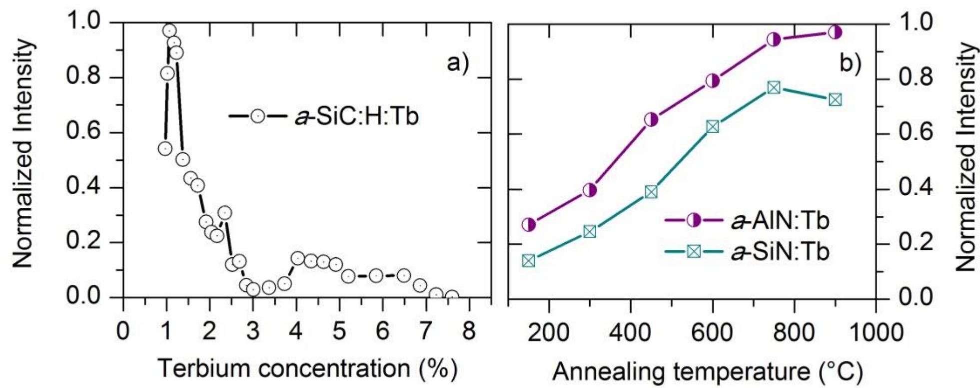


***Figure 2.11*** *Normalized integrated CL intensity versus (a) the atomic concentration of Tb (Image modified from*[80]*) and (b) the annealing temperatures of different Tb doped matrices (Image modified from*[55]*). Only the* $^7F_5$ *transition was used.*

The emitted light intensity varies with annealing temperature in two independent processes (see Figure 2.11 (b)). First one observes an enhancement of the emission intensity after thermal annealing treatments, which suggest a thermal activation process of the luminescence centers. The possible activation mechanisms are still under discussion [32], [94], [95]. For Tb doped amorphous AlN and $Si_3N_4$ thin films, a phonon assisted energy transfer mechanism between electronic defects and the Tb ions was proposed [55]. On the other hand, experiments on Er ions incorporated on amorphous hydrogenated silicon suboxides (*a*-$SiO_x$:H) suggested that increasing oxygen content can provides a better local environment for the emission intensity [96]. When a critical annealing temperature is reached a second behavior of decreasing light emission intensity occurs. This is called thermal quenching and it may result by a weakening of the excitation efficiency and by predominant non-radiative decay channels. Investigations have been conducted trying to elucidate the non-radiative mechanisms for quenching process such as multi-phonon emission from the 4f-5d excited state to the 4f ground state [97] and thermal ionization [98].



Tesis publicada con autorización del autor
No olvide citar esta tesis

TESIS PUCP

PONTIFICIA UNIVERSIDAD CATÓLICA DEL PERÚ

# 3 Experimental details

This chapter gives a description of the sputtering production of AlN:Tb thin films, the annealing treatments performed and the characterization techniques used to investigate the luminescence spectra, composition and structure of the produced samples. The experimental setup and the parameters used are described in detail in each case.

## 3.1 Film deposition and annealing

All AlN:Tb films were deposited on polished silicon (Si) substrates with orientation (001) using a double RF magnetron sputtering system. The deposition conditions are listed in Table 3.1. The substrates were cooled down with a constant water flux at 12°C to enforce the amorphous state of the layers. However, it has been found by XRD analysis the presence of crystalline AlN phases in the produced films. Moreover, the EDX analysis shows a 30 at.% of oxygen content in the as deposited film, which suggests the presence of an amorphous aluminum oxide phase in the film. Although the produced films present also an aluminum oxide phase, they will be referred as AlN:Tb through the thesis since it was the initial intention of this work. The sputtering deposition was performed in a nitrogen and argon mixture atmosphere of purity 5N, respectively. The target of AlN bulk crystal (with oxygen impurity below 90 ppm) and the Tb target of 3N (*) purity were sputtered simultaneously at different RF powers. In order to clean the surface of the target materials, a pre-sputtering process of 15 min was done first.

***Table 3.1*** *Sputtering conditions used for the prepared AlN:Tb thin films with a thickness of about 600 nm.*

| ***Sample*** | ***Substrate*** | ***Target*** | ***Basic Pressure*** $\times 10^{-6}\,mbar$ | ***Sputtering ambient*** | ***Power*** $(W)$ | ***Pressure of plasma formation*** $\times 10^{-2}\,mbar$ |
|---|---|---|---|---|---|---|
| AlN:Tb | Si (001) | AlN<br>Tb | 2.03 – 3.7 | Ar/$N_2$<br>35:5 sccm | 100 (AlN)<br>15 (Tb) | 6.15-6.34 |

The as-deposited AlN:Tb film samples were annealed using rapid thermal processing (RTP) with a constant $N_2$ flux of 4000 sccm of purity 5N. The heating rate was 20 K/s and the holding time at heist temperature was 5 min. Two kinds of heating were applied: a single step annealing

(*) The purity not considering other RE ions is better than 5N.



Tesis publicada con autorización del autor
No olvide citar esta tesis

TESIS PUCP

PONTIFICIA UNIVERSIDAD CATÓLICA DEL PERÚ

where samples were exposed directly to temperatures of 500°C, 750°C, 900°C and 1000°C, and a multi-step annealing where samples were heated from the as deposited state directly to 500°C, it was left to cool down and then again heated directly to 750°C, it was left to cool down again and heated directly to 900°C, and so on until 1000°C. A second annealing treatment in a quartz tube furnace (QTF) was also applied using the single step heating procedure. The reason for all these different annealing treatments is to study how they affect the structure and the luminescence of the films.

***Table 3.2*** *Annealing treatments used for the prepared AlN:Tb thin films.*

| RTP single step | RTP multi-step | QTF single step |
|---|---|---|
| RT (*) | RT | RT |
| RT – 500 °C | RT – 500 °C | RT – 500 °C |
| RT – 750 °C | 500 °C – 750 °C | RT – 750 °C |
| RT – 900 °C | 750 °C – 900 °C | RT – 900 °C |
| RT – 1000 °C | 900 °C – 1000 °C | RT – 1000 °C |

(*) RT: room temperature

## 3.2 Film structure, composition and light emission characterization

***X-ray diffraction***

The structure of the samples was investigated by X-ray diffraction (XRD, Bruker D 5000 Theta-Theta with Goebel mirror) at U=40 kV and I=40 mA. Instead of the conventional Bragg-Brentano geometry, a grazing-incidence set up (see Figure 3.1) was applied with a parallel beam. This is especially useful for thin films to limit the incidence of the X-ray beam to the surface, and therefore enhance the sensitivity to obtain a better signal and less presence of the interfering effect of the substrate. The used Cu K-alpha radiation had a wavelength of 0.15418 nm, the incidence angle was 3° and the scanning angle $2\theta$ varied in the range from 20 to 100 degrees. The step size was 0.020° and the time step was 1.3 seconds.



Tesis publicada con autorización del autor
No olvide citar esta tesis

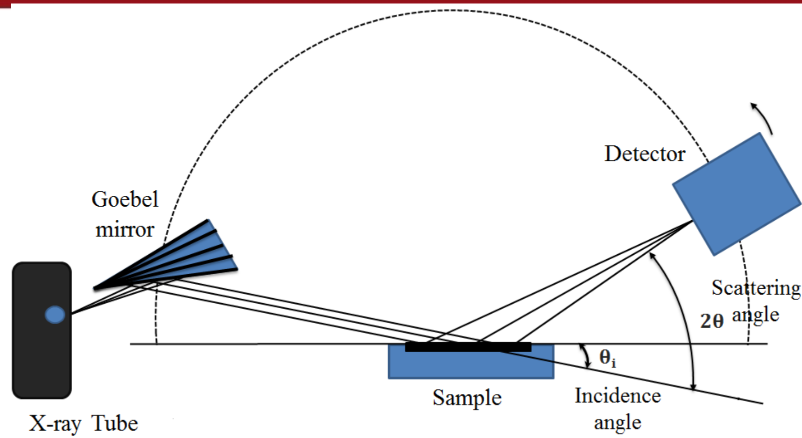


***Figure 3.1*** *The grazing-incidence set up, the divergent beam of an X-ray tube is converted into a parallel beam by applying a graded multilayer Goebel mirror.*

***Scanning electron microscopy with EDX***

The surface morphology was examined with a Scanning Electron Microscope (SEM, Hitachi S 4800) equipped with a field emission gun and using an accelerating voltage of U=30kV. The SEM micrographs were obtained at 0° tilt, with a normal incidence of the electron beam.

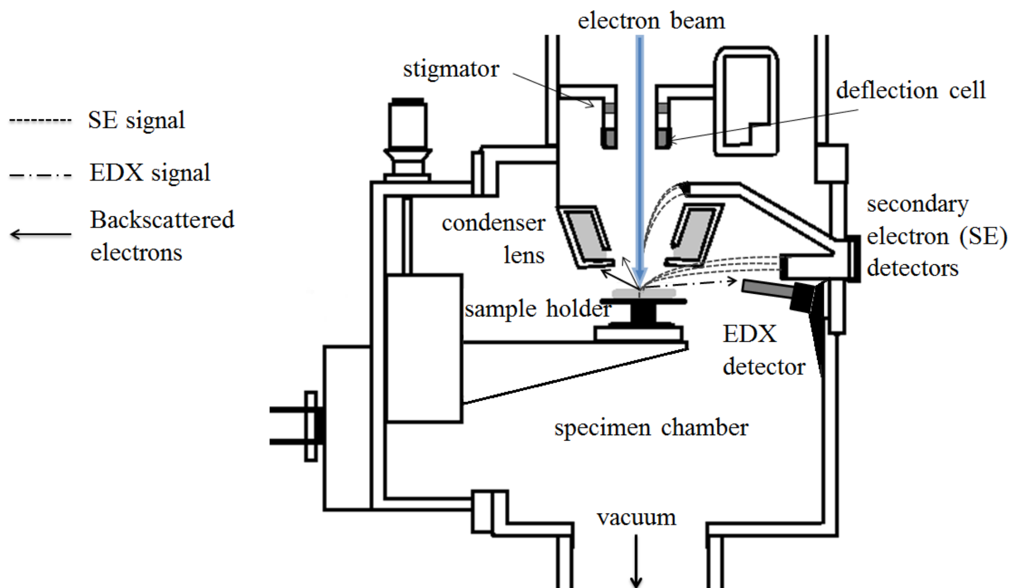


***Figure 3.2*** *Schematic drawing of a combined SEM and EDX set up.*

Using the SEM Philips XL30 coupled with Energy Dispersive X-ray analysis (EDX), the elemental composition of the thin film samples was determined and the approximate concentration of each element was found. A schematic drawing for the SEM-EDX configuration is given in Figure



Tesis publicada con autorización del autor
No olvide citar esta tesis

3.2. The EDX current density was maintained at 5 kV for a small penetration depth (less than 1 micrometer) in order to reduce the contribution of the silicon substrate in the measurement.

***RHEED-analysis and CL-measurements***

For a qualitative confirmation of the crystallinity of the AlN:Tb films and its evolution after annealing treatments, RHEED (Reflection high-energy electron diffraction) was used. An electron beam is directed to the film surface at a grazing incidence angle from 1° to 10°. The incidence angle varied due to the rotation motion of the sample position in order to obtain different crystallographic plane images. The diffraction pattern is formed using Ewald construction by projecting the reciprocal lattice rods until they intersect the Ewald sphere (see Figure 3.3), the result is a series of high intensity points on a dark background [99].

Due to the very low angle of incidence of the electron beam, RHEED analysis has a very low penetration depth into the material. Thus, it gives information about the crystallographic orientation only at the surface.

The RHEED pattern for surface structure characterization was monitored using a CCD in a solid source molecular beam epitaxy MBE system (UMS 500 Balzers SSMBE) equipped with a RHEED system. At the same time the RHEED electron gun was used to perform cathodoluminescence (CL) excitation for light emission characterization of the films produced. Figure 3.4 shows a scheme of the CL and RHEED set up in the MBE chamber.

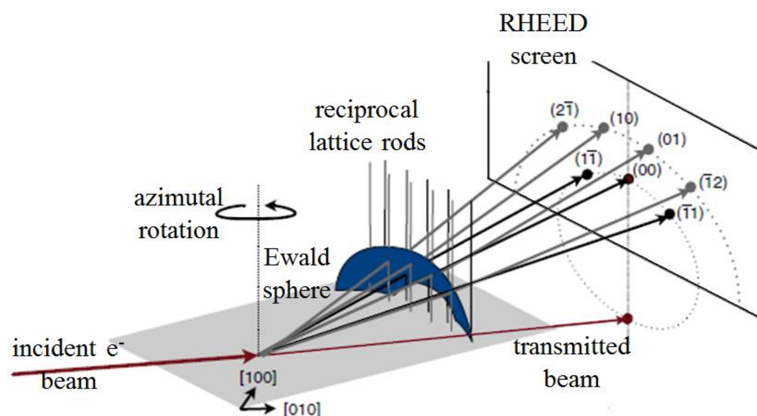


***Figure 3.3*** *Scheme of the basic geometrical set up of RHEED with the Ewald sphere construction highlighted. Imagen modified from* [99].



Tesis publicada con autorización del autor
No olvide citar esta tesis

PONTIFICIA UNIVERSIDAD CATÓLICA DEL PERÚ

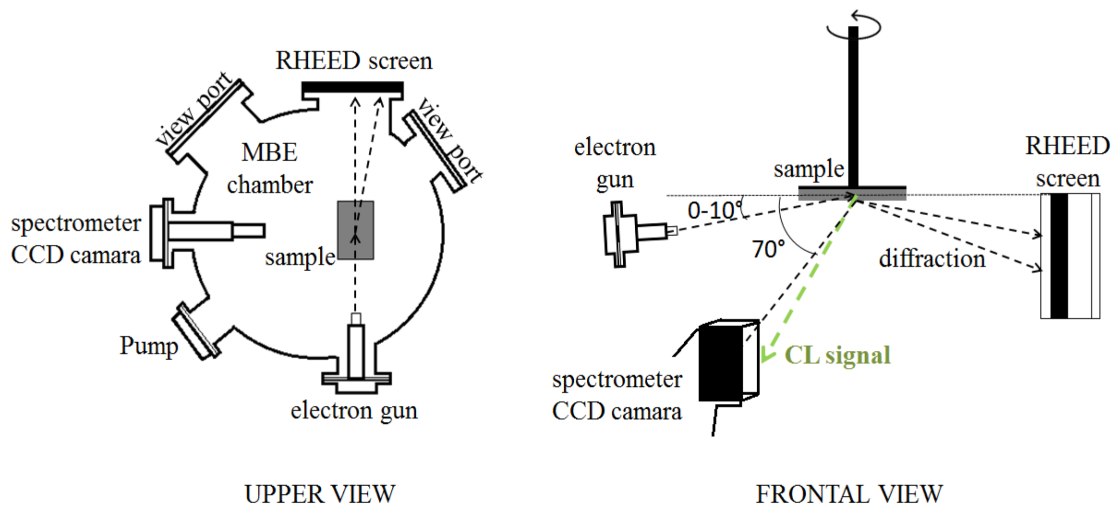


***Figure 3.4*** *Schematic drawing of a RHEED set up with CL spectrometers.*

The CL emission experiments were performed at room temperature in a vacuum chamber at a pressure of about $4\times10^{-9}$ mbar. Films were excited with electron beam accelerating voltage of 30 kV and a beam current between 1.6-1.7 A. Due to the high value of the mean free path of high energy electrons, CL and RHEED measurements were done in grazing incidence to have only access to the structure of the surface atomic planes in the film, avoiding completely the substrate. In the experiment the electrons dipped at low angle between 1° to 10°. For the CL measurements, the Spectrograph Thermo Oriel, Model 77441 with a CCD Array Spectrometer DB401-UV was placed at an angle of 70° from the normal to the sample surface. The spectral range covers from 190 to 800 nm, the grating density was of 285 lines/mm and the measurement slit was set to 100 μm. It gives a resolution at 546 nm of 0.45 nm.



Tesis publicada con autorización del autor
No olvide citar esta tesis

PONTIFICIA UNIVERSIDAD CATÓLICA DEL PERÚ

# 4 Results and Discussion

This chapter is divided in three main sections. The first section shows the results of testing the accuracy of the proposed method to recover the radiative parameters reported in literature. In the second section luminescence analysis results are presented and the calculated radiative lifetime values are discussed. In the third section results concerning the structure, phases, composition and surface morphology are shown and discussed.

## 4.1 Judd-Ofelt parameters calculation from emission spectrum

A method to obtain the radiative lifetimes of Tb-doped AlN thin films was implemented based on the JO theory. The advantage of this method consists in using the emission spectrum in order to calculate the JO parameters and the radiative lifetime. In this manner the proposed method solves the problem of screened absorption bands of the RE ion due to highly absorbing host materials.

***Description of the proposed method***

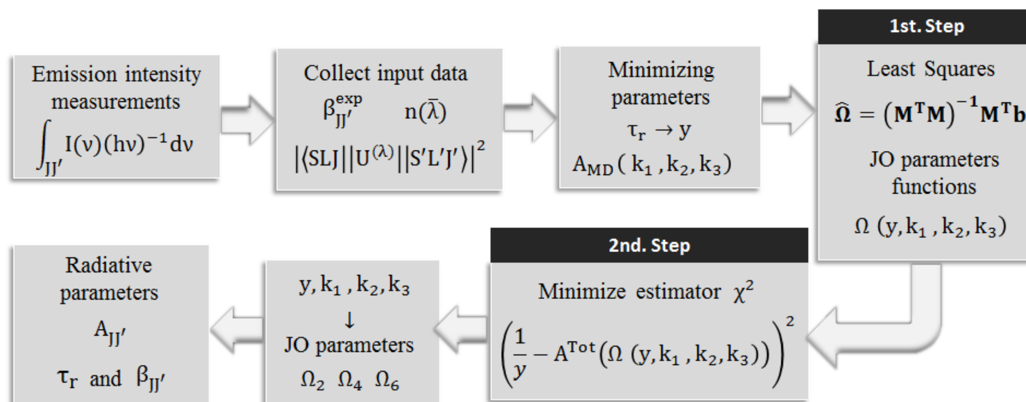


***Figure 4.1*** *Procedure of the proposed method for the Judd-Ofelt analysis using the emission spectrum.*

The procedure of the proposed JO analysis from emission spectrum is represented in a flow chart shown in Figure 4.1. The first step of this method consists of determining the



Tesis publicada con autorización del autor
No olvide citar esta tesis

PONTIFICIA UNIVERSIDAD CATÓLICA DEL PERÚ

experimental branching ratio from the emission spectrum using Eq. (2.23) and Eq.(2.24). The experimental branching ratios constitutes the input data, together with the refractive index and the values of the squared reduced-matrix elements given in Kaminskii [45].

The calculation of the JO parameters involves two step procedures. In the first step, the input data is replaced in Eq.(2.32)-Eq.(2.35), and the matrix of the least-square is developed to estimate the JO parameters. However, at this stage the JO parameters are expressions that depend on the unknown variables $y$ (for the radiative lifetime), $k_0$ $k_1$, $k_2$ and $k_3$ (for the MD squared matrix elements). The second step, consist of minimizing an estimator $\chi^2$ in order to solve the unknown variables $y, k_0, k_1, k_2$ and $k_3$. Once they are found, the JO parameters are calculated and with them it is possible to calculate the derived quantities: spontaneous emission probability, branching ratios and radiative lifetime.

***Test of the method***

The validity of the proposed method was tested by comparing the results obtained with the ones reported in literature data. The reported JO parameters of Tb doped bulk materials were determined using the absorption spectrum by applying a least-square fit between the theoretical and experimental dipole line strength, then the derived quantities were further calculated. The experimental branching ratio is a value usually reported in literature to stablish a comparison with the calculated ones. Since the experimental branching ratios reported in literature are related to the emission spectrum, they will be used to test the proposed method.

The mean wavelength, refractive index and experimental branching ratios reported in [46] and [89] and the calculated branching ratios reported in [48] were used as input data to test the proposed method. The JO parameters were obtained and with them the derived quantities were calculated. The results of the proposed method and the values reported in literature are listed in Table 4.1.

The JO parameters values in this work are not comparable to the values given in the references. In the latter, they are obtained directly by a fit of the dipole line strength expressions from absorption. In the present method, they are indirectly determined: the emission spectrum is an input data in the form of experimental branching ratios which are



Tesis publicada con autorización del autor
No olvide citar esta tesis

taken into account in the matrix of the least-square estimation of the JO parameters expressions, then by minimizing the estimator $\chi^2$ the JO parameters values are obtained. Thus, the proposed approach to obtain the JO parameters from emission spectra excited multiplets ($^5D_4 \rightarrow {}^7F_{3,4,5,6}$) is very different from the straightforward fit. However, as can be seen in Table 4.1 the method succeeds in recovering the branching ratios and the radiative lifetime.

The set of experimental branching ratios values for the $^7F_{0,1,2}$ peaks were assumed as zero due to the very low intensity of this emission peaks, as is suggested in [46]. On the other hand, literature did not report the error in the calculation of the JO parameters, spontaneous emission probability, branching ratios and radiative lifetime. The only reported error is the RMS of the fit between the experimental and calculated dipole line strength.

The spontaneous emission probabilities calculated by the proposed method present high relative errors when compared with the reported values. However, a plot of the different spontaneous emission probabilities reported and the ones calculated in this work show that the proposed method can recover the tendency (see Figure 4.2) of the values. At some transitions the spontaneous emission probability increments or decrements with respect to the reported values. It can be seen in Figure 4.2 these changes are related with an enhancement of the calculated branching ratios in the present work. This is also appreciated in the lower RMS deviation between the experimental and calculated branching ratios obtained in the present work (see Table 4.1). On the other hand, the calculated radiative lifetimes with the proposed method have a relative error less than 2% with the reported values.

These results are proofing that the proposed method works and can predicts the spontaneous emission probability, branching ratios and radiative lifetime parameters.



Tesis publicada con autorización del autor
No olvide citar esta tesis

***Table 4.1.*** *Comparison between the values of the JO parameters values. branching ratios $\beta_{JJ'}$, spontaneous emission probabilities $A_{JJ'}$ and radiation lifetimes $\tau$ obtained by the proposed method with three different spectra from literature* [48], [46], [89].

| Transition from $^5D_4$ | $\beta_{JJ'}^{exp}$ | $\Omega^{cal}$ $10^{-20}\ cm^2$ [this work] | $\Omega^{cal}$ $10^{-20}\ cm^2$ [ref] | $A_{JJ'}\ (s^{-1})$ [this work] | $A_{JJ'}\ (s^{-1})$ [ref] | Rel. error $\%\ \delta A_{JJ'}$ | $\beta_{JJ'}^{cal}$ [this work] | $\beta_{JJ'}^{cal}$ [ref] | $\tau_{rad}\ (ms)$ [this work] | $\tau_{rad}\ (ms)$ [ref] |
|---|---|---|---|---|---|---|---|---|---|---|
| *From $TbAlO_3$* [48] | | | | | | | | | | |
| $^7F_0$ | ~0 | $\Omega_2$= | 40.52 | 3.87± 0.01 | 2.46 | 57 | 0.01± 5×10$^{-4}$ | 0.0009 | | |
| $^7F_1$ | ~0 | 1.33± 0.005 | | 4.59± 0.02 | 11.55 | 60 | 0.02± 5×10$^{-4}$ | 0.04 | | |
| $^7F_2$ | ~0 | $\Omega_4$= | 8.74 | 6.32± 0.01 | 10-11 | 37 | 0.02± 4×10$^{-7}$ | 0.03 | | |
| $^7F_3$ | 0.33 | 0.78± 0.004 | | 95.42± 0.04 | 95.64 | 0.23 | 0.34± 2×10$^{-3}$ | 0.33 | 3.50 ± 0.004 | 3.5 |
| $^7F_4$ | 0.02 | $\Omega_6$= | 2.26 | 6.82± 0.05 | 6.43 | 6.06 | 0.02± 1×10$^{-3}$ | 0.02 | | |
| $^7F_5$ | 0.51 | 0.03± 0.004 RMS(*)= | (**) | 147.34± 0.10 | 147.77 | 0.29 | 0.52± 2×10$^{-3}$ | 0.51 | | |
| $^7F_6$ | 0.05 | 0.02 | | 14.59± 0.06 | 15.13 | 3.56 | 0.05± 2×10$^{-3}$ | 0.05 | | |
| *From lead telluroborate PTBTb20 glass* [46] | | | | | | | | | | |
| $^7F_0$ | ~0 | $\Omega_2$= | 11.98 | 1.09± 0.002 | 1.48 | 26 | 0.002± 5×10$^{-5}$ | ~0 | | |
| $^7F_1$ | ~0 | 0.01± 0.002 | | 1.31± 0.003 | 2.27 | 42 | 0.003± 7×10$^{-5}$ | 0.01 | | |
| $^7F_2$ | ~0 | $\Omega_4$= | 2.87 | 1.90± 0.01 | 12.47 | 84 | 0.005± 2×10$^{-5}$ | 0.03 | | |
| $^7F_3$ | 0.05 | 0.48± 0.001 | | 18.30± 0.007 | 29.59 | 38 | 0.04± 1×10$^{-4}$ | 0.08 | 2.70 ± 0.003 | 2.75 |
| $^7F_4$ | 0.11 | $\Omega_6$= | 10.51 | 45.54± 0.07 | 10.66 | 327 | 0.11± 5×10$^{-5}$ | 0.03 | | |
| $^7F_5$ | 0.49 | 17.7± 0.001 | | 202.51± 0.01 | 273.91 | 26 | 0.49± 2×10$^{-4}$ | 0.76 | | |
| $^7F_6$ | 0.34 | RMS= 0.004 | RMS =0.18 | 137.22± 0.01 | 32.20 | 326 | 0.33± 2×10$^{-4}$ | 0.09 | | |
| *From NBTb fluorophosphates glass* [89] | | | | | | | | | | |
| $^7F_0$ | ~0 | $\Omega_2$= | 2.75 | 6.22± 0.02 | 4.70 | 32 | 0.03± 5×10$^{-4}$ | - | | |
| $^7F_1$ | ~0 | 0.05± 0.002 | | 7.42± 0.03 | 7.30 | 1.64 | 0.03± 6×10$^{-4}$ | - | | |
| $^7F_2$ | ~0 | $\Omega_4$= | 3.21 | 2.17± 0.01 | 4.40 | 50 | 0.01± 2×10$^{-4}$ | - | | |
| $^7F_3$ | 0.15 | 2.14± 0.008 | | 18.05± 0.06 | 16.10 | 12 | 0.09± 1×10$^{-4}$ | 0.09 | 5.08 ± 0.01 | 5.1 |
| $^7F_4$ | 0.18 | $\Omega_6$= | 3.36 | 29.20± 0.06 | 15.70 | 85 | 0.15± 8×10$^{-5}$ | 0.12 | | |
| $^7F_5$ | 0.45 | 7.27± 0.01 | | 96.89± 0.14 | 127.30 | 23 | 0.49± 3×10$^{-3}$ | 0.62 | | |
| $^7F_6$ | 0.22 | RMS=0.04 | RMS= 0.09 | 36.55± 0.08 | 20.80 | 75 | 0.19± 1×10$^{-4}$ | 0.17 | | |

(*) Every RMS value was calculated according to Eq. (2.38) 0

(**) RMS value cannot be calculated since $\beta_{JJ'}^{exp}$ is not reported in [48]. The reported $\beta_{JJ'}^{cal}$ was used instead.



PONTIFICIA UNIVERSIDAD CATÓLICA DEL PERÚ

Tesis publicada con autorización del autor
No olvide citar esta tesis

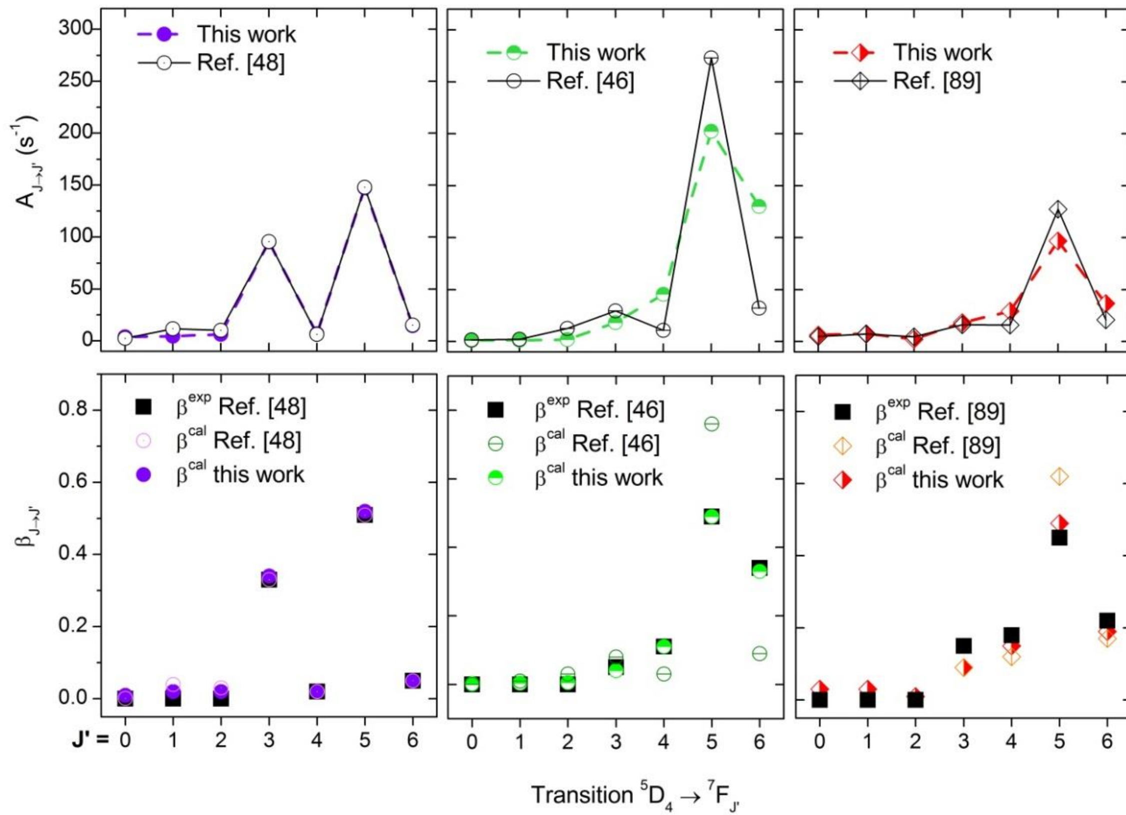


***Figure 4.2*** *Comparison between the spontaneous emission probabilities $A_{JJ}$ and the branching ratios $\boldsymbol{\beta}_{JJ}$ obtained by the proposed method and the reported values in literature.*

## 4.2 Luminescence analysis

This section presents the results obtained from CL experiments of annealed Tb doped AlN samples. Furthermore, calculation of the radiative lifetime using the proposed JO analysis from CL data obtained at room temperature is presented.

### 4.2.1 Emission spectra of AlN:Tb thin films

To analyze the radiative properties of Tb ions embedded in aluminum nitride thin films, cathodoluminescence excitation spectroscopy was applied for the samples in as deposited



Tesis publicada con autorización del autor
No olvide citar esta tesis

TESIS PUCP

state and annealed at temperatures between 500 °C and 1000 °C. Figure 4.3 below show the CL emitted light intensity obtained. The main four optical transitions ${}^5D_4 \rightarrow {}^7F_3$, ${}^5D_4 \rightarrow {}^7F_4$, ${}^5D_4 \rightarrow {}^7F_5$ and ${}^5D_4 \rightarrow {}^7F_6$ are well resolved and occurred around 622, 589, 546 and 490 nm respectively.

The samples annealed with RTP single-step process exhibits the strongest light emission intensity spectrum. The RTP multi-step process produced samples with lower emission intensity spectrum. The lowest intensity corresponds to the samples annealed with the QTF single-step process. This CL intensity variation with annealing treatment is shown in Figure 4.4 with the integrated light emission intensity of the strongest ${}^5D_4 \rightarrow {}^7F_5$ transition band.

The RTP single-step annealed samples present the maximum intensity at 750 °C, the RTP multi-step and the QTF single-step annealed samples present the maximum intensity at 900°C. Since the Tb ions are embedded and fixed in the AlN matrix, the excitation and enhancement of radiative de-excitation channels in the Tb ion depend on the effect of the microscopic structural parameters surrounding the ion. These structural parameters are influenced by the annealing temperature, and they are behind the observed enhancement of the Tb emission intensity with annealing temperature. Once the intensity starts to drop above 900°C occurs the enhancement of non-radiative de-excitation channels.

The effect of the structural changes on the radiative quantum efficiency can be estimated by applying the JO-analysis which determines the radiative lifetime. In the following sub-section the proposed method is applied to the produced samples to calculate and investigate the influence of the annealing temperatures on the JO parameters, spontaneous emission probabilities, branching ratios and radiative lifetime values.



Tesis publicada con autorización del autor
No olvide citar esta tesis

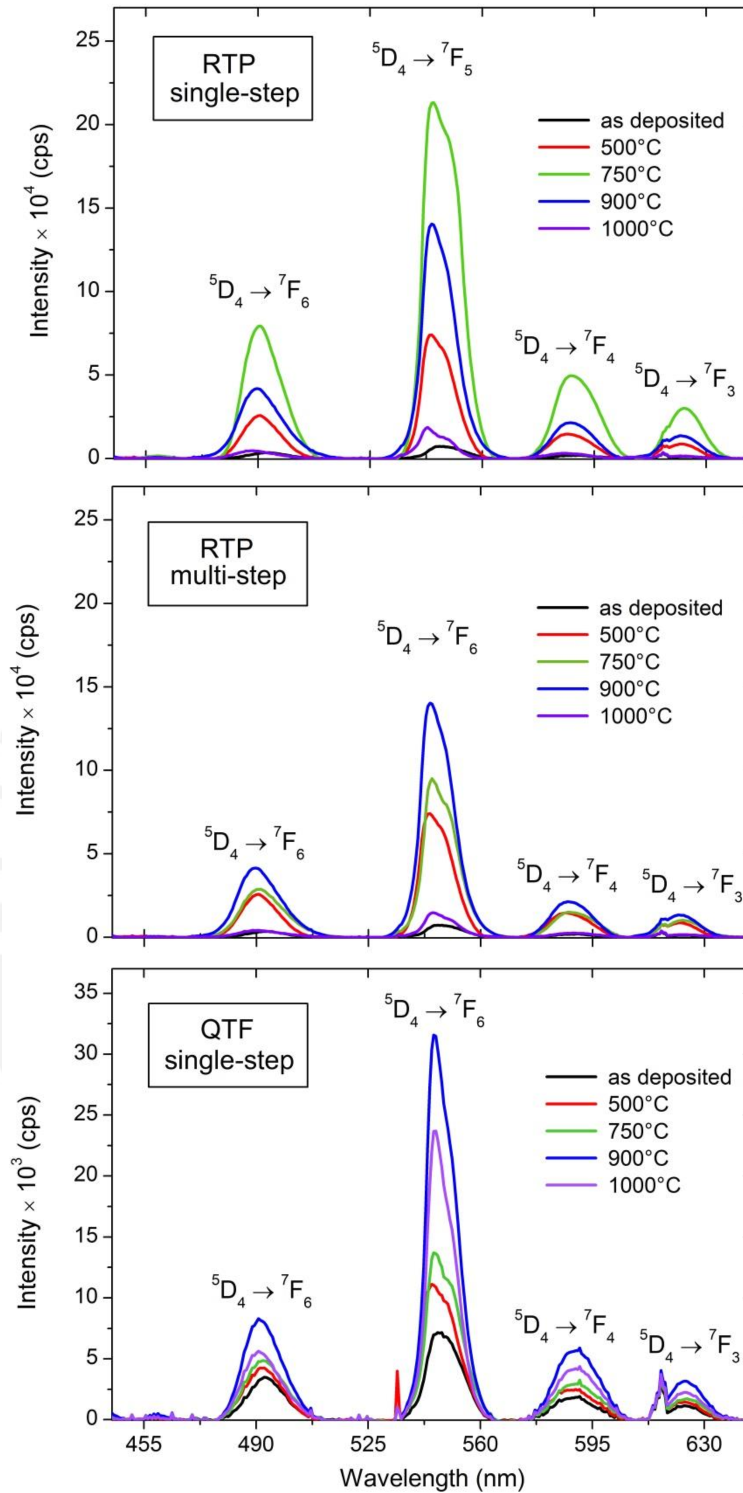


***Figure 4.3*** *Room temperature CL spectrum of AlN:Tb thin films with and without annealing treatments. Each spectrum is the average of six measured CL intensities. The inset indicates the annealing temperature.*



Tesis publicada con autorización del autor
No olvide citar esta tesis

TESIS PUCP

PONTIFICIA UNIVERSIDAD CATÓLICA DEL PERÚ

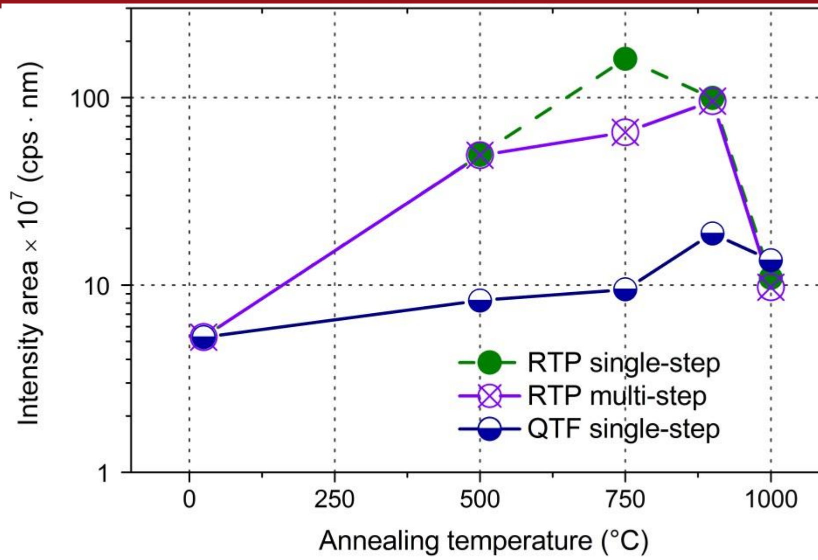


***Figure 4.4*** *Integrated CL intensity of the* $^5\boldsymbol{D_4} \rightarrow {}^7\boldsymbol{F_5}$ *transition of AlN:Tb samples at different annealing temperatures. Logarithmic scale was used for a better spread out of the values.*

### 4.2.2 Radiative lifetime of AlN:Tb thin films

From the measured CL emission spectra of the produced samples, the experimental branching ratios were obtained for the emission band transitions $^5D_4 \rightarrow {}^7F_{3,4,5,6}$ using Eq.(2.24). Since the intensity of the transitions $^5D_4 \rightarrow {}^7F_{0,1,2}$ are very small and not seen in the CL spectrum, their branching ratio values were assumed to be zero, as in reference [46]. The mean wavelength of the emission bands was calculated using Eq. (2.7). The index of refraction of the AlN host has been obtained by transmission measurements. It is expressed as a function of the wavelength through the Cauchy dispersion formula given by:

$$n(\lambda) = p + q/\lambda^2 \quad (4.1)$$

The Cauchy coefficients, $p$ = 1.70 and $q$ = 10989.31 nm$^2$, were found for the as deposited AlN host using the method proposed by Guerra [50] to determine the refractive index from transmittance measurements. After annealing treatments these parameters incremented up to $p$ =2.10 and $q$ = 17568.60 nm$^2$, leading to an overall higher refractive index. These coefficients have been applied to Eq. (4.1) to determine the indices of refraction for the mean wavelengths of the emission bands investigated.



Tesis publicada con autorización del autor
No olvide citar esta tesis

The squared reduced-matrix elements are independent of the host and can be found in Kaminskii [45], the values are given in Table 4.2. Using the experimental branching ratios, refractive indices and mean wavelengths, the proposed method was applied to the produced samples to calculate the JO parameters values, which are given in Table 4.3.

***Table 4.2*** *Values of reduced matrix elements for the emission transitions of Tb ions* [45].

| Transition (from $^5D_4$) | $\bar{\lambda}$ (nm) | $\lvert\langle U^{(2)}\rangle\rvert^2$ | $\lvert\langle U^{(4)}\rangle\rvert^2$ | $\lvert\langle U^{(6)}\rangle\rvert^2$ |
|---|---|---|---|---|
| $^7F_0$ | 680 | 0 | 0.0022 | 0 |
| $^7F_1$ | 671 | 0 | 0.0025 | 0 |
| $^7F_2$ | 649 | 0.0016 | 0.0004 | 0.00008 |
| $^7F_3$ | 621 | 0.0137 | 0.0010 | 0.0007 |
| $^7F_4$ | 588 | 0.0003 | 0.0019 | 0.0015 |
| $^7F_5$ | 543 | 0.0139 | 0.0010 | 0.0026 |
| $^7F_6$ | 488 | 0.0007 | 0.0013 | 0.0011 |

***Table 4.3.*** *Values for the three JO parameters for AlN:Tb thin films with and without annealing treatment.*

| | | $\Omega_{i=2,4,6}$ $(\times 10^{-20}\ cm^2)$ | | | $\Delta\Omega_{i=2,4,6}$ $(\times 10^{-22}\ cm^2)$ | | |
|---|---|---|---|---|---|---|---|
| | | $\Omega_2$ | $\Omega_4$ | $\Omega_6$ | $\Delta\Omega_2$ | $\Delta\Omega_4$ | $\Delta\Omega_6$ |
| as deposited | | 0.11 | 0.12 | 2.81 | 0.10 | 0.87 | 0.95 |
| RTP single-step | 500 °C | 0.06 | 0.12 | 0.01 | 0.06 | 0.48 | 0.53 |
| | 750 °C | 0.09 | 0.08 | 0.01 | 0.04 | 0.32 | 0.36 |
| | 900 °C | 0.09 | 0.04 | 0.01 | 0.03 | 0.25 | 0.28 |
| | 1000 °C | 0.01 | 0.04 | 0.01 | 0.02 | 0.22 | 0.25 |
| RTP multi-step | 750 °C | 0.08 | 0.05 | 0.01 | 0.03 | 0.30 | 0.33 |
| | 900 °C | 0.09 | 0.03 | 0.21 | 0.02 | 0.23 | 0.25 |
| | 1000 °C | 0.10 | 0.05 | 0.01 | 0.03 | 0.30 | 0.33 |
| QTF single-step | 500 °C | 0.12 | 0.05 | 0.20 | 0.04 | 0.31 | 0.35 |
| | 750 °C | 0.15 | 0.05 | 0.01 | 0.04 | 0.36 | 0.39 |
| | 900 °C | 0.14 | 0.08 | 0.01 | 0.05 | 0.42 | 0.46 |
| | 1000 °C | 0.13 | 0.06 | 0.01 | 0.04 | 0.36 | 0.40 |

The JO parameters are important for the investigation of the local structure and bonding in the vicinity of the RE ion. The change of the values of $\Omega_2$, $\Omega_4$ and $\Omega_6$ with different annealing temperature is consistent with the change in the intensity of the strongest emission $^5D_4 \rightarrow {}^7F_5$ and is shown in Figure 4.5. The $\Omega_2$ values larger than $\Omega_4$, are related with a change in symmetry and strong covalent bonding. In Figure 4.5 it is observed that for Tb ions, $\Omega_2$ and $\Omega_4$parameters are in the same range [0.01-0.15 $\times$ $10^{-20}$ $cm^2$] which suggest a lesser covalent environment for the Tb ions and an increase of the ionic nature of the chemical bond with the



Tesis publicada con autorización del autor
No olvide citar esta tesis

ligands. Compared with RTP single and multi-step annealing, the QTF process presents a relatively higher $\Omega_2$ with a decreasing intensity. On the other hand, as the annealing temperature increases the $\Omega_6$ parameter decreases drastically from the as deposited state to become the lowest parameter in the samples annealed. Since $\Omega_6$ is related to the rigidity of the host matrix, it indicates lower rigidity of the medium with increasing annealing temperature.

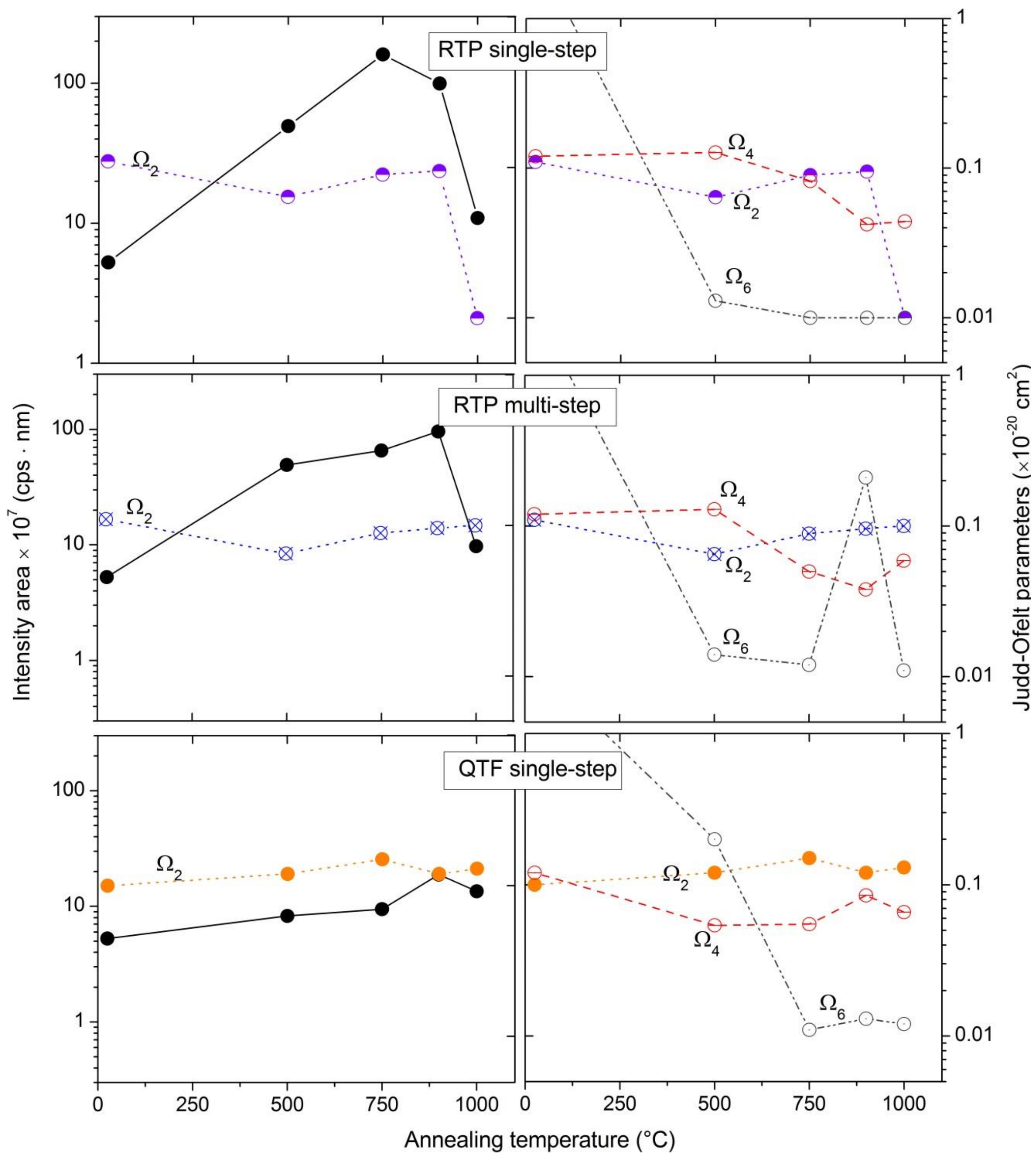


***Figure 4.5*** *Calculated* $\boldsymbol{\Omega_2}$, $\boldsymbol{\Omega_4}$ *and* $\boldsymbol{\Omega_6}$*and the intensity of the strongest transition* $^5\boldsymbol{D_4} \rightarrow {}^7\boldsymbol{F_5}$ *for AlN:Tb versus annealing temperature. Logarithmic scale was used for a better spread out of the values*



Tesis publicada con autorización del autor
No olvide citar esta tesis

However, as the annealing temperature increases there is no clear tendency with the JO parameters. See for example in Figure 4.5, the maximum intensity in the RTP single-step occurs when $\Omega_2 > \Omega_4 > \Omega_6 Figure\ 4.5$ , for RTP multi-step $\Omega_6 > \Omega_2 > \Omega_4 Figure\ 4.5$ and for QTF the tendency is $\Omega_2 > \Omega_4 > \Omega_6 Figure\ 4.5$ again. The variation of the JO parameters gives no more information of the structural changes at the maximum increment of intensity.

With the calculated JO parameters, the spontaneous emission probability and branching ratio values for the ${}^5D_4 \rightarrow {}^7F_{J'}$ ($J'$=0 – 6) transitions were obtained, and the radiative lifetime of the ${}^5D_4$ level is determined. The propagation of the errors in the derived quantities was evaluated by partial derivatives. Since the order of the errors in $\Omega_2, \Omega_4$ and $\Omega_6$ is of $10^{-22}$ $cm^2$, the small errors in the JO parameters give also small errors in the derived quantities.

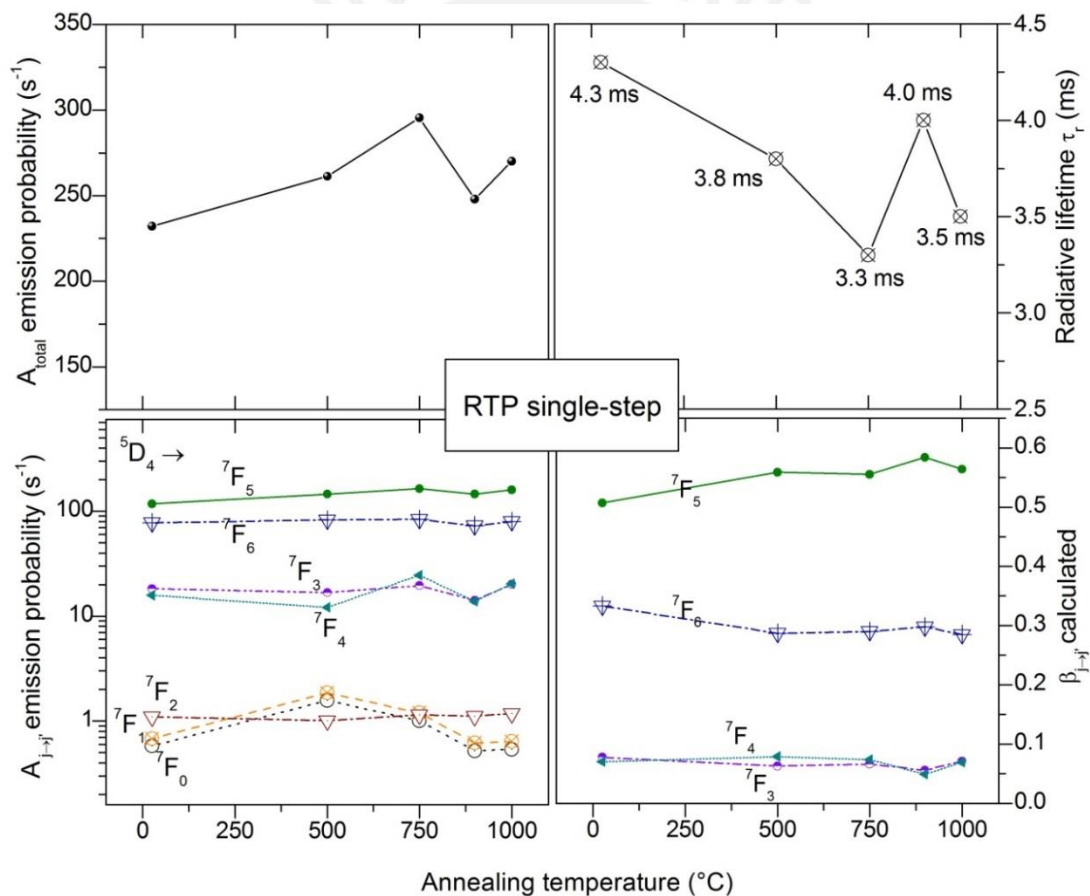


***Figure 4.6*** *Radiative properties versus annealing temperature. For a better spread out of the values the logarithmic scale is used for the $A_{J \rightarrow J'}$ emission probability.*

The results are shown in Table 4.4, Table 4.5 and Table 4.6. The RMS deviation has a maximum value of 0.06 and a minimum value of 0.02 for all the calculations. This is indicative of a good



Tesis publicada con autorización del autor
No olvide citar esta tesis

approach of the proposed method between the predicted and the experimental branching ratios, as compared to results obtained in other works [46], [49], [89], [100]. Along with the tabulated values, the tendencies of the radiative parameters versus annealing temperature are plotted in Figure 4.6, Figure 4.7, and Figure 4.8 with the objective of comparison.

***Table 4.4*** *Radiative properties of AlN:Tb thin film in as deposited state and after RTP single-step annealing.*

| Transition from $^5D_4$ | $\bar{\lambda}\,(nm)$ | $A_{JJ'}(s^{-1})$ | $A_{JJ'}^{ed}(s^{-1})$ | $A_{JJ'}^{md}(s^{-1})$ | $\tau_{rad}(ms)$ | $\beta_{JJ'}^{cal}$ | $\beta_{JJ'}^{exp}$ |
|---|---|---|---|---|---|---|---|
| As deposited | | | | | | | |
| $^7F_0$ | 680 | $0.58 \pm 0.03$ | 0.58 | 0 | $4.30 \pm 0.01$ | $0.002 \pm 1\times 10^{-4}$ | ~0 |
| $^7F_1$ | 671 | $0.68 \pm 0.04$ | 0.68 | 0 | | $0.002 \pm 2\times 10^{-4}$ | ~0 |
| $^7F_2$ | 649 | $1.10 \pm 0.01$ | 1.10 | 0 | | $0.004 \pm 1\times 10^{-4}$ | ~0 |
| $^7F_3$ | 622 | $18.26 \pm 0.08$ | 10.09 | 8.17 | | $0.07 \pm 2\times 10^{-4}$ | 0.07 |
| $^7F_4$ | 590 | $15.79 \pm 0.10$ | 14.63 | 1.16 | | $0.06 \pm 3\times 10^{-4}$ | 0.12 |
| $^7F_5$ | 546 | $117.80 \pm 0.19$ | 36.97 | 80.83 | | $0.50 \pm 5\times 10^{-4}$ | 0.50 |
| $^7F_6$ | 493 | $77.97 \pm 0.13$ | 19.20 | 58.77 | | $0.33 \pm 3\times 10^{-4}$ | 0.28 |
| | | | | | | | RMS = 0.04 |
| 500 °C | | | | | | | |
| $^7F_0$ | 680 | $1.57 \pm 0.06$ | 1.57 | 0 | $3.8 \pm 0.01$ | $0.006 \pm 2\times 10^{-4}$ | ~0 |
| $^7F_1$ | 671 | $1.86 \pm 0.07$ | 1.86 | 0 | | $0.007 \pm 2\times 10^{-4}$ | ~0 |
| $^7F_2$ | 649 | $1.01 \pm 0.02$ | 1.01 | 0 | | $0.003 \pm 1\times 10^{-4}$ | ~0 |
| $^7F_3$ | 621 | $16.74 \pm 0.12$ | 7.65 | 9.08 | | $0.06 \pm 3\times 10^{-4}$ | 0.06 |
| $^7F_4$ | 587 | $12.10 \pm 0.15$ | 2.52 | 9.58 | | $0.04 \pm 4\times 10^{-4}$ | 0.12 |
| $^7F_5$ | 546 | $145.67 \pm 0.31$ | 12.03 | 133.64 | | $0.55 \pm 8\times 10^{-4}$ | 0.56 |
| $^7F_6$ | 491 | $82.30 \pm 0.20$ | 3.63 | 78.66 | | $0.31 \pm 4\times 10^{-4}$ | 0.25 |
| | | | | | | | RMS = 0.06 |
| 750 °C | | | | | | | |
| $^7F_0$ | 680 | $1.01 \pm 0.03$ | 1.01 | 0 | $3.3 \pm 0.007$ | $0.003 \pm 1\times 10^{-4}$ | ~0 |
| $^7F_1$ | 671 | $1.20 \pm 0.05$ | 1.20 | 0 | | $0.004 \pm 2\times 10^{-4}$ | ~0 |
| $^7F_2$ | 649 | $1.15 \pm 0.01$ | 1.15 | 0 | | $0.003 \pm 4\times 10^{-4}$ | ~0 |
| $^7F_3$ | 623 | $19.55 \pm 0.08$ | 9.79 | 9.76 | | $0.06 \pm 1\times 10^{-4}$ | 0.06 |
| $^7F_4$ | 589 | $24.60 \pm 0.10$ | 1.76 | 22.83 | | $0.08 \pm 2\times 10^{-4}$ | 0.13 |
| $^7F_5$ | 547 | $164.32 \pm 0.20$ | 15.29 | 149.02 | | $0.56 \pm 5\times 10^{-4}$ | 0.58 |
| $^7F_6$ | 491 | $83.61 \pm 0.13$ | 2.90 | 80.71 | | $0.28 \pm 1\times 10^{-4}$ | 0.24 |
| | | | | | | | RMS = 0.04 |
| 900 °C | | | | | | | |
| $^7F_0$ | 680 | $0.52 \pm 0.03$ | 0.52 | 0 | $4.0 \pm 0.008$ | $0.002 \pm 1\times 10^{-4}$ | ~0 |
| $^7F_1$ | 671 | $0.62 \pm 0.04$ | 0.62 | 0 | | $0.002 \pm 1\times 10^{-4}$ | ~0 |
| $^7F_2$ | 649 | $1.11 \pm 0.01$ | 1.11 | 0 | | $0.004 \pm 3\times 10^{-4}$ | ~0 |
| $^7F_3$ | 622 | $14.09 \pm 0.07$ | 10.15 | 3.93 | | $0.05 \pm 2\times 10^{-4}$ | 0.05 |
| $^7F_4$ | 588 | $13.80 \pm 0.08$ | 1.11 | 12.68 | | $0.06 \pm 2\times 10^{-4}$ | 0.10 |
| $^7F_5$ | 546 | $145.10 \pm 0.16$ | 15.83 | 129.26 | | $0.58 \pm 5\times 10^{-4}$ | 0.58 |
| $^7F_6$ | 491 | $72.74 \pm 0.10$ | 2.15 | 70.59 | | $0.29 \pm 2\times 10^{-4}$ | 0.26 |
| | | | | | | | RMS = 0.03 |



Tesis publicada con autorización del autor
No olvide citar esta tesis

| | | | | | | | |
|---|---|---|---|---|---|---|---|
| | | | 1000 °C | | | | |
| $^7F_0$ | 680 | $0.54 \pm 0.02$ | 0.54 | 0 | $3.5 \pm 0.06$ | $0.001 \pm 1\times 10^{-4}$ | ~0 |
| $^7F_1$ | 671 | $0.64 \pm 0.03$ | 0.64 | 0 | | $0.002 \pm 1\times 10^{-4}$ | ~0 |
| $^7F_2$ | 649 | $1.18 \pm 0.01$ | 1.18 | 0 | | $0.004 \pm 3\times 10^{-4}$ | ~0 |
| $^7F_3$ | 619 | $20.07 \pm 0.06$ | 10.98 | 9.09 | | $0.07 \pm 1\times 10^{-4}$ | 0.07 |
| $^7F_4$ | 589 | $20.30 \pm 0.07$ | 1.15 | 19.15 | | $0.07 \pm 2\times 10^{-4}$ | 0.11 |
| $^7F_5$ | 545 | $159.41 \pm 0.14$ | 17.05 | 142.36 | | $0.56 \pm 4\times 10^{-4}$ | 0.56 |
| $^7F_6$ | 490 | $79.97 \pm 0.09$ | 2.27 | 77.70 | | $0.28 \pm 1\times 10^{-4}$ | 0.25 |
| | | | | | | | RMS = 0.02 |

The induced ED and MD transitions for the spontaneous emission probabilities were calculated for the observed emission intensity peaks. The strongest emission $^5D_4 \rightarrow {}^7F_5$ presents a remarkable spontaneous transition probability with the highest ED and MD contribution. Moreover, the $^5D_4 \rightarrow {}^7F_5$ and $^5D_4 \rightarrow {}^7F_6$ emissions are characterized by MD transitions higher than the induced ED transitions which was also found by a reference [49]. As can be seen from the values tabulated, the MD transitions contribute significantly to the total radiative transition $A_{JJ'}$. Among europium and erbium, terbium ions may also have strong MD transitions that may be applied in magnetic light-matter interactions at the nanoscale [101].

***Table 4.5*** *Radiative properties of AlN:Tb thin film after RTP multi-step annealing.*

| Transition | $\bar{\lambda}\ (nm)$ | $A_{JJ'}(s^{-1})$ | $A_{JJ'}^{ed}(s^{-1})$ | $A_{JJ'}^{md}(s^{-1})$ | $\tau_{rad}(ms)$ | $\beta_{JJ'}^{cal}$ | $\beta_{JJ'}^{exp}$ |
|---|---|---|---|---|---|---|---|
| | | | 750 °C | | | | |
| $^7F_0$ | 680 | $0.62 \pm 0.04$ | 0.62 | 0 | $4.2 \pm 0.01$ | $0.002 \pm 2\times 10^{-4}$ | ~0 |
| $^7F_1$ | 671 | $0.74 \pm 0.04$ | 0.74 | 0 | | $0.003 \pm 2\times 10^{-4}$ | ~0 |
| $^7F_2$ | 649 | $1.07 \pm 0.01$ | 1.07 | 0 | | $0.004 \pm 1\times 10^{-4}$ | ~0 |
| $^7F_3$ | 623 | $14.64 \pm 0.07$ | 9.53 | 5.11 | | $0.06 \pm 2\times 10^{-4}$ | 0.06 |
| $^7F_4$ | 589 | $12.61 \pm 0.09$ | 1.24 | 11.37 | | $0.05 \pm 3\times 10^{-4}$ | 0.10 |
| $^7F_5$ | 547 | $133.78 \pm 0.19$ | 14.88 | 118.90 | | $0.57 \pm 6\times 10^{-4}$ | 0.57 |
| $^7F_6$ | 492 | $69.26 \pm 0.12$ | 2.24 | 67.02 | | $0.29 \pm 2\times 10^{-4}$ | 0.25 |
| | | | | | | | RMS = 0.03 |
| | | | 900 °C | | | | |
| $^7F_0$ | 680 | $0.48 \pm 0.02$ | 0.48 | 0 | $3.5 \pm 0.02$ | $0.001 \pm 1\times 10^{-4}$ | ~0 |
| $^7F_1$ | 671 | $0.56 \pm 0.03$ | 0.56 | 0 | | $0.002 \pm 1\times 10^{-4}$ | ~0 |
| $^7F_2$ | 649 | $1.21 \pm 0.01$ | 1.21 | 0 | | $0.004 \pm 3\times 10^{-4}$ | ~0 |
| $^7F_3$ | 622 | $15.67 \pm 0.06$ | 11.28 | 4.39 | | $0.05 \pm 2\times 10^{-4}$ | 0.05 |
| $^7F_4$ | 588 | $16.60 \pm 0.07$ | 3.73 | 12.87 | | $0.06 \pm 2\times 10^{-4}$ | 0.09 |
| $^7F_5$ | 546 | $163.57 \pm 0.15$ | 21.83 | 141.74 | | $0.58 \pm 4\times 10^{-4}$ | 0.58 |
| $^7F_6$ | 491 | $80.04 \pm 0.09$ | 5.62 | 74.42 | | $0.28 \pm 1\times 10^{-4}$ | 0.25 |
| | | | | | | | RMS = 0.02 |



Tesis publicada con autorización del autor
No olvide citar esta tesis

| | | | | | | | |
|---|---|---|---|---|---|---|---|
| | | | 1000 °C | | | | |
| $^7F_0$ | 680 | $0.73 \pm 0.04$ | 0.73 | 0 | $3.6 \pm 0.07$ | $0.002 \pm 1\times 10^{-4}$ | ~0 |
| $^7F_1$ | 671 | $0.87 \pm 0.04$ | 0.87 | 0 | | $0.003 \pm 2\times 10^{-4}$ | ~0 |
| $^7F_2$ | 649 | $1.30 \pm 0.01$ | 1.30 | 0 | | $0.004 \pm 4\times 10^{-4}$ | ~0 |
| $^7F_3$ | 621 | $22.34 \pm 0.08$ | 11.69 | 10.65 | | $0.08 \pm 1\times 10^{-4}$ | 0.08 |
| $^7F_4$ | 589 | $17.69 \pm 0.09$ | 1.44 | 16.25 | | $0.06 \pm 2\times 10^{-4}$ | 0.11 |
| $^7F_5$ | 547 | $152.83 \pm 0.19$ | 18.10 | 134.73 | | $0.55 \pm 5\times 10^{-4}$ | 0.55 |
| $^7F_6$ | 492 | $79.97 \pm 0.12$ | 2.66 | 77.31 | | $0.29 \pm 2\times 10^{-4}$ | 0.25 |
| | | | | | | | RMS = 0.03 |

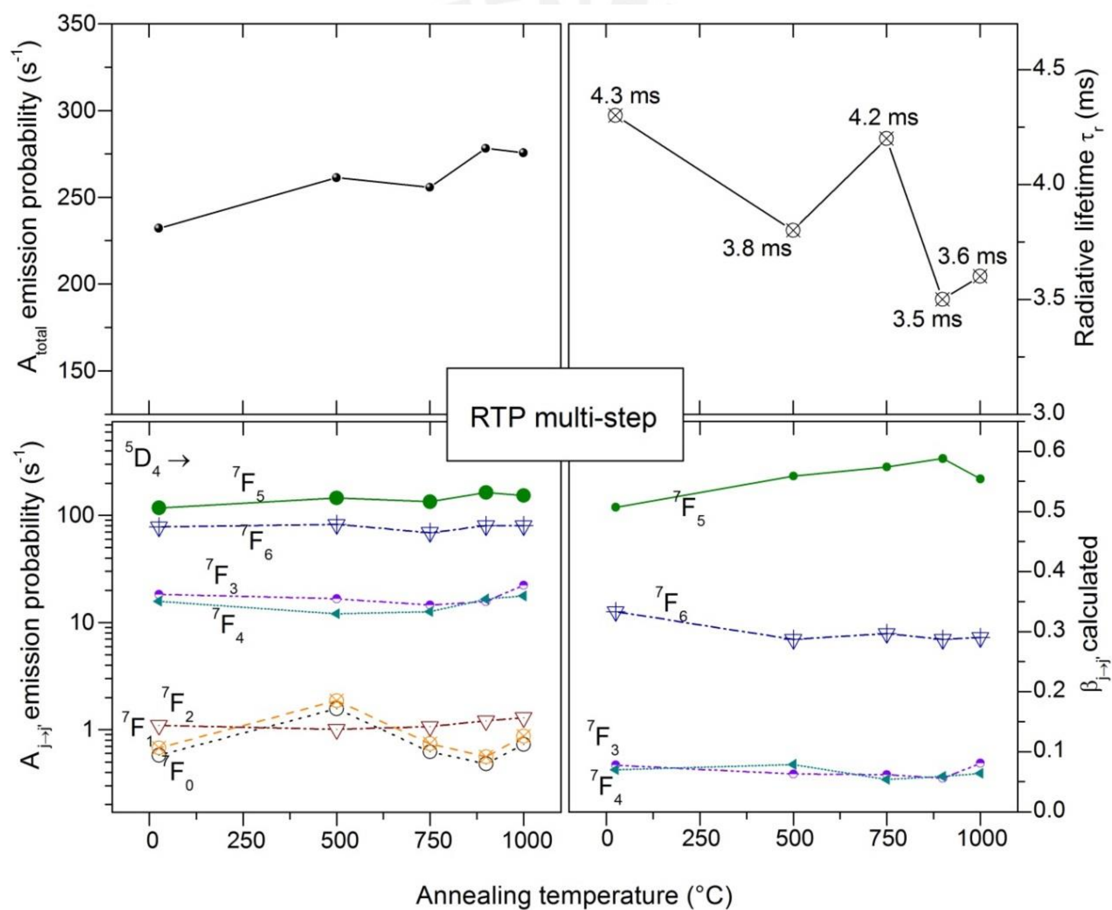


***Figure 4.7*** *Radiative properties versus annealing temperature. For a better spread out of the values the logarithmic scale is used for the* $A_{J\rightarrow J'}$ *emission probability.*



Tesis publicada con autorización del autor
No olvide citar esta tesis

***Table 4.6** Radiative properties of AlN:Tb thin film after QTF single-step annealing.*

| Transition | $\bar{\lambda}\,(nm)$ | $A_{JJ'}\,(s^{-1})$ | $A^{ed}_{JJ'}\,(s^{-1})$ | $A^{md}_{JJ'}\,(s^{-1})$ | $\tau_{rad}\,(ms)$ | $\beta^{cal}_{JJ'}$ | $\beta^{exp}_{JJ'}$ |
|---|---|---|---|---|---|---|---|
| | | | 500 °C | | | | |
| $^7F_0$ | 680 | $0.67 \pm 0.04$ | 0.67 | 0 | $3.6 \pm 0.08$ | $0.002 \pm 1\times 10^{-4}$ | ~0 |
| $^7F_1$ | 671 | $0.80 \pm 0.05$ | 0.80 | 0 | | $0.002 \pm 2\times 10^{-4}$ | ~0 |
| $^7F_2$ | 649 | $1.49 \pm 0.01$ | 1.49 | 0 | | $0.005 \pm 4\times 10^{-4}$ | ~0 |
| $^7F_3$ | 622 | $18.80 \pm 0.08$ | 13.62 | 5.17 | | $0.06 \pm 1\times 10^{-4}$ | 0.06 |
| $^7F_4$ | 589 | $15.75 \pm 0.10$ | 3.92 | 11.83 | | $0.06 \pm 2\times 10^{-4}$ | 0.11 |
| $^7F_5$ | 547 | $146.48 \pm 0.20$ | 25.16 | 121.32 | | $0.54 \pm 5\times 10^{-4}$ | 0.54 |
| $^7F_6$ | 493 | $87.18 \pm 0.13$ | 5.99 | 81.18 | | $0.32 \pm 3\times 10^{-4}$ | 0.28 |
| | | | | | | | RMS = 0.04 |
| | | | 750 °C | | | | |
| $^7F_0$ | 680 | $0.68 \pm 0.04$ | 0.68 | 0 | $3.7 \pm 0.09$ | $0.002 \pm 1\times 10^{-4}$ | ~0 |
| $^7F_1$ | 671 | $0.81 \pm 0.05$ | 0.81 | 0 | | $0.003 \pm 2\times 10^{-4}$ | ~0 |
| $^7F_2$ | 649 | $1.79 \pm 0.01$ | 1.79 | 0 | | $0.006 \pm 4\times 10^{-4}$ | ~0 |
| $^7F_3$ | 623 | $18.57 \pm 0.09$ | 16.44 | 2.12 | | $0.06 \pm 2\times 10^{-4}$ | 0.06 |
| $^7F_4$ | 590 | $14.45 \pm 0.11$ | 1.47 | 12.98 | | $0.05 \pm 3\times 10^{-4}$ | 0.11 |
| $^7F_5$ | 546 | $143.33 \pm 0.22$ | 25.35 | 117.97 | | $0.53 \pm 5\times 10^{-4}$ | 0.53 |
| $^7F_6$ | 493 | $88.34 \pm 0.15$ | 3.06 | 85.28 | | $0.33 \pm 3\times 10^{-4}$ | 0.28 |
| | | | | | | | RMS = 0.04 |
| | | | 900 °C | | | | |
| $^7F_0$ | 680 | $1.05 \pm 0.05$ | 1.05 | 0 | $3.8 \pm 0.01$ | $0.004 \pm 2\times 10^{-4}$ | ~0 |
| $^7F_1$ | 671 | $1.24 \pm 0.06$ | 1.24 | 0 | | $0.004 \pm 2\times 10^{-4}$ | ~0 |
| $^7F_2$ | 649 | $1.57 \pm 0.02$ | 1.57 | 0 | | $0.006 \pm 5\times 10^{-4}$ | ~0 |
| $^7F_3$ | 623 | $17.16 \pm 0.11$ | 13.82 | 3.34 | | $0.06 \pm 2\times 10^{-4}$ | 0..06 |
| $^7F_4$ | 590 | $15.50 \pm 0.13$ | 1.95 | 13.55 | | $0.06 \pm 3\times 10^{-4}$ | 0.13 |
| $^7F_5$ | 547 | $148.99 \pm 0.26$ | 21.55 | 127.44 | | $0.57 \pm 8\times 10^{-4}$ | 0.57 |
| $^7F_6$ | 492 | $75.62 \pm 0.17$ | 3.44 | 72.18 | | $0.28 \pm 2\times 10^{-4}$ | 0.23 |
| | | | | | | | RMS = 0.05 |
| | | | 1000 °C | | | | |
| $^7F_0$ | 680 | $0.82 \pm 0.05$ | 0.82 | 0 | $3.8 \pm 0.02$ | $0.003 \pm 2\times 10^{-4}$ | ~0 |
| $^7F_1$ | 671 | $0.97 \pm 0.05$ | 0.97 | 0 | | $0.003 \pm 2\times 10^{-4}$ | ~0 |
| $^7F_2$ | 649 | $1.54 \pm 0.02$ | 1.54 | 0 | | $0.005 \pm 4\times 10^{-4}$ | ~0 |
| $^7F_3$ | 623 | $17.27 \pm 0.09$ | 13.83 | 3.43 | | $0.06 \pm 2\times 10^{-4}$ | 0.06 |
| $^7F_4$ | 590 | $14.64 \pm 0.11$ | 1.62 | 13.02 | | $0.06 \pm 3\times 10^{-4}$ | 0.11 |
| $^7F_5$ | 545 | $147.72 \pm 0.23$ | 21.54 | 128.18 | | $0.57 \pm 7\times 10^{-4}$ | 0.57 |
| $^7F_6$ | 493 | $75.66 \pm 0.15$ | 3.05 | 72.61 | | $0.29 \pm 2\times 10^{-4}$ | 0.24 |
| | | | | | | | RMS = 0.04 |



Tesis publicada con autorización del autor
No olvide citar esta tesis

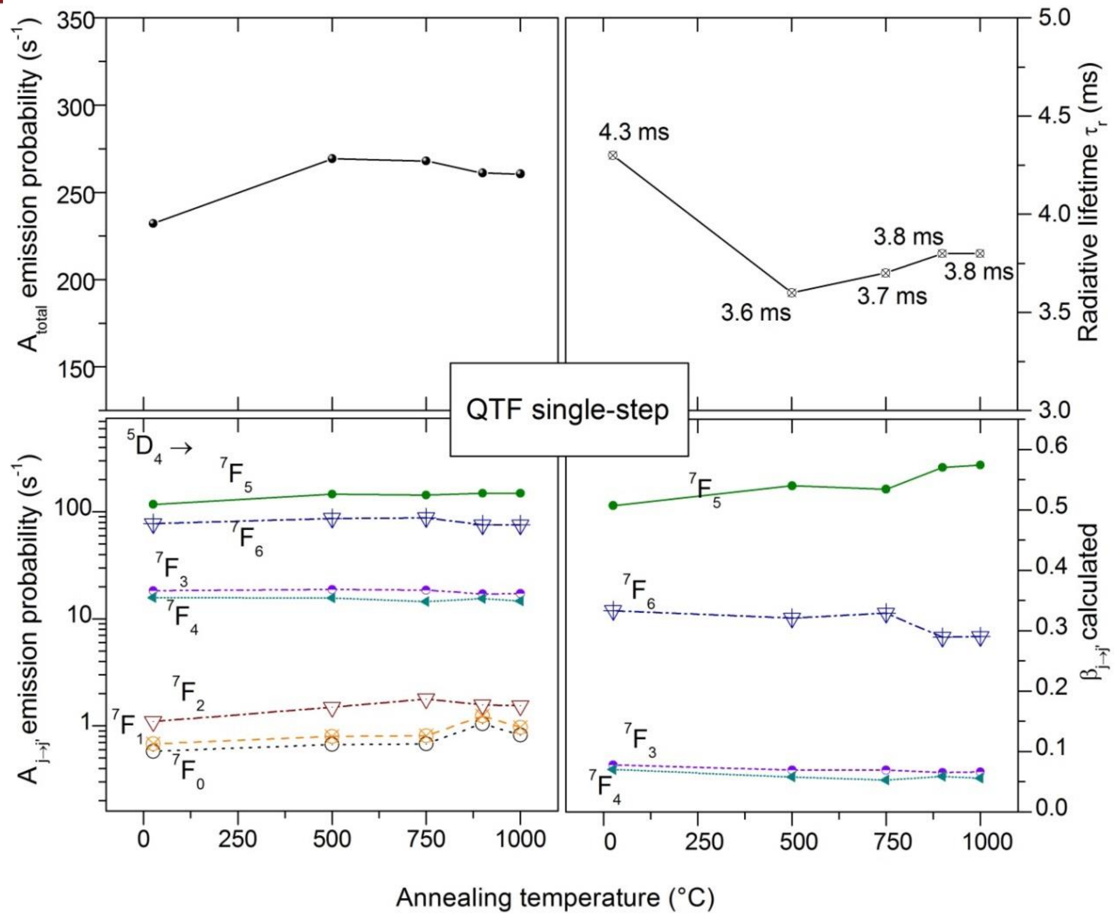


***Figure 4.8*** *Radiative properties versus annealing temperature. For a better spread out of the values the logarithmic scale is used for the $A_{J\to J'}$ emission probability.*

For the RTP single-step films, the total spontaneous emission probability present a maximum increment at 750°C in accordance with the highest intensity of the CL spectra measured (see Figure 4.6, Figure 4.7, and Figure 4.8). The same situation occurs for the RTP multi-step films at 900°C. However, for the QTF single-step samples the maximum total spontaneous emission probability does not correspond to the highest CL intensity spectra. Even though some values drops, the overall tendency is an increase of the spontaneous emission probability with annealing temperature. This is in agreement with the activation of the Tb ions with annealing temperature. Also the highest spontaneous emission probability and branching ratio calculated is in accordance with the strongest transition$^5D_4 \to {}^7F_5$.

The radiative life time is by definition the inverse of the total spontaneous emission probability, and represents the time required for an electron in an excited state to decay by emitting a photon. Since the spontaneous emission probability increments with the amount of emitting Tb ions, longer radiative lifetimes are associated with low probable transitions and



Tesis publicada con autorización del autor
No olvide citar esta tesis

with feeble emitted light intensities. Furthermore, a long radiative lifetime may imply reduce internal quantum efficiency for the material [102]–[104].

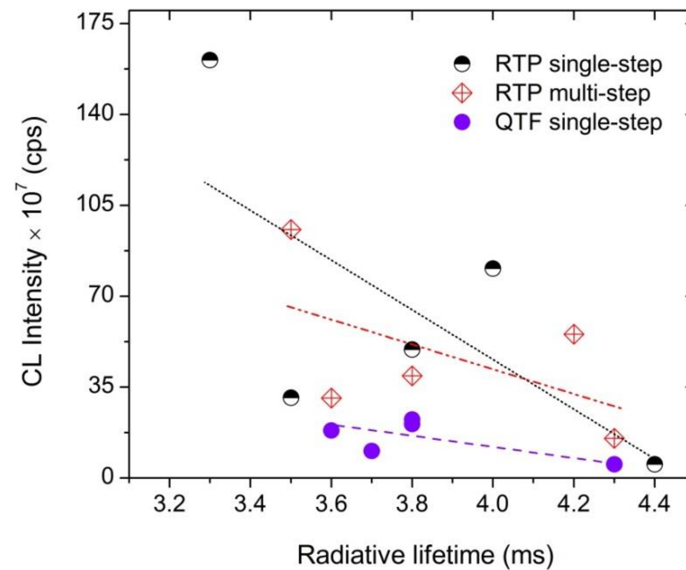


***Figure 4.9*** *CL intensities versus calculated radiative lifetime for AlN:Tb annealed samples.*

Figure 4.9 shows an increase in the CL intensity for shorter radiative lifetime values. At low radiative lifetime, the electrons decay faster from the excited to the lower energy state emitting photons and thus, enhancing the light intensity. Since the thermal quenching produces a decrease in the emitted intensity, it influences an increase of the radiative lifetime. This can be appreciated in the RTP single-step annealing from 750 to 900°C where the highest emission drops and the radiative lifetime value changes from 3.3 ms to 4.0 ms.

## 4.3 Structural analysis

The annealing effect on the structure and composition of the AlN:Tb films are investigated by means of X-ray diffraction, RHEED, SEM and EDX analysis. The results are presented and discussed in this section.



Tesis publicada con autorización del autor
No olvide citar esta tesis

TESIS PUCP

### 4.3.1 X-ray diffraction

The X-ray diffraction analysis was performed in grazing incidence with a rotation angle for the sample that allows avoiding the diffraction of the substrate silicon (100). By doing this, it is possible to increment the counts per second coming from the film, while minimizing the counts coming from the substrate.

The XRD patterns in Figure 4.10 show a phase of AlN wurtzite structure for the as deposited film and the films annealed up to 750°C. The hexagonal wurtzite structure of AlN corresponds to the Power Diffraction File (PDF) 25-3311, where the strongest peak corresponds to the $(10\bar{1}0)$ orientation at $2\theta$ angle of 33.2°. The other peaks with orientations $(10\bar{1}1)$, $(10\bar{1}2)$, $(11\bar{2}0)$, $(10\bar{1}3)$ and $(11\bar{2}2)$ are second peaks with less intensity. The annealed films at 900°C and 1000°C using RTP and QTF process, on the other hand, show XRD patterns consisting of new peaks due to the rise of second crystalline phases.

For the RTP single-step and multi-step annealing at 900°C and 1000°C, the X-ray analysis reveal the growth of second phases of aluminum oxynitride $Al_5O_6N$ with cubic structure corresponding to the PDF 48-0686, and of aluminum oxide $Al_2O_3$ with cubic structure corresponding to the PDF 74-2206. The strongest $Al_5O_6N$ peak has the orientation (311) at 37.4°, followed by a second peak with orientation (511) at 60.2°. Besides, the $Al_2O_3$ phase presents a strongest peak with orientation (400) at 45.87° and a second peak with orientation (440) at 66.8°. Only the AlN peak continues being the strongest peak observed at around 33.2°. These results suggest that the films after annealing still retains a highly preferred orientation in the $(10\bar{1}0)$ crystal plane of hexagonal AlN.

For the QTF single-step annealing at 900°C and 1000°C, the XRD pattern in **¡Error! No se encuentra el origen de la referencia.** shows a complete change of phase from the wurtzite AlN to the hexagonal $Al_2O_3$ structure reported on the PDF 13-0373. The crystal planes $(21\bar{3}4)$, $(10\bar{1}4)$ and $(20\bar{2}0)$ correspond to the peak positions 67.03°, 46.2° and 37.2° respectively. This indicates that the annealing treatment at high temperatures gets oxygen continuously diffusing into the thin film due to the gas flux during the annealing. This effect is weighed more for the QTF process since the flux of the nitrogen gas mix with the oxygen present in the quartz furnace, which is not isolated from the environment.



Tesis publicada con autorización del autor
No olvide citar esta tesis

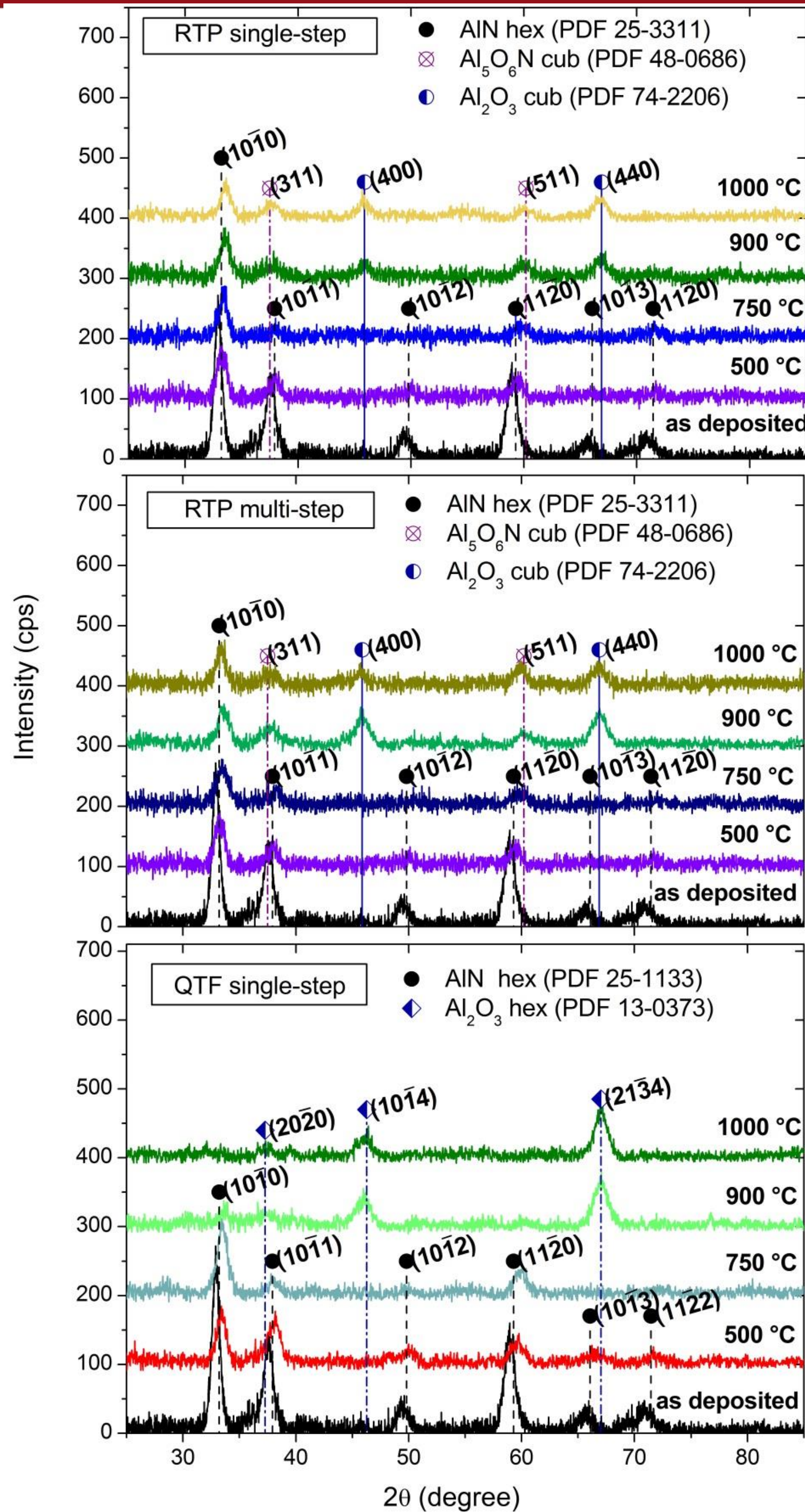


***Figure 4.10*** *XRD pattern of AlN:Tb thin film deposited by RF magnetron sputtering and annealed at different temperatures. The patterns are plotted together with a vertical shift of 100 cps for better identification of the peaks.*

From the full width half maximum (FWHM) of the XRD peaks, the average crystallite size can be roughly estimated by the Scherrer equation (4.2). It is important to remark here, the



Tesis publicada con autorización del autor
No olvide citar esta tesis

crystallite size is not exactly the grain size, and usually the grain size is much larger than the crystallite size [105], [106]. Thus, the crystallite size is the length of the coherently diffracting domains.

$$D = \frac{0.9\,\lambda}{\mathrm{FWHM}\ \mathrm{Cos}\theta} \tag{4.2}$$

Where, $\lambda$ is the X-ray wavelength and $\theta$ is half of the diffraction angle in radians.

The average crystallite size is plotted in Figure 4.11 as a function of the annealing temperature. The broadening of the X-ray strongest peaks: the orientation $(10\bar{1}0)$ for the AlN wurtzite structure and the orientation $(21\bar{3}4)$ for the $Al_2O_3$ hexagonal structure were used in the calculations.

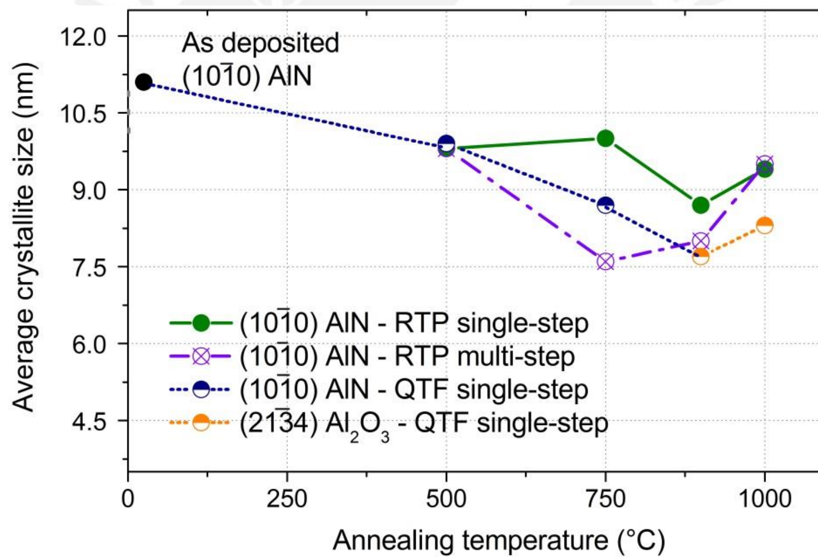


***Figure 4.11*** *Average crystalline size calculated using the Scherrer formula for $(10\bar{1}0)$ and $(21\bar{3}4)$ strongest orientation peaks in AlN:Tb thin films.*

Figure 4.12 plots the FWHM and the position of the peaks $2\theta$ versus annealing temperature for the $(10\bar{1}0)$ orientation in AlN wurtzite structure using RTP single-step process. The reduction of the crystallite size can be an effect of broader FWHM values and the shift of the $2\theta$ positions toward higher angles with increasing annealing temperature (see Figure 4.12). This suggests the presence of induced strain in the films. As can be seen in the XRD profile shown in Figure 4.13, the as deposited film presents a compressive strain. After the annealing treatment at 500°C, the compressive strain relaxes and the measured peak shifts to the



Tesis publicada con autorización del autor
No olvide citar esta tesis

theoretical positions of 32.21° without residual stresses. At higher annealing temperatures the measured peak shifts from the theoretical position to higher scattering angles, revealing a tension strain in the films.

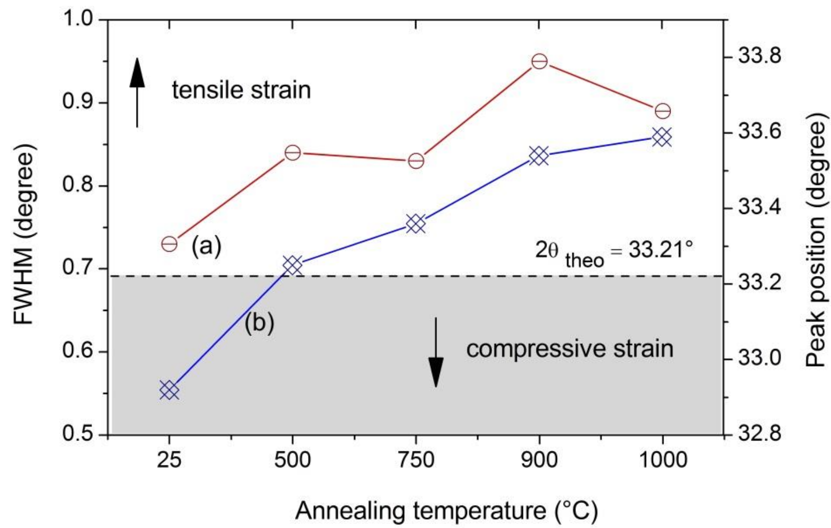


***Figure 4.12*** *Evolution of (a) the FHWM and (b) the peak position $2\theta$ of AlN wurtzite (10$\bar{1}$0) peak orientation with annealing temperature using RTP single-step.*

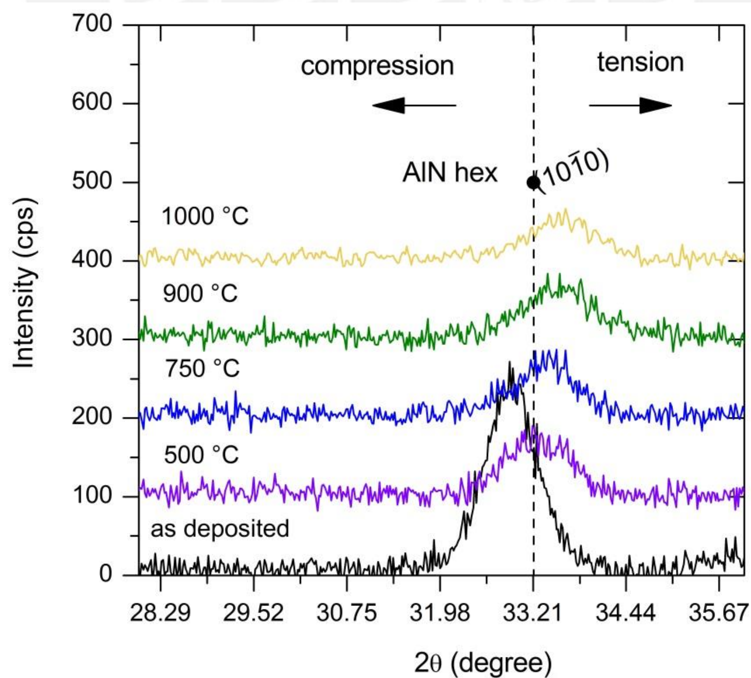


***Figure 4.13*** *Shift of the main peaks in the XRD profile of produced AlN:Tb thin films.*



Tesis publicada con autorización del autor
No olvide citar esta tesis

PONTIFICIA UNIVERSIDAD CATÓLICA DEL PERÚ

### 4.3.2 RHEED surface analysis

In order to examine qualitatively crystallinity of the AlN:Tb thin films, RHEED observations was performed. As the films were rotated around its normal axis, the RHEED patterns show the electron beam interactions with two set of crystal planes corresponding to the hexagonal wurtzite structure. One set of planes contains the $(10\bar{1}0)$ plane and equivalents, whereas the second set of planes contains the $(11\bar{2}0)$ plane and equivalents, as illustrated in Figure 4.14. The observed sets of crystal planes indicates the wurtzite AlN:Tb thin films are oriented with the c-axis normal to the film surface [107].

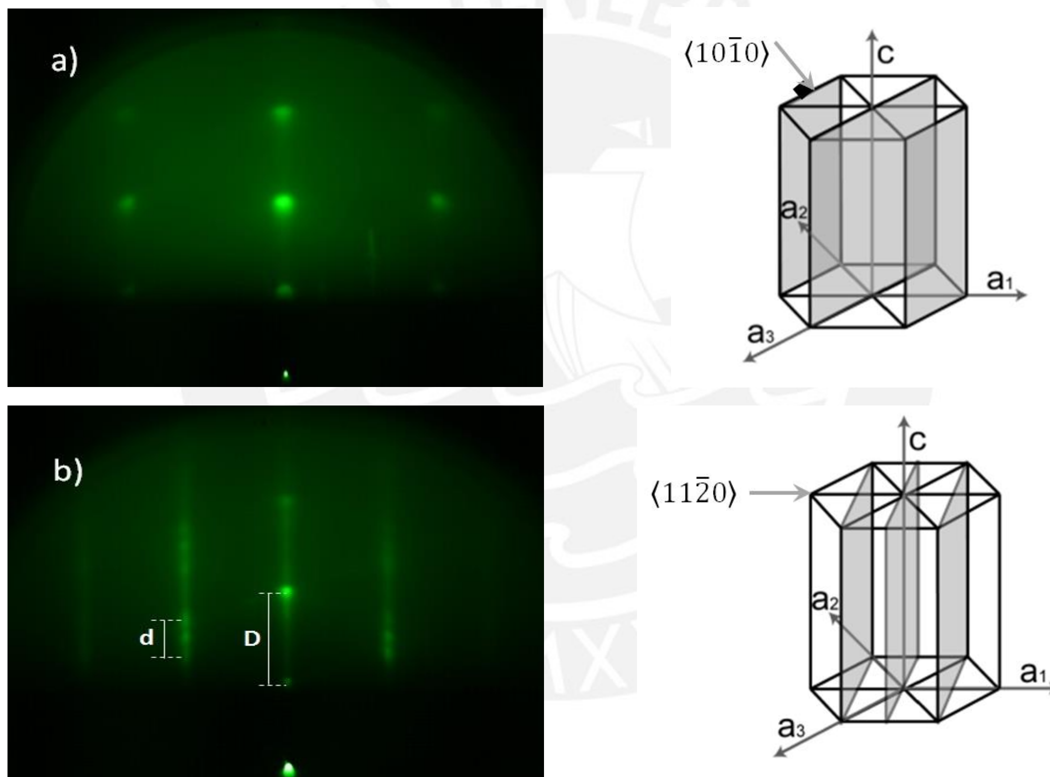


***Figure 4.14*** *RHEED pattern of AlN:Tb sample RTP annealed at 500°C arising from the (a)* $\{10\bar{1}0\}$ *and (b)* $\{11\bar{2}0\}$ *planes. The two main diffraction spots distance (D) is three times the slight diffraction spots distance (d). The hexagonal unit cell of the selected planes is shown (image from* [107]*).*

The measured distance D, between two main diffraction spots, is three times the measured distance d, between slight diffraction spots, sketched in the RHEED pattern arising from the $(11\bar{2}0)$ planes (see Figure 4.14 (b)). This corresponds to a superposition of two reciprocal lattices, one from a 2H hexagonal structure and other from a 3C cubic structure (see Figure



Tesis publicada con autorización del autor
No olvide citar esta tesis

4.15). The most stable structure of AlN is the 2H-AlN polytype [108]. Besides, a natural passivation layer of $Al_2O_3$ can be formed on the surface of aluminum as a result of oxidation [109]. Due to the presence of oxygen detected by EDX analysis, the surface of AlN specimens could be thinly covered, with a thickness typically lower than 10 nm [110], with $Al_2O_3$ layer. Thus, the RHEED pattern shows the occurrence of a 2H-AlN wurtzite structure and a 3C-$Al_2O_3$ cubic structure at the surface of samples. The simplest stacking of AlN layers follows the sequence described by AB for the hexagonal 2H structure. On the other hand, the $Al_2O_3$ can be visualized as a series of oxygen planes with an ABC stacking sequence with a different coordination of the aluminum atoms which gives rise to its cubic symmetry [111].

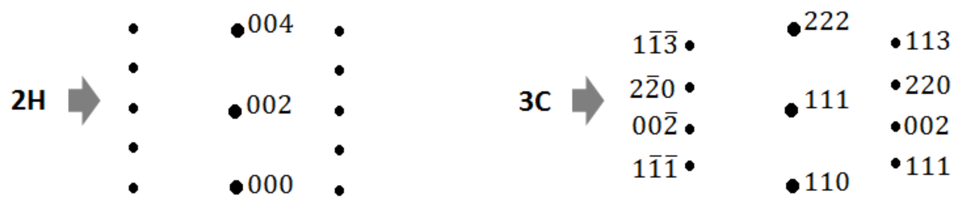


***Figure 4.15*** *Reciprocal lattices for a hexagonal close packed structure and a simple cubic structure.*

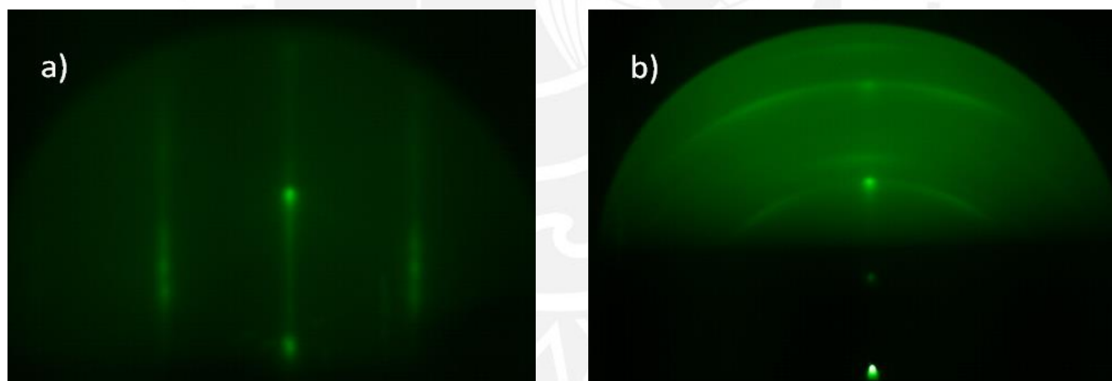


***Figure 4.16*** *RHEED pattern of AlN:Tb sample (a) RTP multi-step and (b) RTP single-step annealed at 900°C.*

The crystal quality can also be evaluated by RHEED analysis. For all the samples annealed treated above 750°C, the RHEED data collected shows severe diffused lines with spots (see Figure 4.16 (a)) and rings centered on the specular spot (see Figure 4.16 (b)). The diffused lines with spots indicate possible presence of plane defects such as stacking faults. Thus, the crystalline quality of the AlN:Tb films is reduced with annealing temperature, due to the presence of few planes not in the right position or existence of dislocation lines. This result coincides with the XRD measurements, which has revealed the presence of induced tensile



Tesis publicada con autorización del autor
No olvide citar esta tesis

PONTIFICIA UNIVERSIDAD CATÓLICA DEL PERÚ

strains and phase transition at higher post- deposition annealing. On the other hand, the crystallization by thermal annealing occurs due to the presence of defects, which works as nucleation centers leading to polycrystalline structures. The sharp rings observed in Figure 4.16 (b) suggest polycrystallization by thermal annealing of AlN:Tb.

### 4.3.3 EDX composition ratio

The elemental composition of the films was determined by EDX analysis as described in section 3.2. Detailed results are presented in Table 4.7 and Table 4.8. The N:Al and the O:N ratios were calculated to show the oxidation behavior of samples after annealing at 500°C, 750°C, 900°C and 1000°C using nitrogen atmosphere in both RTP and QTF processes.

***Table 4.7*** *EDX measurement results of AlN:Tb thin films with and without RTP annealing treatment.*

| Element | Concentration in at. % | | | | | | | |
|---|---|---|---|---|---|---|---|---|
| | as deposited | Single-step | | | | Multi-step | | |
| | | 500 °C | 750 °C | 900 °C | 1000°C | 750 °C | 900 °C | 1000°C |
| C | 5.8 | 6.6 | 7.0 | 5.6 | 5.2 | 5.7 | 5.8 | 4.6 |
| N | 26.2 | 20.4 | 17.2 | 15.8 | 13.1 | 14.7 | 16.0 | 11.0 |
| O | 30.1 | 34.1 | 34.3 | 34.6 | 37.7 | 38.0 | 34.4 | 41.4 |
| Tb | 0.2 | 0.6 | 0.8 | 0.5 | 0.3 | 0.4 | 0.8 | 0.6 |
| Al | 37.5 | 38.3 | 40.7 | 43.5 | 43.7 | 41.2 | 43.0 | 42.4 |
| Ratio | | | | | | | | |
| N:Al | 0.7 | 0.5 | 0.4 | 0.4 | 0.3 | 0.3 | 0.3 | 0.2 |
| O:N | 1.1 | 1.7 | 1.9 | 2.2 | 2.9 | 2.6 | 2.2 | 3.7 |

***Table 4.8*** *EDX measurement results of AlN:Tb thin films with and without QTF annealing treatment.*

| Element | Concentration in at. % | | | | |
|---|---|---|---|---|---|
| | as deposited | Single-step | | | |
| | | 500 °C | 750 °C | 900 °C | 1000 °C |
| C | 5.8 | 7.6 | 6.5 | 4.8 | 5.5 |
| N | 26.2 | 19.4 | 14.6 | 7.9 | 4.2 |
| O | 30.1 | 32.8 | 38.2 | 45.2 | 50.4 |
| Tb | 0.2 | 0.2 | 0.2 | 0.3 | 0.6 |
| Al | 37.5 | 40.0 | 40.5 | 41.8 | 39.3 |
| Ratio | | | | | |
| N:Al | 0.7 | 0.5 | 0.4 | 0.2 | 0.1 |
| O:N | 1.1 | 1.7 | 2.6 | 5.7 | 12.2 |



Tesis publicada con autorización del autor
No olvide citar esta tesis

The EDX measurement for the as deposited sample shows the aluminum content is higher than that of nitrogen. However the concentration of oxygen is about 30% and higher than that of nitrogen. Since the oxygen contamination at the surface layer is limited to 5-10 nm thick when the film is exposed to the atmosphere [112], the observed oxygen concentration cannot be limited to the surface. This suggests a competition between the nitrogen and the oxygen to react with aluminum during the deposition of the film. The amount of oxygen contamination depends on the sputtering system and the deposition parameters. Since none of the targets or gas flux contains oxygen, it should have come from the residual oxygen in the chamber or moisture leakage. From the high oxygen content in the as deposited state combined with the XRD analysis above is possible to infer that the produced films consist of both amorphous $Al_2O_3$ or $Al_5O_6N$ and crystalline AlN phases.

After annealing, the atomic percentage of aluminum and oxygen in the sample increases with annealing temperature. While the atomic percentage of nitrogen and carbon decreases. The increment of the oxygen reveals that at higher annealing temperatures the aluminum prefers to react with the oxygen impurities in the nitrogen gas flux during the annealing process. As can be seen in Table 4.8, the oxygen increment is higher in the QTF annealing due to the system setup which allows more air content gets trapped in the furnace. The oxygen content increases and diffuses inside the structure; it can react with aluminum to form second phases of crystalline $Al_2O_3$ and $Al_5O_6N$ already identified by the XRD analysis. This phase transformation would induce the nitrogen desorption.

It can be seen in Table 4.7 and Table 4.8 the N:Al ratio decreases with increasing annealing temperature, while the O:N ratio increases with increasing annealing temperature. This tendency is observed for the RTP and QTF process. The overall concentration in the sample varies as atoms are redistributed. Thus, the increase or decrease of the aluminum and terbium atomic percentage does not indicate a real variation of the amount of Tb ions or aluminum atoms in the samples.



Tesis publicada con autorización del autor
No olvide citar esta tesis

PONTIFICIA UNIVERSIDAD CATÓLICA DEL PERÚ

### 4.3.4 SEM micrographs

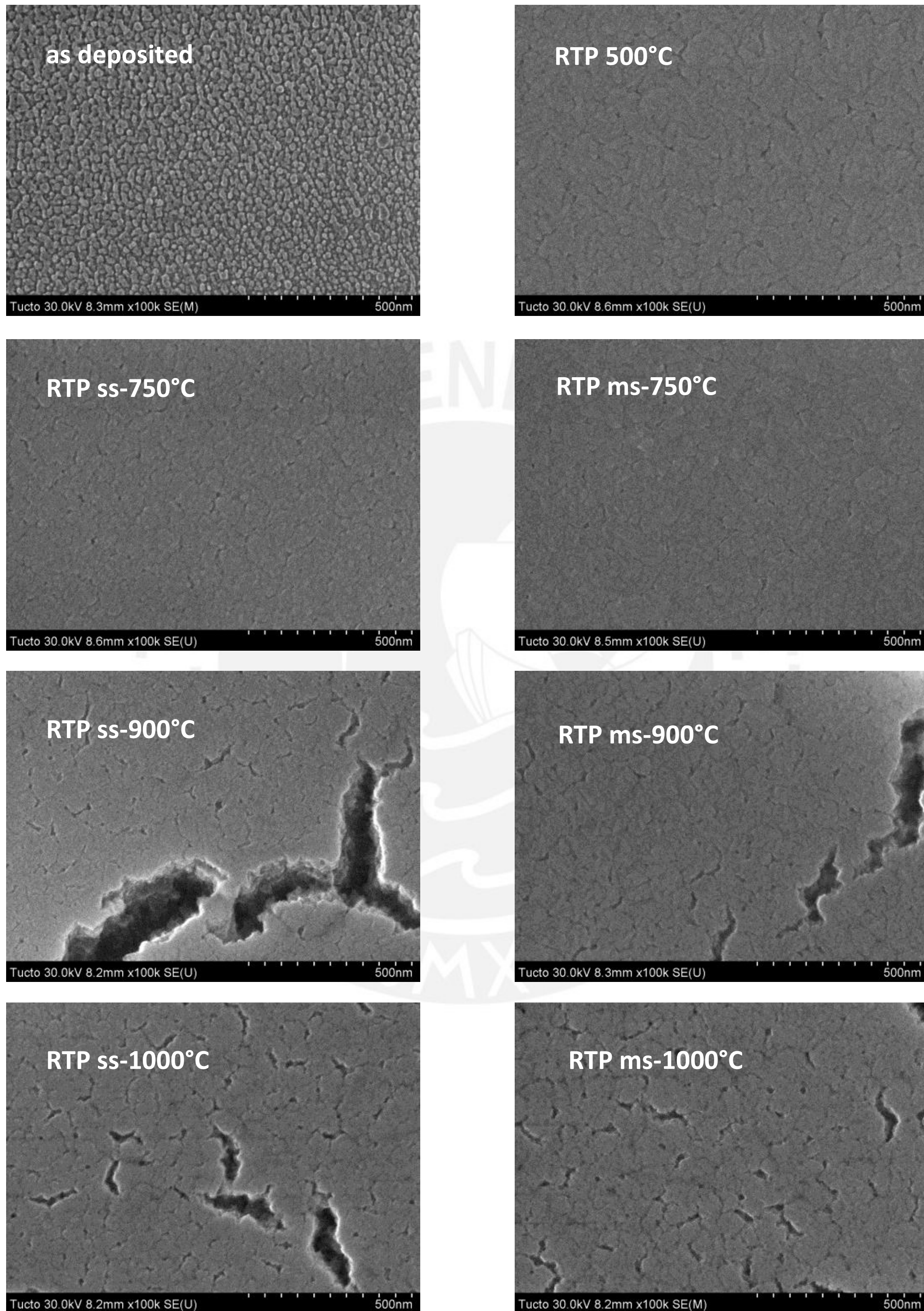


***Figure 4.17*** *SEM micrographs for samples RTP single-step (ss) and multi-step (ms) treated.*



Tesis publicada con autorización del autor
No olvide citar esta tesis

Scanning electron microscopy was applied to evaluate the surface morphology of the films. Figure 4.17 and Figure 4.18 show SEM images for the AlN:Tb films deposited by RF magnetron sputtering and annealed treated with RTP single-step, RTP multi-step and QTF single-step processes at different temperatures. The micrograph for the as deposited sample is shown in Figure 4.17 (a) and it reveals a grainy morphology at the surface. The average crystallite size from XRD was about 10 nm, while the as deposited SEM image reveals an overall grain size of about 100 nm. This reveals the grain size is bigger than the crystallite size as literature also suggests [105], [106]. The grain can be thought of an agglomerate of smaller crystallites. For an accurate estimation of the crystallite and grain size, TEM analysis is necessary.

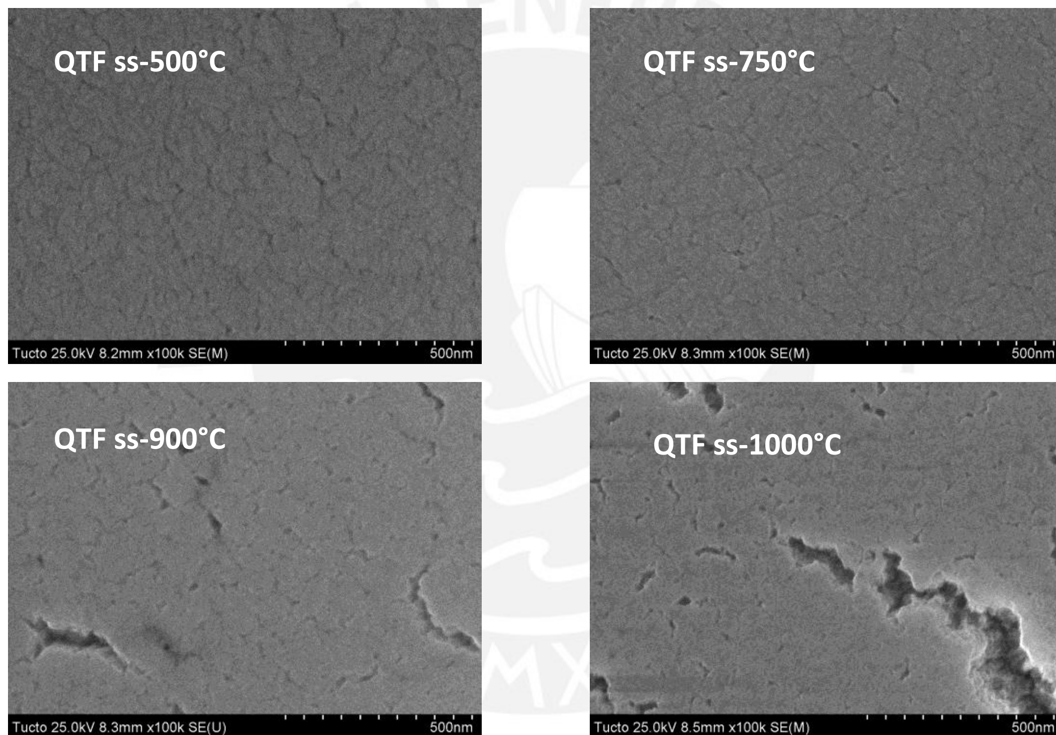


***Figure 4.18*** *SEM micrographs for samples annealed with QTF single-step process.*

After annealing treatment, the grainy surface morphology disappears and a dense surface morphology is observed. The SEM micrographs presents not much differences between the samples annealed using RTP or QTF process, since both annealing treatments shows a dense microstructure where the grain size looks incremented with annealing temperature (see Figure 4.17 and Figure 4.18). This apparent larger grains observed at the surface may be an agglomerate of small grains



Tesis publicada con autorización del autor
No olvide citar esta tesis

PONTIFICIA UNIVERSIDAD CATÓLICA DEL PERÚ

Also, with increasing annealing temperatures, the film microstructure show untied, thinner interfaces than in as deposited film. At 900°C and 1000°C cracking formation is observed, causing large spaces between grains and damaging the structure. Note the relation between the presence of cracking formation in SEM images and the tensile strain found by XRD analysis for samples annealed above 500°C. The release of the as deposited compressive stresses in thin films by post deposition annealing is convenient for the good optical and electrical properties of the films. However, the release of stress occurs at 500°C then at higher annealing temperatures tensile stress appears producing cracking formation in the films. Also loss of adhesion of the film to the substrate had been seen after annealing. In order to achieve AlN:Tb films of better quality, low deposition pressure and higher substrate temperature can enhance the adhesion of the growth structure on the substrate surface. On the other hand, if the substrate must be cooled to improve the growth of amorphous structure, it is necessary a previous investigation of suitable substrates with lattice spacing and thermal expansion coefficients that matches better with that of the sputtering species.

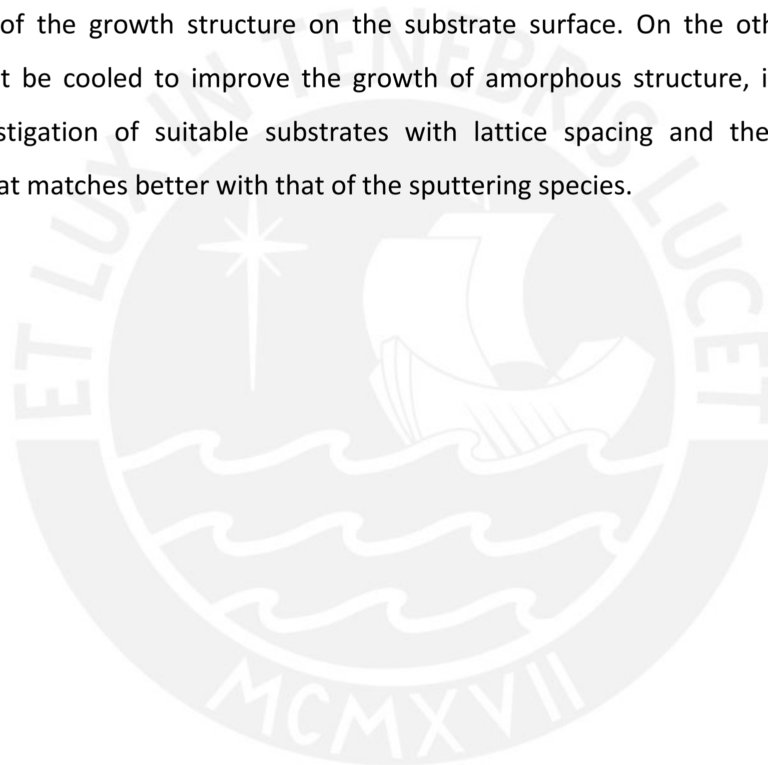



Tesis publicada con autorización del autor
No olvide citar esta tesis

PONTIFICIA UNIVERSIDAD CATÓLICA DEL PERÚ

# 5 Conclusion

AlN is a wide band gap semiconductor and when doped with Tb it can exhibit an intense green luminescence, corresponding to the $^5D_4$ de-excitation of the Tb ion. The luminescent and semiconductor characteristics of AlN:Tb make of it a promising material for optoelectronic applications. In the present thesis AlN:Tb thin films were deposited on silicon substrates by RF magnetron sputtering. A method has been developed to apply the JO analysis using the emission spectra of the produced films.

The proposed method had proven its ability to recover the branching ratios and the radiative lifetime values reported in literature with an error less than 2% for the radiative lifetime and an RMS deviation of 0.04 between the experimental and calculated branching ratios.

The films were annealed using RTP single-step, RTP multi-step and QTF single-step process. Since the annealing changes the host microstructure, it can modify the local structure around the Tb ion and influence the probability of interaction between the Tb ion and the external excitation. These changes do not perturb the electron transitions within the 4f shell and the emission color remains independent of the host.

Table 5.1 summarizes the results of the luminescence and structural analysis. The JO analysis was applied to the samples to estimate the radiative parameters. The spontaneous emission probability follows the increasing/decreasing tendency of the intensity. The branching ratio of the $^5D_4 \rightarrow {}^7F_5$ is $\geq 0.50$ which is reasonable high due to the efficient stimulate emission of the transition. The radiative life times calculated from the JO analysis are found to be 4.3 for the as deposited sample, and 3.3, 3.5 and 3.8 at the maximum intensity obtained with RTP single-step, RTP multi-step and QTF single-step annealed sample respectively.

The high spontaneous emission probability and the shorter radiative lifetime indicate optimal activation of the ions and fast decay of the electrons from the $^5D_4$ upper manifold after excitation. It can be attributed to the host-lattice interaction with the Tb ion.



Tesis publicada con autorización del autor
No olvide citar esta tesis

TESIS PUCP

PONTIFICIA UNIVERSIDAD CATÓLICA DEL PERÚ

**Table 5.1** *Summary of the luminescent properties obtained for the transition $^5D_4 \rightarrow {}^7F_5$ of Tb and the results of structural and composition analysis of the prepared samples with and without annealing treatment. The shaded row highlights the maximum intensity in each annealing treatment.*

| *Annealing* ($°C$) | $\bar{\lambda}$ *(nm)* | *Intensity Area* $\times 10^7$ $(cps \cdot nm)$ | $A_{4\rightarrow5}$ $(s^{-1})$ | $\beta_r^{cal}$ | $\tau_r$ *(ms)* | *Judd Ofelt parameters* $\times 10^{-20}\ cm^2$ | | | *XRD (crystalline phase)* | *Oxygen at.%* | *O:N ratio* | *Crystallite size (nm)* |
|---|---|---|---|---|---|---|---|---|---|---|---|---|
| | | | | | | $\Omega_2$ | $\Omega_4$ | $\Omega_6$ | | | | |
| *As deposited* | 546 | 5.27 | 117.80 | 0.50 | 4.3 | 0.11 | 0.12 | 2.81 | AlN wurtzite hexagonal | 30 | 1.1 | 11.0 |
| *RTP ss 500* | 546 | 49.47 | 145.67 | 0.55 | 3.8 | 0.06 | 0.12 | 0.01 | AlN wurtzite hexagonal | 34 | 1.7 | 9.8 |
| *RTP ss 750* | 547 | 160.92 | 164.32 | 0.56 | 3.3 | 0.09 | 0.08 | 0.01 | AlN wurtzite hexagonal | 34 | 1.9 | 10.0 |
| *RTP ss 900* | 546 | 80.64 | 145.10 | 0.58 | 4.0 | 0.09 | 0.04 | 0.01 | AlN (hex) + $Al_5O_6N$ (cub) + $Al_2O_3$ (cub) | 35 | 2.2 | 8.7 |
| *RTP ss 1000* | 545 | 40.92 | 159.41 | 0.56 | 3.5 | 0.01 | 0.04 | 0.01 | AlN (hex) + $Al_5O_6N$ (cub) + $Al_2O_3$ (cub) | 38 | 2.9 | 9.4 |
| *RTP ms 750* | 547 | 55.40 | 133.78 | 0.57 | 4.2 | 0.08 | 0.05 | 0.01 | AlN wurtzite hexagonal | 38 | 2.6 | 7.6 |
| *RTP ms 900* | 546 | 95.64 | 163.5 | 0.58 | 3.5 | 0.09 | 0.03 | 0.21 | AlN (hex) + $Al_5O_6N$ (cub) + $Al_2O_3$ (cub) | 34 | 2.2 | 8.0 |
| *RTP ms 1000* | 547 | 37.72 | 152.8 | 0.55 | 3.6 | 0.10 | 0.05 | 0.01 | AlN (hex) + $Al_5O_6N$ (cub) + $Al_2O_3$ (cub) | 41 | 3.7 | 9.5 |
| *QTF ss 500* | 547 | 8.26 | 146.48 | 0.54 | 3.6 | 0.12 | 0.05 | 0.20 | AlN wurtzite hexagonal | 33 | 1.7 | 9.9 |
| *QTF ss 750* | 546 | 10.45 | 143.33 | 0.53 | 3.7 | 0.15 | 0.05 | 0.01 | AlN wurtzite hexagonal | 38 | 2.6 | 8.7 |
| *QTF ss 900* | 547 | 20.82 | 148.99 | 0.57 | 3.8 | 0.14 | 0.08 | 0.01 | $Al_2O_3$ (hex) | 45 | 5.7 | 7.7 |
| *QTF ss 1000* | 545 | 13.50 | 147.7 | 0.57 | 3.8 | 0.13 | 0.06 | 0.01 | $Al_2O_3$ (hex) | 50 | 12.2 | 8.3 |



Tesis publicada con autorización del autor
No olvide citar esta tesis

The annealing treatments introduced more oxygen concentration in the films and possible desorption of the nitrogen. As the annealing temperature increases, the O:N ratio also increases, and the crystalline phases present transformations. The AlN hexagonal wurtzite structure presented second phase formation of $Al_2O_3$ and $Al_5O_6N$ cubic structure at higher annealing temperatures using RTP. Besides, the as deposited film presents 30 at.% of oxygen content not seen in the XRD analysis. This suggests the produced films consist also of amorphous phases rich in oxygen content.

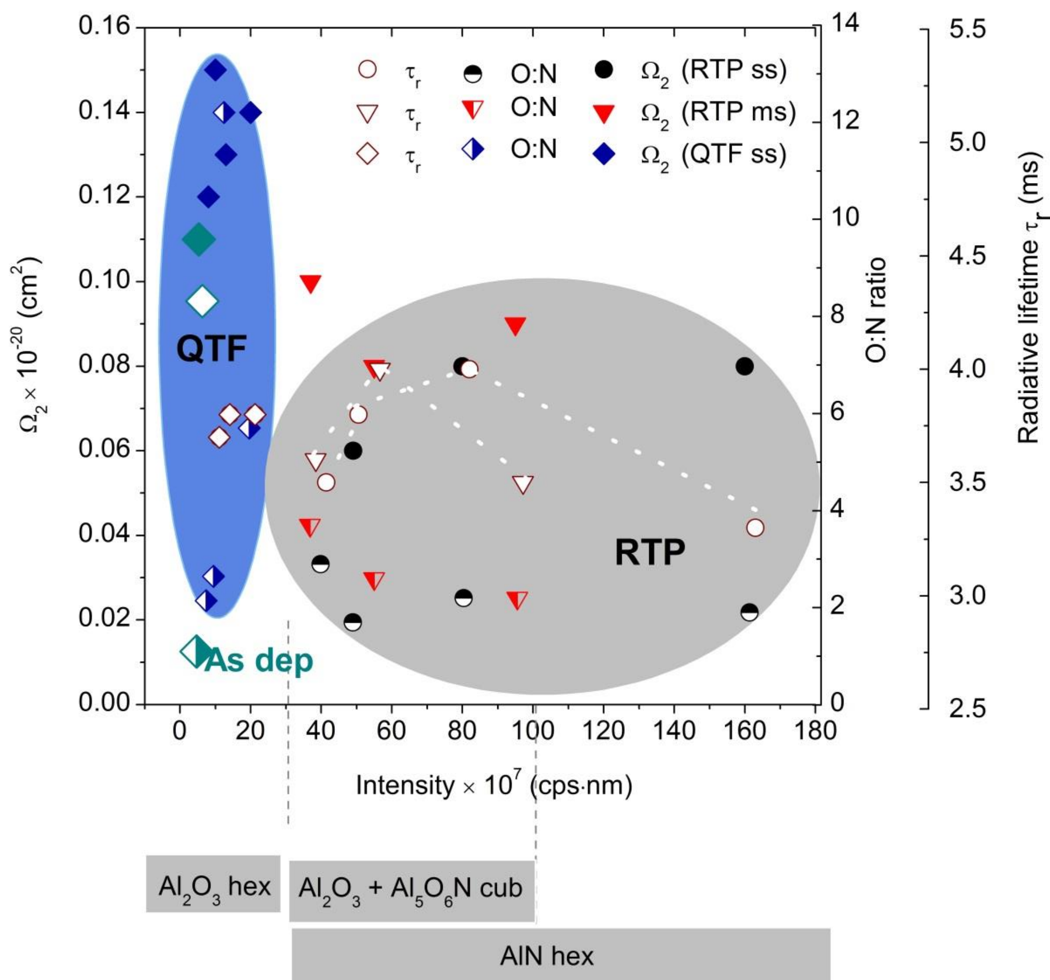


***Figure 5.1*** *The* $\mathbf{\Omega_2}$ *parameter, O:N ratio and calculated radiative lifetime versus the intensity area of the transition* $^5\boldsymbol{D_4} \rightarrow {}^7\boldsymbol{F_5}$ *.*

In the present work the thermal activation effect on the luminescence intensity of AlN:Tb thin films were studied. The results show that the intensity increments with low O:N ratio and less crystalline phases containing oxygen (see Figure 5.1). The relation of $\Omega_2$ with the local



Tesis publicada con autorización del autor
No olvide citar esta tesis

symmetry and bonding in the vicinity of the RE ion is reflected in the results. The increment in the values of $\Omega_2$ is related to higher O:N ratios and to the change of the crystalline phase into hexagonal $Al_2O_3$, which results in a decrease of the intensity and longer radiative lifetime values.

Compared with the RTP annealing, the QTF process is detrimental for the emission intensity. The best annealing treatment in this investigation was the RTP single-step process. The samples annealed with RTP single-step process showed lower O:N ratios and maintained the hexagonal AlN phase during the formation of second phases of cubic $Al_2O_3$ and $Al_5O_6N$. It is possible that the oxygen content was present in amorphous phase. The shortest radiative lifetime of 3.3 ms and the highest emission intensity was obtained at 750°C using RTP single-step annealing.

Future work should focus on TEM to strength the structural analysis. With TEM it would be possible to estimate accurately the amorphous and crystalline phases, the crystallite and the grain size, and more important to characterize the local structure around the RE ion. In addition, the determination of the optical band gap of the host matrix and the mechanism behind the thermal activation of the Tb ion can fulfill the scientific picture of the correlation between the obtained properties.



Tesis publicada con autorización del autor
No olvide citar esta tesis

TESIS PUCP

PONTIFICIA UNIVERSIDAD CATÓLICA DEL PERÚ

# References

[1] B. M. Walsh, “Judd-Ofelt theory: principles and practices,” *Adv. Spectrocopy Lasers Sens.*, pp. 403–433, 2006.

[2] M. Maqbool and T. Ali, “Intense Red Catho- and Photoluminescence from 200 nm Thick Samarium Doped Amorphous AlN Thin Films.,” *Nanoscale Res. Lett.*, vol. 4, no. 7, pp. 748–752, 2009.

[3] J. Lucas, P. Lucas, T. Le Mercier, A. Rollat, and W. Davenport, *Rare Earths*. Elsevier, 2015.

[4] A. J. Kenyon, “Quantum confinement in rare-earth doped semiconductor systems,” *Curr. Opin. Solid State Mater. Sci.*, vol. 7, no. 2, pp. 143–149, Apr. 2003.

[5] M. Beeler, E. Trichas, and E. Monroy, “III-nitride semiconductors for intersubband optoelectronics: a review,” *Semicond. Sci. Technol.*, vol. 28, no. 7, p. 074022, 2013.

[6] F. Group, “Chapter 1,” pp. 1–4, 2009.

[7] P. Ruterana, M. Albrecht, and J. Neugebauer, *Nitride Semiconductors: Handbook of Materials and Devices*. Germany: Wiley-VCH, 2003.

[8] H. Jin, J. Zhou, S. R. Dong, B. Feng, J. K. Luo, D. M. Wang, W. I. Milne, and C. Y. Yang, “Deposition of c-axis orientation aluminum nitride films on flexible polymer substrates by reactive direct-current magnetron sputtering,” *Thin Solid Films*, vol. 520, no. 15, pp. 4863–4870, 2012.

[9] D. Maurya, A. Sardarinejad, and K. Alameh, “Recent Developments in R.F. Magnetron Sputtered Thin Films for pH Sensing Applications—An Overview,” *Coatings*, vol. 4, no. 4, pp. 756–771, 2014.

[10] a. Stolz, a. Soltani, B. Abdallah, J. Charrier, D. Deresmes, P. Y. Jouan, M. a. Djouadi, E. Dogheche, and J. C. De Jaeger, “Optical properties of aluminum nitride thin films grown by direct-current magnetron sputtering close to epitaxy,” *Thin Solid Films*, vol. 534, pp. 442–445, 2013.

[11] M. Maqbool, W. M. Jadwisienczak, and M. E. Kordesch, “Cathodoluminescence from Amorphous and Nanocrystalline Nitride Thin Films Doped with Rare Earth and Transition Metals,” 1999.



Tesis publicada con autorización del autor
No olvide citar esta tesis

[12] D. Y. Kim, H. S. Cho, K. B. Park, J. Y. Kwon, and J. S. Jung, "Effect of thermal annealing on sputtered a-Si film," *J.Korean Phys.Soc.*, vol. 45, no. December, pp. S847–S850, 2004.

[13] A. G. Ramirez, H. Ni, and H. J. Lee, "Crystallization of amorphous sputtered NiTi thin films," *Mater. Sci. Eng. A*, vol. 438–440, no. SPEC. ISS., pp. 703–709, 2006.

[14] O. Erlenbach, G. Gálvez, J. A. Guerra, F. De Zela, R. Weingärtner, and A. Winnacker, "Thermal Activation and Cathodoluminescence Measurements of Tb3+-Doped a-(SiC)1-x(AlN)x Thin Films," *Mater. Sci. Forum*, vol. 645–648, pp. 459–462, 2010.

[15] F. Huang, X. Liu, L. Hu, and D. Chen, "Spectroscopic properties and energy transfer parameters of Er(3+)- doped fluorozirconate and oxyfluoroaluminate glasses.," *Sci. Rep.*, vol. 4, p. 5053, 2014.

[16] P. Chimalawong, J. Kaewkhao, and P. Limsuwan, "Effect of $Nd^{3+}$ Concentration on the Physical and Absorption Properties of Soda-Lime-Silicate Glasses," *Adv. Mater. Res.*, vol. 93–94, no. 4, pp. 455–458, 2010.

[17] P. Van Do, V. P. Tuyen, N. M. Khaidukov, and N. T. Thanh, "Predict optical properties of Dy 3 + ions doped double potassium gadolinium fluoride crystal from absorption spectra," vol. 28, pp. 61–67, 2012.

[18] I. Pal, a Agarwal, S. Sanghi, and M. P. Aggarwal, "Spectroscopic and radiative properties of Nd 3 + ions doped zinc bismuth borate glasses," vol. 51, no. January, pp. 18–25, 2013.

[19] S. Dutta, S. Som, and S. K. Sharma, "Excitation spectra and luminescence decay analysis of $K^{+}$ compensated $Dy^{3+}$ doped $CaMoO_{4}$ phosphors," *RSC Adv.*, vol. 5, no. 10, pp. 7380–7387, 2015.

[20] B. R. Judd, "Optical Absorption Intensities of Rare-Earth Ions," *Phys Rev*, vol. 127, pp. 750–761, 1962.

[21] B. R. Judd, "The Matrix Elements of Tensor Operators for the Electronic Configurations fn," *Proc. Phys. Soc.*, vol. 74, no. 3, pp. 330–339, 1959.

[22] J. Ofelt, "Intensities of crystal spectra of rare-earth ions," *Chem Phys*, vol. 37, pp. 511–520, 1962.

[23] A. . Belyanin, L. . Bouilov, V. . Zhirnov, A. . Kamenev, K. . Kovalskij, and B. . Spitsyn, "Application of aluminum nitride films for electronic devices," *Diam. Relat. Mater.*, vol. 8, no. 2–5, pp. 369–372, Mar. 1999.



Tesis publicada con autorización del autor
No olvide citar esta tesis

PONTIFICIA UNIVERSIDAD CATÓLICA DEL PERÚ

[24] N. Kumari, A. K. Singh, and P. K. Barhai, "Study of Properties of AlN Thin Films Deposited by Reactive Magnetron Sputtering," *Int. J. Thin Film. Sci. Technol.*, vol. 3, no. 2, pp. 43–49, 2014.

[25] W. Wang, P. Zhang, X. Wang, X. Lei, H. Ding, and H. Yang, "Bifunctional AlN:Tb semiconductor with luminescence and photocatalytic properties," *RSC Adv.*, vol. 5, no. 110, pp. 90698–90704, 2015.

[26] F. Benz, J. A. Guerra, Y. Weng, A. R. Zanatta, R. Weingärtner, and H. P. Strunk, "Concentration quenching of the green photoluminescence from terbium ions embedded in AlN and SiC matrices," *J. Lumin.*, vol. 137, pp. 73–76, May 2013.

[27] F. Benz, H. P. Strunk, J. Schaab, U. Künecke, and P. Wellmann, "Tuning the emission colour by manipulating terbium-terbium interactions: Terbium doped aluminum nitride as an example system," *J. Appl. Phys.*, vol. 114, no. 7, 2013.

[28] F. Benz, T. Walther, and H. P. Strunk, "Towards the structure of rare earth luminescence centres – terbium doped aluminium nitride as an example system," *J. Phys. Conf. Ser.*, vol. 471, p. 012032, 2013.

[29] F. Benz, M. Yang, Y. Weng, and H. P. Strunk, "Luminescence intensity and dopant concentration in AlN:Tb," *J. Lumin.*, vol. 132, no. 6, pp. 1493–1496, Jun. 2012.

[30] I. Pelant and J. Valenta, "Kinetic description of luminescence properties," in *Luminescence Spectroscopy of Semiconductors*, New York: Oxford University Press Inc., 2012.

[31] A. Sennaroglu, *Solid-State Lasers and Applications*. USA: CRC Press, 2007.

[32] A. R. Z. R. Weingärtner, O. Erlenbach, A. Winnacker, A. Welte, I. Brauer, H. Mendel, H.P. Strunk, C.T.M. Ribeiro, "Thermal activation, cathodo- and photoluminescence measurements of rare earth doped (Tm, Tb, Dy, Eu, Sm, Yb) amorphous/nanocrystalline AlN thin films prepared by reactive rf-sputtering," *Opt. Mater. (Amst).*, vol. 28, p. 790, 2006.

[33] C. Delsart and N. Pelletier-Allard, "Probabilities for radiative and nonradiative decay of Pr3+ ion in LaAl03," *J. Phys. C Solid State Phys*, vol. 6, p. 1277, 1973.

[34] H. Shalibeik, "Rare-Earth-Doped Fiber Lasers and Amplifiers," Technischen Universität Carolo-Wilhelmina zu Braunschweig, 2007.

[35] G. Liu and B. Jacquier, "Rare Earth Doped Confined Structures for Lasers and



Tesis publicada con autorización del autor
No olvide citar esta tesis

TESIS PUCP

Amplifiers," in *Spectroscopic Properties of Rare Earths in Optical Materials*, China: Springer-Verlag Berling Heidelberg, 2005.

[36] M. H. V. Werts, "Luminescent Lanthanide Complexes: Visible Light Sensitised Red and Near-infrared Luminescence.," University of Amsterdam, 2000.

[37] J. G. Bunzli and S. V Eliseeva, "Basics of Lanthanide Photophysics," *Springer Ser. Fluoresc.*, pp. 1–45, 2011.

[38] R. C. Powell, "Electronic energy levels," in *Physics of Solid-State Laser Materials*, New York: Springer-Verlag, 1998.

[39] D. J. Newman, *The Theory of Lanthanide Crystal Fields*, vol. 20, no. 84. 1971.

[40] M. Gerloch and R. . Slade, *Ligand Field Parameters*. Great Britain: Cambridge University Press, 1973.

[41] M. P. Hehlen, M. G. Brik, and K. W. Krämer, "50th anniversary of the Judd-Ofelt theory: An experimentalist's view of the formalism and its application," *J. Lumin.*, vol. 136, pp. 221–239, 2013.

[42] C. Görller-Walrand and K. Binnemans, "Spectral Intensities of f-f Transitions," in *Handbook on the Physics and Chemistry of Rare Earths, Volumen 325*, USA: Elsevier Science B.V, 1998.

[43] S. Tanabe, "Optical transitions of rare earth ions for ampli ® ers : how the local structure works in glass," vol. 259, pp. 1–9, 1999.

[44] P. Nachimuthu and R. Jagannathan, "Judd–Ofelt Parameters, Hypersensitivity, and Emission Characteristics of Ln3+ (Nd3+, Ho3+, and Er3+) Ions Doped in PbO–PbF2 Glasses," *J. Am. Ceram. Soc*, vol. 82, pp. 387–92, 1999.

[45] A. A. Kaminskii, "Intensity of Radiative Transitions of Ln3+ Activators in Insulating Laser Crystals," in *Crystalline Lasers: Physical Processes and Operating Schemes*, USA: CRC Press, 1996, pp. 227–302.

[46] B. C. Jamalaiah, M. V. Vijaya Kumar, and K. Rama Gopal, "Investigation on luminescence and energy transfer in Tb3-doped lead telluroborate glasses," *Phys. B Condens. Matter*, vol. 406, no. 14, pp. 2871–2875, 2011.

[47] R. Reisfeld and C. K. Jorgensen, "Rare-Earth Lasers," in *Lasers and Excited States of Rare Earths*, Berlin Heildelberg: Springer-Verlag, 1977.



Tesis publicada con autorización del autor
No olvide citar esta tesis

[48] D. K. Sardar, K. L. Nash, R. M. Yow, J. B. Gruber, U. V. Valiev, and E. P. Kokanyan, "Absorption intensities and emission cross sections of Tb3+ (4f8) in TbAlO3," *J. Appl. Phys.*, vol. 100, no. 8, p. 083108, 2006.

[49] V. Vasyliev, E. G. Víllora, Y. Sugahara, and K. Shimamura, "Judd-Ofelt analysis and emission quantum efficiency of Tb-fluoride single crystals: LiTbF4 and Tb0.81Ca0.19F2.81," *J. Appl. Phys.*, vol. 113, no. 20, p. 203508, 2013.

[50] J. A. Guerra, "Determination of the optical bandgap of thin amorphous (SiC)1-x(AlN)x films produced by radio frequency dual magnetron sputtering," Pontificia Universidad Católica del Perú. Master Thesis, 2010.

[51] A. Barybin and V. Shapovalov, "Substrate Effect on the Optical Reflectance and Transmittance of Thin-Film Structures," *Int. J. Opt.*, vol. 2010, pp. 1–18, 2010.

[52] E. Marquez, J. Ramirez-Malo, P. Villares, R. Jimenez-Garay, P. J. S. Ewen, and a E. Owen, "Calculation of the thickness and optical constants of amorphous arsenic sulphide films from their transmission spectra," *J. Phys. D. Appl. Phys.*, vol. 25, no. 3, pp. 535–541, 2000.

[53] R. Swanepoel, "Determination of surface roughness and optical constants of inhomogeneous amorphous silicon films Determination of surface roughness and optical constants of inhomogeneous amorphous silicon films," *J. Phys. E.*, vol. 17, 1984.

[54] W. Yen, S. Shionoya, and H. Yamamoto, "Principal phosphor materials and their optical properties," in *Phosphor Handbook*, 2nd Ed., CRC Press, 2007.

[55] J. A. Guerra, L. Montañez, A. Winnacker, F. De Zela, and R. Weingärtner, "Thermal activation and temperature dependent PL and CL of Tb doped amorphous AlN and SiN thin films," *Phys.Status Solidi C*, vol. 12, no. No. 8, pp. 1183–1186, 2015.

[56] B. G. Yacobi and D. B. Holt, "Cathodoluminescence scanning electron microscopy of semiconductors," *J. Appl. Phys.*, vol. 59, no. 4, p. R1, 1986.

[57] O. Sjölund, H. T. Lin, D. H. Rich, M. Ghisoni, a. Larsson, S. Wang, J. Thordsson, and T. G. Andersson, "Cathodoluminescence and electron beam induced current study of partially relaxed AlGaAs/GaAs/InGaAs heterojunction phototransistors under operating conditions," *J. Appl. Phys.*, vol. 82, no. 3, p. 1438, 1997.

[58] J. Sam Boggs and D. Krinsley, *Application of Cathodoluminescence Imaging to the Study of Sedimentary Rocks*, vol. XXXIII. New York: Cambridge University Press, 2006.



Tesis publicada con autorización del autor
No olvide citar esta tesis

[59] L. Ozawa, *Cathodoluminescence: Theory and Applications*. Tokyo (Japan): Kodansha Ltd., 1990.

[60] C. O. Mosiori, “Energy Band Theory,” in *High Speed Semiconductor Physics: Principles, Theory and Devices*, Hamburg: Anchor Academic Publishing, 2015, pp. 100–114.

[61] Roushdey Salh, “Silicon Nanocluster in Silicon Dioxide: Cathodoluminescence, Energy Dispersive X-ray Analysis, Infrared Spectroscopy Studies, Crystalline Silicon - Properties and Uses,” *In Tech*, 2011. [Online]. Available: http://www.intechopen.com/books/crystalline-siliconproperties-and-uses/silicon-nanocluster-in-silicon-dioxide-cathodoluminescence-energy-dispersive-x-rayanalysis-infrared. [Accessed: 11-Dec-2015].

[62] T. H. Myers, *GaN and Related Alloys-1999:Volume 595*. United States: Materials Research Society, 2000.

[63] A. L. D. Max Wallace, *Characterization of Electron-Hole Pair Migration and Trapping in Rare Earth Doped YBO3 under Vacuum Ultraviolet Excitation*, vol. 44. 2013, pp. 210–213.

[64] R. C. A. and S. Bloom, “Cathodoluminescent efficiency,” *J. Electrochem. Soc.*, vol. 124, p. 1136, 1977.

[65] G. F. J. Garlick, *Luminescence of Inorganic Solids*. New York, 1966.

[66] A. Rothwarf, “Plasmon theory of electron-hole pair production: efficiency of cathode ray phosphors,” *J. Appl. Phys.*, vol. 44, p. 752, 1973.

[67] M. Maqbool, “Growth, Characterization and Luminescence and Optical properties of Rare Earth elements and Transition Metals doped in Wide Bandgap Nitride Semiconductors,” Ohio University.

[68] E. Ruiz and S. Alvarez, “Electronic structure and properties of AlN,” *Phys. Rev. B*, vol. 49, no. 11, 1994.

[69] L. Shen, R. K. Y. Fu, and P. K. Chu, “Synthesis of aluminum nitride films by plasma immersion ion implantation-deposition using hybrid gas-metal cathodic arc gun,” *Rev. Sci. Instrum.*, vol. 75, no. 3, pp. 719–724, 2004.

[70] H. Morkoç, *Handbook of Nitride Semiconductors and Devices. Volume 1: Material Properties, Physics and Growth*. Germany: Wiley-VCH, 2008.



Tesis publicada con autorización del autor
No olvide citar esta tesis

[71] M. . Mendez, S. . Rodriguez, R. Machorro, and W. D. Cruz, “Characteriztion of AlN thin films deposited by DC reactive magnetron sputtering,” *Rev. Mex. Fis.*, vol. 54, no. 4, pp. 271–278, 2008.

[72] L. Berger, “Binary IV-VI and III-V Semiconductors,” in *Semiconductor Materials*, USA: CRC Press, 1997.

[73] D. Chung, *Composite Materials: Science and Applications. Functional Materials for Modern Technologies*. Berlin Heildelberg: Springer-Verlag London, 2004.

[74] C. Madhukar Reddy, B. Sudhakar Reddy, G. R. Dillip, K. Mallikarjuna, and B. Deva Prasad Raju, “FT-IR, FT-Raman and fluorescence studies of Tb3+ ions activated lead containing sodium fluoroborate glasses,” *J. Mol. Struct.*, vol. 1019, pp. 166–173, 2012.

[75] J. Vuojola and T. Soukka, “Luminescent lanthanide reporters: new concepts for use in bioanalytical applications,” *Methods Appl. Fluoresc.*, vol. 2, no. 1, p. 012001, 2014.

[76] P. C. Ricci, C. M. Carbonaro, R. Corpino, C. Cannas, and M. Salis, “Optical and structural characterization of terbium-doped Y \n 2SiO\n 5 phosphor particles,” *J. Phys. Chem. C*, vol. 115, pp. 16630–16636, 2011.

[77] C. C. Chiang, M. S. Tsai, and M. H. Hon, “Synthesis and photoluminescent properties of Ce3+ doped terbium aluminum garnet phosphors,” *J. Alloys Compd.*, vol. 431, no. 1–2, pp. 298–302, Apr. 2007.

[78] C. L. Hardin, Y. Kodera, S. a Basun, D. R. Evans, and J. E. Garay, “Transparent, luminescent terbium doped zirconia: development of optical-structural ceramics with integrated temperature measurement functionalities,” *Opt. Mater. Express*, vol. 3, no. 6, p. 893, 2013.

[79] J. E. Penilla, E. H., Kodera, Y. and Garay, “Blue–Green Emission in Terbium-Doped Alumina (Tb:Al2O3) Transparent Ceramics,” *Adv. Funct. Mater.*, vol. 23, pp. 6036–6043, 2013.

[80] J. A. Guerra, F. Benz, A. R. Zanatta, H. P. Strunk, A. Winnacker, and R. Weingärtner, “Concentration quenching and thermal activation of the luminescence from terbium-doped a -SiC:H and c -AlN thin films,” *Phys. Status Solidi*, vol. 10, no. 1, pp. 68–71, 2013.

[81] P. Gehring, Y. Weng, Z. Wu, and H. P. Strunk, “Photoluminescence from Al x In 1−x N layers doped with Tb 3+ ions,” *J. Phys. Conf. Ser.*, vol. 281, p. 012014, 2011.

[82] F. Lu, R. Carius, A. A. Alam, and M. Heuken, “Terbium implanted AlN and



Tesis publicada con autorización del autor
No olvide citar esta tesis

photoluminescence properties," *J. Korean Phys. Soc.*, vol. 46, no. May, pp. S48–S51, 2005.

[83] A. Guerra, "Determination of the Optical Bandgap of thin amorphous (SiC)1-x(AlN)x films," Pontificia Universidad Católica del Perú, 2010.

[84] P. Abdul Azeem and M. Kalidasan, "Luminescence Properties on Tb 3 + Doped Lead Fluoroborate Glasses," in *International Conference on Management, Applied and Social Sciences*, 2012, pp. 394–396.

[85] P. Abdul Azeem, M. Kalidasan, R. R. Reddy, and K. Ramagopal, "Spectroscopic investigations on Tb 3 doped lead fluoroborate glasses," *Opt. Commun.*, vol. 285, no. 18, pp. 3787–3791, 2012.

[86] J. L. Pascual, Z. Barandiarán, and L. Seijo, "Ab initio theoretical study of the 4f8 and 4f7 5d manifolds of Tb3+ doped BaF2 cubic sites," *J. Lumin.*, vol. 145, pp. 808–817, 2014.

[87] R. Reisfeld, "Optical Properties of Lanthanides in Condensed Phase, Theory and Applications," *AIMS Mater. Sci.*, vol. 2, no. 2, pp. 37–60, 2015.

[88] J. G. Kang and T. J. Kim, "Luminescence and crystal-field analysis of europium and terbium complexes with oxydiacetate and 1,10-phenanthroline," *Bull. Korean Chem. Soc.*, vol. 26, no. 7, pp. 1057–1064, 2005.

[89] N. Duhamel-Henry, J. L. Adam, B. Jacquier, and C. Linarès, "Photoluminescence of new fluorophosphate glasses containing a high concentration of terbium (III) ions," *Opt. Mater. (Amst).*, vol. 5, no. 3, pp. 197–207, 1996.

[90] A. Podhorodecki, M. Banski, J. Misiewicz, J. Serafińczuk, and N. V. Gaponenko, "Influence of Annealing on Excitation of Terbium Luminescence in YAlO[sub 3] Films Deposited onto Porous Anodic Alumina," *J. Electrochem. Soc.*, vol. 157, no. 6, p. H628, 2010.

[91] U. V. Valiev, J. B. Gruber, I. A. Ivanov, G. W. Burdick, H. Liang, L. Zhou, D. Fu, O. V. Pelenovich, V. O. Pelenovich, and Z. Lin, "Magnetooptics of the luminescent transitions in Tb3+:Gd3Ga5O12," *Opt. Mater. (Amst).*, vol. 46, no. MAY, pp. 282–291, 2015.

[92] Y. Li, Y. Chang, Y. Lin, Y. Chang, and Y. Lin, "Synthesis and luminescent properties of Ln3+ (Eu3+, Sm3+, Dy3+)-doped lanthanum aluminum germanate LaAlGe2O7 phosphors," *J. Alloys Compd.*, vol. 439, pp. 367–375, 2007.

[93] T. Jiang, X. Xu, and Å. Ê, "A strong green-emitting phosphor : : K3Gd(PO4)2:Tb3+ for UV-



Tesis publicada con autorización del autor
No olvide citar esta tesis

excited white light-emitting-diodes.," *Chinese Opt. Lett.*, vol. 12, no. 1, pp. 11–13, 2014.

[94] S. Xia and P. A. Tanner, "Theory of one-phonon-assisted energy transfer between rare-earth ions in crystals," pp. 1–17, 2002.

[95] A. R. Zanatta, "Effect of thermal annealing treatments on the optical properties of rare-earth-doped AlN films," *J.Phys.D: Appl. Phys.*, vol. 42, no. 025109, p. 7 pp, 2009.

[96] A. Janotta, M. Schmidt, R. Janssen, and M. Stutzmann, "Photoluminescence of Er 3+ implanted amorphous hydrogenated silicon suboxides," pp. 1–17, 2003.

[97] M. J. Weber, "Nonradiative decay from 5d states of rare earths in crystals," *Solid State Commun.*, vol. 12, no. 7, pp. 741–744, 1973.

[98] J. Ueda, P. Dorenbos, A. J. J. Bos, A. Meijerink, and S. Tanabe, "Insight into the Thermal Quenching Mechanism for $Y_3Al_5O_{12}$:$Ce^{3+}$ through Thermoluminescence Excitation Spectroscopy," *J. Phys. Chem. C*, vol. 119, no. 44, pp. 25003–25008, 2015.

[99] N. J. C. Ingle, A. Yuskauskas, R. Wicks, M. Paul, and S. Leung, "The structural analysis possibilities of reflection high energy electron diffraction," *J. Phys. D. Appl. Phys.*, vol. 43, no. 13, p. 133001, 2010.

[100] C. Cnr, "Rietveld Quantitative Phase Analysis ( RQPA )," 2004. [Online]. Available: http://www.xrd.us/services/quantificatin.htm. [Accessed: 08-Jul-2015].

[101] T. H. Taminiau, S. Karaveli, N. F. Van Hulst, and R. Zia, "Quantifying the magnetic nature of light emission," *Nat. Commun.*, vol. 3, pp. 976–979, 2012.

[102] R. Rolli, M. Montagna, S. Chaussedent, A. Monteil, V. K. Tikhomirov, and M. Ferrari, "Erbium-doped tellurite glasses with high quantum efficiency and broadband stimulated emission cross section at 1.5 um," *Opt. Mater. (Amst).*, vol. 21, pp. 743–748, 2003.

[103] H. Van Cong, "Quantum efficiency and radiative lifetime in degenerate n-type GaAs," *J.Phys.Chem. Solids*, vol. 42, pp. 95–99, 1981.

[104] G. C. Righini and M. Ferrari, "Photoluminescence of rare-earth-doped glasses," *Riv. del Nuovo Cim.*, vol. 28, no. 12, 2005.

[105] J. R. Ares, A. Pascual, I. J. Ferrer, and C. Sánchez, "Grain and crystallite size in polycrystalline pyrite thin films," *Thin Solid Films*, vol. 480–481, pp. 477–481, Jun. 2005.

[106] W. Wang, W. Widiyastuti, T. Ogi, and I. W. Lenggoro, "Correlations between Crystallite /



Tesis publicada con autorización del autor
No olvide citar esta tesis

Particle Size and Photoluminescence Properties of Submicrometer Phosphors," *Chem. Mater.*, vol. 19, pp. 1723–1730, 2007.

[107] L. Rosenberger, "Modification and characterization of aluminum nitride surfaces for an acoustic wave biosensor," Wayne State University, 2007.

[108] S. K. Kazuaki Kobayashi, "First-Principles Study of BN, SiC, and AlN Polytypes," *J. Phys. Soc. Japan*, vol. 77, no. 084703, 2008.

[109] Y.-W. Chung, *Introduction to Materials Science and Engineering*. United States of America: CRC Press, 2007.

[110] T. Campbell, R. K. Kalia, A. Nakano, P. Vashishta, and S. Rodgers, "Dynamics of Oxidation of Aluminum Nanoclusters using Variable Charge Molecular-Dynamics Simulations on Parallel Computers," *Phys Rev Lett.*, pp. 1–4, 1999.

[111] C. A. Ventrice and J. and H. Geisler, "The Growth and Structure of Epitaxial Metal-Oxide/Metal Interfaces," in *Thin Films: Heteroepitaxial Systems*, M. B. S. W. K. Liu, Ed. Singapore: World Scientific Publishing Company, 1999.

[112] T. K. Hatwar and T. R. Pian, "Surface Studies of Aluminum Nitride Thin Films," *MRS Proc.*, vol. 121, no. 557, 1988.



Tesis publicada con autorización del autor
No olvide citar esta tesis